Algorithm Development for Electrochemical Impedance Spectroscopy Diagnostics in PEM Fuel Cells

By

Ruth Anne Latham
BSME, Lake Superior State University, 2001

A Thesis Submitted in Partial Fulfillment of the
Requirements for the Degree of

MASTER OF APPLIED SCIENCE

in the department of Mechanical Engineering

We accept this thesis as conforming
to the required standards

Abstract

The purpose of this work is to develop algorithms to identify fuel cell faults using electrochemical impedance spectroscopy. This has been done to assist with the development of both onboard and off-board fuel cell diagnostic hardware.

Impedance can identify faults that cannot be identified solely by a drop in cell voltage[1]. Furthermore, it is able to conclusively identify electrode/flow channel flooding, membrane drying, and CO poisoning of the catalyst faults.

In an off-board device an equivalent circuit model fit to impedance data can provide information about materials in an operating fuel cell. It can indicate if the membrane is dry or hydrated, and whether or not the catalyst is poisoned. In an onboard device, following the impedance at three frequencies can differentiate between drying, flooding, and CO poisoning behaviour.

An equivalent circuit model, developed through a process of iterative design and statistical testing, is able to model fuel cell impedance in the 50 Hz to 50 kHz frequency range. The model, consisting of a resistor in series with a resistor and capacitor in parallel and a capacitor and short Warburg impedance element in parallel, is able to consistently fit the impedance of fuel cells in normal and fault conditions. The values of the fitted circuit parameters can give information about membrane resistivity, and can be used to consistently differentiate between the fault conditions studied. This method requires the acquisition of many data points in the 50 Hz to 50 kHz frequency range and an iterative fitting process and thus is more suitable for off-board diagnostic applications.

Monitoring the impedance of a fuel cell at 50 Hz, 500 Hz, and 5 kHz can also be used to differentiate between flooding, drying and CO poisoning conditions. The real and imaginary parts, and the phase and magnitude of the impedance can each be used to differentiate between faults. The real part of the impedance has the most consistent change with each fault at each of the three frequencies. This method is well suited to an

onboard diagnostic device because the data acquisition and fitting requirements are minimal.

Complete implementation of each of these methods into a final diagnostic device, be it onboard or off-board in nature, requires the development of reasonable threshold values. These threshold values can be developed through testing done at normal fuel cell operating conditions.

Table of Contents

List of Figures

List of Tables

Nomenclature

δ_c	Electrode thickness	cm
ε_o	Permittivity of vacuum	$8.85 \cdot 10^{-12}$ F·m^{-1}
ε_r	Dielectric constant of the electrolyte	1
θ	Phase shift	rads
ρ	Electrolyte resistivity	Ω·cm
$\rho_{r,c}$	Bulk resistivity of the electrode	Ω·cm
σ_E	Charge density at the electrode	C·cm^{-3}
σ_i	Variance of a parent distribution	1
τ_k	Relaxation time constant	s
φ	Phase of the impedance	degrees
Φ_e	Void fraction of the electrode	1
χ^2	Chi-squared statistical test results	1
ω	Angular frequency	rads·s^{-1}
A_{cell}	Active area of a cell	cm^2
C	Capacitance	F·cm^{-2}
C_{dl}	Double-layer capacitance	F·cm^{-2}
C_G	Geometric capacitance	F·cm^{-2}
d	Electrolyte membrane thickness	cm
d_N	Diffusion layer thickness	m
D_a	Diffusion constant of species a	m^2·s^{-1}
D_k	Diffusion constant of species k	m^2·s^{-1}
E	Potential	V
f_{top}	Frequency at the top of the first impedance feature	Hz
F_x	F-ratio value	1
h_c	Height of the flow channel	cm
h_p	Height of the flow-field plate	cm
i	Imaginary number ($\sqrt{(-1)}$)	1
I	Current	A
$Im(Z)$	Imaginary part of the impedance	Ω·cm^2
l	Length of the electrode	cm
j	Current density	A·cm^{-2}
j_f	Faradaic current density	A·cm^{-2}
L	Inductance	H·cm^2
n	Number of free parameters in a model	1
n_{cell}	Number of cells in a fuel cell stack	1
N	Number of data points	1
p_{fuel}	Fuel gas stream pressure	psig
p_{ox}	Oxidant gas stream pressure	psig
P	Set of model parameters	1
R	Resistance	Ω·cm^2
R_Ω	Ohmic resistance	Ω·cm^2
R_{ct}	Charge-transfer resistance	Ω·cm^2
R_{el}	Electron resistance	Ω

R_k	Relaxation resistance	Ω
R_m	Metal resistance	$\Omega \cdot cm^2$
R_{noise}	Resistance with noise added	$\Omega \cdot cm^2$
$R_{nonoise}$	Resistance without noise added	$\Omega \cdot cm^2$
R_p	Proton resistance	Ω
R_s	Electrolyte resistance	$\Omega \cdot cm^2$
R_t	Total resistance of the electrode	$\Omega \cdot cm^2$
$Re(Z)$	Real part of the impedance	$\Omega \cdot cm^2$
t	Time	s
T	Temperature	°C
T_{cell}	Fuel cell temperature	°C
T_{fuel}	Fuel gas stream temperature	°C
T_{ox}	Oxidant gas stream temperature	°C
T_w	Diffusion time scale	s
V	Voltage	V
V_{AC}	Amplitude of voltage perturbation	V
w_c	Width of the flow channel	cm
w_i	Statistical weighting coefficients	1
w_s	Width of the flow-field plate support	cm
W	Width of the flow-field plate	cm
Z	Impedance	$\Omega \cdot cm^2$
Z'	Real part of the impedance	$\Omega \cdot cm^2$
Z''	Imaginary part of the impedance	$\Omega \cdot cm^2$
Z_C	Impedance of a capacitor	$\Omega \cdot cm^2$
Z_{CPE}	Impedance of a constant phase element	$\Omega \cdot cm^2$
Z_i	Impedance of series element i	$\Omega \cdot cm^2$
Z_L	Impedance of an inductor	$\Omega \cdot cm^2$
Z_m	Measured impedance	$\Omega \cdot cm^2$
Z_R	Impedance of a resistor	$\Omega \cdot cm^2$
Z_t	Total impedance	$\Omega \cdot cm^2$
Z_{Wst}	Impedance of short terminus Warburg element	$\Omega \cdot cm^2$

Acknowledgements

I would like to thank my supervisors: Dr. David Harrington for his patience and willingness to help me understand just about anything that confused me as well as the consistent feedback that helped me find solutions to many problems, and Dr. Ned Djilali for helping me to gain a more global understanding of fuel cells and energy.

I would also like to thank Dr. Jean-Marc Le Canut for all his help and all the lab work that he has done. Without him not only would I have no data to work with but I would not understand impedance nearly so well. I would also like to thank him for all his patience with my numerous questions.

IESVic would not run as smoothly, nor would its graduate students ever know where they need to be and when, without the tireless work of Ms. Susan Walton. Her help and advice were invaluable in adjusting to life in Victoria and to graduate studies.

I would like to thank Greenlight Power Technologies for their technical and financial support of this work.

1 Introduction

This document outlines the processing and results of algorithm development for fuel cell diagnostics using electrochemical impedance spectroscopy (EIS) data. This work deals primarily with the data analysis aspects of EIS for fuel cell diagnostics. While the experimental aspects are outside the scope of this work, a thorough explanation of the experimental methods, artifact removal, and reasons for experimental conditions for the data analyzed in the work can be found in references 1-5.

EIS is useful as a diagnostic tool for fuel cells because it is essentially quite non-invasive. Fuel cells are sensitive to anything going on inside the sealed cell. The addition of instrumentation inside the cell can affect the fuel cell operation making it difficult to interpret whether effects in acquired data are due to poor fuel cell operation or instrumentation effects on fuel cell operation. While this can still be a concern with EIS, it is a much smaller one because there is not instrumentation needed inside the cell and the AC voltage perturbation across the cell is of a small magnitude. Furthermore, the techniques measures the condition of the fuel cell while operating.

This work focuses on the ability to identify multiple failure modes with a single experimental technique, EIS. EIS has been shown (refs. 1-5) to have generic behaviour for a variety of MEA types and cell and stack configurations. The EIS diagnostic technique is here investigated as a globally applicable diagnostic technique for fuel cells but it is anticipated that final algorithms and failure threshold values will need to be tuned to specific PEM fuel cells. Because of this, this work focuses on the identification of general trends and algorithms rather than on specific threshold values for our single cell test assembly.

Flooding, drying, and CO poisoning were assumed to be the only fuel cell failure modes for the purposes of this work. This was done because these are among the most well understood and well documented failure modes; also the number of failure modes examined was kept to a minimum to maintain a reasonable scope.

The algorithm development has taken two primary approaches: off-board and on-board diagnostic systems. Off-board diagnostics refers to diagnostic situations where the instrumentation for acquiring impedance information is separate from the fuel cell module (e.g., a fuel cell test station). Off-board diagnostic systems would be most useful in product design, quality testing, and optimization. They could also be used to diagnose less common failures. In an off-board situation there is the opportunity to have more operator interaction with data fitting and acquisition as well as the opportunity for more data acquisition and analysis. In this work, algorithms for off-board diagnostics with EIS are discussed primarily in the context of equivalent circuit modeling.

On-board diagnostics are integrated into the fuel cell module (balance of plant) system. This type of device would be used primarily to detect fault conditions during fuel cell operation and initiate procedures either to fix the fault condition or shut down fuel cell operation. The multi-frequency analysis modeling focuses primarily on onboard diagnostic applications.

1.1 Introduction to Fuel Cells

A fuel cell is essentially an electrochemical generator. All fuel cells are fed fuels and produce electricity through an electrochemical reaction. There are several different types of fuel cells currently being investigated for commercial viability. They essentially fall into two categories; high and medium temperature fuel cells, and low temperature fuel cells. The proton exchange membrane fuel cell, also known as the polymer electrolyte membrane fuel cell (PEMFC) is the fuel cell being studied in this work and will be further described in Section 1.1.3.

1.1.1 High and Medium Temperature Fuel Cells

Table 1-1 summarizes the operating characteristics of high and medium temperature fuel cells. There are two primary high temperature fuel cell types: molten carbonate fuel cells (MCFC) and solid oxide fuel cells (SOFC). They are both considered primarily for larger

scale (MW) stationary power applications. The two primary advantages of high temperature fuel cells are their ability to internally process fuels such as natural gas without concerns about catalyst poisoning, and the high efficiencies they are able to achieve particularly through the reuse of excess heat and in combined heating and power (CHP) applications. They require high temperatures to operate (Table 1-1) and cannot quickly be turned off or on which makes them practical primarily for the stationary power sector.

Phosphoric acid fuel cells (PAFC) are considered to be medium temperature fuel cells. They are currently one of the more commercially viable fuel cell system with approximately 200 units currently operating worldwide as stationary power, particularly as backup power systems.

Table 1-1: Summary of High and Medium Temperature Fuel Cell Characteristics [6,7,8,9]

Fuel Cell Type	Phosphoric Acid Fuel Cell	Molten Carbonate Fuel Cell	Solid Oxide Fuel Cell
Abbreviation	PAFC	MCFC	SOFC
Operating Temperature	~220 °C	~650 °C	~1000 °C
Electrolyte	Phosphoric Acid	Lithium and Potassium Carbonate	Solid Oxide Electrolyte (yttria,zirconia)
Charge Carrier	H^+	CO_3^{2-}	O^{2-}
Fuel	Pure H_2 (some (~1%) CO_2 tolerance)	H_2,CO,CH_4, other Hydrocarbons	H_2,CO,CH_4, other Hydrocarbons
System Efficiency	40%	>50%	>50%
Power Range	10kW-1MW	10kW-2MW	2kW-1MW
Application	CHP medium scale power generation	CHP and stand alone large scale power generation	CHP and stand alone medium to large scale power generation
Advantages	commercially available, market presence, proven life.	high efficiency, internal fuel processing, high grade heat waste	high efficiency, internal fuel processing, high grade waste heat
Disadvantages	relatively low efficiency, limited lifetime	lifetime undetermined, electrolyte instability, CO_2 poisoning	high operating temperature (materials), High cost
Anode Reaction	$H_2(g) \rightarrow 2H^+(aq) + 2e^-$	$H_2(g) + CO_3^{2-} \rightarrow H_2O(g) + CO_2(g) + 2e^-$	$H_2(g) + O_2^- \rightarrow H_2O(g) + 2e^-$
Cathode Reaction	$\frac{1}{2}O_2(g) + 2H^+(aq) + 2e^- \rightarrow H_2O(l)$	$\frac{1}{2}O_2(g) + CO_2(g) + 2e^- \rightarrow CO_3^{2-}$	$\frac{1}{2}O_2(g) + 2e^- \rightarrow O^{2-}$
Cell Reaction	$H_2(g) + \frac{1}{2}O_2(g) \rightarrow H_2O(l)$	$H_2(g) + \frac{1}{2}O_2(g) \rightarrow H_2O(g)$	$H_2(g) + \frac{1}{2}O_2(g) \rightarrow H_2O(g)$

1.1.2 Low Temperature Fuel Cells

There are three primary types of low temperature fuel cells: the direct methanol fuel cell (DMFC) , the alkaline fuel cell (AFC) and the proton exchange membrane fuel cell (also known as the polymer electrolyte membrane fuel cell)(PEMFC) .

Table 1-2: Summary of Low Temperature Fuel Cell Characteristics [6,7,8,9]

Fuel Cell Type	Proton Exchange Membrane Fuel Cell	Direct Methanol Fuel Cell	Alkaline Fuel Cell
Abbreviation	PEMFC	DMFC	AFC
Operating Temperature	60-120 °C	70-90 °C	50-200 °C
Electrolyte	Solid Polymer (i.e. Nafion)	Solid Polymer	KOH
Charge Carrier	H^+	H^+	OH^-
Fuel	Pure H_2 (some CO_2 tolerance)	Pure H_2 (some CO_2 tolerance)	Pure H_2
System Efficiency	35-45%	35-40%	35-55%
Power Range	5-250 kW	<1 kW	<5kW
Desired Application	Transportation, portable, and low power CHP applications	Transportation and portable applications	Space (NASA) and some other transportation
Advantages	high power densities, proven long operating life, adoption by automakers	reduced system complexity (fuel reforming, compression, and humidification are eliminated)	inexpensive materials, CO tolerance, fast cathode kinetics
Disadvantages	lack of CO tolerance, water and heat management, expensive catalyst	anode kinetics, cross-over, complex stack structure, noble catalyst required	corrosive liquid electrolyte, lack of CO_2 tolerance
Anode Reaction	$H_2(g) \rightarrow 2H^+(aq) + 2e^-$	$CH_3OH(aq) + H_2O(l) \rightarrow CO_2(g) + 6H^+(aq) + 6e^-$	$H_2(g) + 2(OH)^-(aq) \rightarrow 2H_2O(l) + 2e^-$
Cathode Reaction	$½O^2(g) + 2H^+(aq) + 2e^- \rightarrow H_2O(l)$	$6H^+(aq) + 6e^- + 3/2\ O_2(g) \rightarrow 3H_2O(l)$	$½O_2(g) + H_2O(l) + 2e^- \rightarrow 2(OH)^-(aq)$
Cell Reaction	$H_2(g) + ½O_2(g) \rightarrow H_2O(l)$	$H_2(g) + ½O_2(g) \rightarrow H_2O(l)$	$H_2(g) + ½O_2(g) \rightarrow H_2O(g)$

AFCs were used by NASA for space missions, before NASA switched to PEMFCs. AFCs were too expensive to be commercially viable for a long time but are currently being investigated by several companies.

DMFCs are essentially quite similar to PEMFCs, and are currently being investigated mostly for small portable power applications (i.e. laptop, cell phone, PDA, etc. battery replacement). They are still encountering problems with fuel crossover.

1.1.3 Proton Exchange Membrane Fuel Cell (PEMFCs)

PEMFC are currently being widely studied for use in a variety of transportation and stationary applications.

Each cell in a PEMFC consists of two flow-field or collector plates (Figure 1.1) with a membrane electrode assembly (MEA) (Figure 1.1) sandwiched between them (Figure 1.2). The MEA consists of a solid polymer electrolyte with a catalyst layer and a gas diffusion layer (GDL) on each side. Generally the electrolyte is a solid polymer such as Nafion®, the catalyst is carbon-supported platinum and the GDL is a woven or felted material made of graphite fibers.

Hydrogen and oxygen (in the form of air or pure O_2) are fed to the fuel cell through gas flow channels on the anode and cathode flow-field plates respectively. At the anode, hydrogen diffuses through the GDL to the catalyst layer and undergoes the following reaction:

$$H_2(g) \rightarrow 2H^+(aq) + 2e^- \qquad \textbf{Eq 1-1}$$

The product protons pass through the solid polymer electrolyte membrane and the electrons are forced through an external circuit, producing electricity.

At the cathode, oxygen diffuses through the GDL to the catalyst layer where it undergoes the following reaction:

$$\tfrac{1}{2}O_2(g) + 2H^+(aq) + 2e^- \rightarrow H_2O(l) \qquad \textbf{Eq 1-2}$$

Here each oxygen atom pairs with two protons, which have passed through the electrolyte membrane, and two electrons, which have been forced through the external circuit, to form a water molecule.

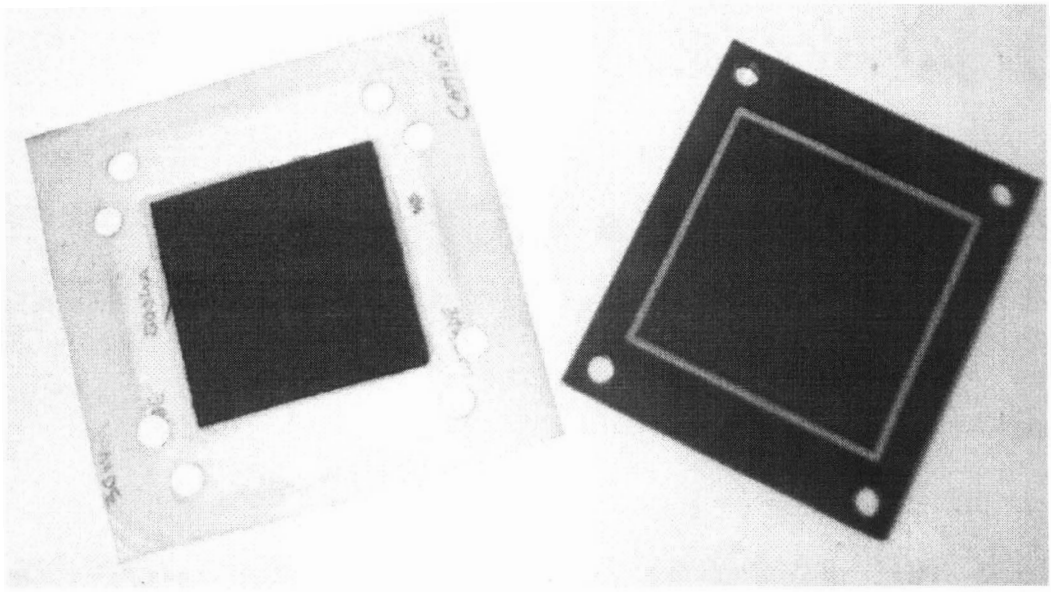

Figure 1.1: Membrane Electrode Assembly (left) and Graphite Flow-field Collector Plate (right) with Light Coloured Gasket.

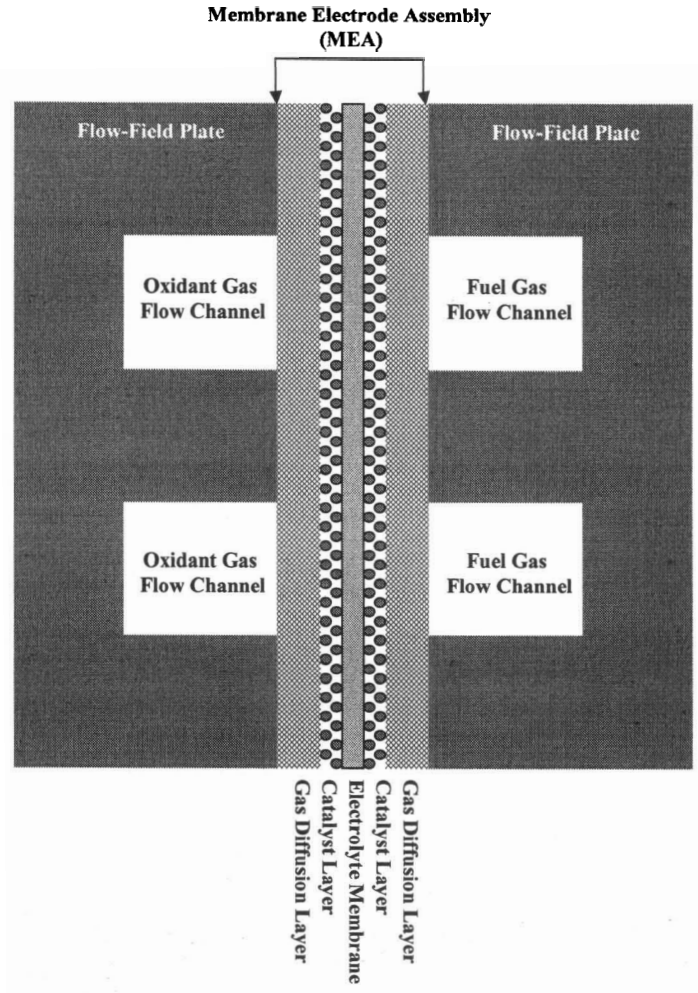

Figure 1.2: Single Cell Fuel Cell Assembly Cross Section

1.2 Fuel Cell Diagnostics

As with any other device there is an interest in knowing when and why a fuel cell is not operating properly. This is information that needs to be understood not only for testing and prototype development but also for quality control and monitoring during production. This type of information is also needed for control and monitoring of onboard systems to prevent catastrophic failure, or to correct poor operating conditions before equipment is damaged.

The purpose of this work is to develop algorithms to identify fuel cell fault behaviour, specifically using electrochemical impedance spectroscopy data from fuel cells under

fault conditions. This has been done to assist with the development of both onboard and off-board fuel cell diagnostic hardware.

For the purposes of this work, an off-board diagnostic device would be external to the fuel cell system and would be used to monitor fuel cell operation in specific settings where there is more time and operator involvement. This would be similar to vehicle diagnostic computers used currently by auto mechanics. An onboard diagnostic device would be small and simple in order to be integrated into the fuel cell control system, not only to identify which fault has occurred but also to initiate measures to resolve problems before failure.

1.3 Background on fuel cell faults

Like any other device, there are many ways that a fuel cell can fail. Some possible mechanical failures in fuel cells include cracked flow-field plates, ruptured membranes or leaking gaskets. In addition to mechanical failure, fuel cells are also susceptible to several failure modes that either prevent the electrochemical reactions from occurring or slow them down. These "electrochemical" faults can include problems with water management such as the flooding of the electrode or the drying of the membrane as well as poisoning of the catalyst layer. These last three faults were the focus of this work and are described further below. Membrane/catalyst ageing is also a possible electrochemical fault but it is not examined in this work.

1.3.1 Fuel Cell Water Management Faults

Water management and water transport in the membrane have been extensively studied in an effort to improve fuel cell performance and prevent drying and flooding failure. Further information about fuel cell failures and their identification can be found in Larminie and Dicks[7], Mérida[1], and Hoogers[6].

1.3.1.1 Flooding

As a product of the PEMFC reaction, water is produced at the fuel cell cathode. If the fuel cell is working well, the water is either used to properly humidify the polymer electrolyte membrane, or it is evaporated and carried away by the oxidant stream, leaving the fuel cell as water vapor. If this is not happening water can build up in the pores of the gas diffusion electrodes and in the flow channels, preventing the diffusion of gases to the electrode. In extreme cases the water buildup can completely block the flow channel. It has been shown[10] that the buildup of water in the flow channel to the point of blockage is responsible for the characteristic saw-tooth voltage profile that is associated with cathode flooding behaviour[1]. This voltage profile is quite different from the voltage behaviour of other faults examined; it could be used as another diagnostic method for flooding identification.

1.3.1.2 Drying

Polymer electrolyte membranes such as Nafion® need to be well humidified in order to function properly. If the reactant gas streams are not sufficiently humidified, or if the fuel cell temperature is kept too high, water in the membrane evaporates into the gas stream and is removed from the fuel cell.

If there is a net flux of water out of a particular region in the membrane, then the membrane resistivity in that area increases. As the resistivity of the region increases, the thermal stresses also increase. If the temperature in the drying regions increases to the melting point of the membrane material (usually referred to as "brown out conditions") then the membrane can burn and rupture. In these conditions not only is the ionic conductivity of the membrane compromised, the reactant streams may mix in possibly explosive ratios.

Drying is typically characterized by a decrease in voltage over time (Figure 3.6 and Figure 3.9) Further information about the pathological effects of membrane drying can be found in the work of Walter Mérida[1]. EIS has been used previously as a method for

measuring membrane resistance, it is often assumed that the real part of an impedance measurement at 1kHz is representative of the membrane resistance.[11] Water vapor sensors can be diagnostic of the conditions leading to membrane drying, but EIS directly measures the state of the membrane.

1.3.2 Catalyst Poisoning Faults

A number of materials can poison the platinum catalyst and affect fuel cell operation. CO, HCHO, HCOOH, and other molecules can all effectively poison the catalyst layer by occupying catalyst sites that could otherwise be used for the PEMFC reaction. This is of concern because hydrogen produced through reforming (particularly in onboard systems) often contains these agents. This work only examines the poisoning effects of the CO molecule.

The rate of catalyst poisoning is dependant on the concentration of the poisoning agent in the gas stream. Catalyst poisoning, like drying, is characterized by a decrease in voltage with time (Figure 3.15). Almost full recovery from CO poisoning conditions can be achieved by the addition of a small amount of oxygen (typically >1% air) to the fuel stream. During air bleed the oxygen bonds with the CO to produce CO_2, thus freeing the occupied catalyst sites.

Another diagnostic method for CO is to create a condition where CO would be stripped from the anode and see if recovery occurs. If so there was CO poisoning; if not another fault. Two methods of doing this are bleeding air into the fuel gas stream[12] and applying positive potential excursions to the anode.

2 Electrochemical Impedance Spectroscopy (EIS)

EIS is a very useful fuel cell diagnostic tool because it is non-invasive and can indicate information about the status of elements inside the fuel cell (e.g., the membrane). Fuel cells are sensitive to anything inside the cell, so it is difficult to determine if data from instrumentation inside the cell is due to cell behaviour or due to the perturbing presence of the instrumentation. EIS avoids this problem because it requires no instrumentation inside the cell and the amplitude of the AC perturbation is small. EIS, as a single technique, is able to identify several different failure modes. This makes if appealing because, even though the instrumentation required for EIS can be cumbersome and expensive, only one on-board diagnostic system is required.

Electrochemical impedance spectroscopy (EIS) was traditionally applied to the determination of the double layer capacitance and in AC polarography[13,14]. Currently EIS is used primarily to characterize the electrical properties of materials and interfaces with electrically conducting electrodes[15]. EIS studies the system response to the imposition of a small amplitude AC signal. Impedance measurements are taken at various frequencies of applied AC signal. EIS has been shown to be effective in identifying fuel cell fault conditions[1].

2.1 Impedance

Within this work $i=\sqrt{-1}$.

An AC voltage (Eq 2-1) of a known frequency ω and magnitude V is imposed over a DC voltage V_{DC} in a cell.

$$V(t) = V_{DC} + V_{AC}\sin(\omega t)$$

Eq 2-1

The resulting AC current (Eq 2-2) is measured and compared to the incoming signal. θ is the phase difference between the applied voltage ($V(t)$) and the measured current ($I(t)$).

$$I(t) = I_{DC} + I_{AC}\sin(\omega t + \theta)$$

Eq 2-2

The impedance of the system (Eq 2-3) , $Z(\omega)$, is defined as the ratio of the applied voltage, in the frequency domain,($v(\omega)$) to the measured current ($i(\omega)$)

$$Z(\omega) \equiv \frac{v(\omega)}{i(\omega)}$$

Eq 2-3

Impedance is a complex number:

$$Z = Z' + i \cdot Z''$$

Eq 2-4

The magnitude of impedance, $|Z|$, can be expressed as follows:

$$|Z| = \sqrt{(Z')^2 + (Z'')^2}$$

Eq 2-5

The phase of the impedance φ is defined as:

$$\varphi = -\tan^{-1}\left(\frac{Z''}{Z'}\right)$$

Eq 2-6

Where the negative sign is conventionally added to give a positive phase when Z' is positive and Z'' is negative.

To facilitate comparison, in this work impedance is shown scaled to a single cell in a fuel cell with a surface area of 1.0 cm^2. The impedance was first scaled to the cell area (A_{cell}) by multiplying the measured impedance (Z_m) by the cell area to determined the scaled impedance (Z):

$$Z = Z_m \cdot A_{cell}$$

Eq 2-7

In the case of data acquired from the 4-cell stack assembly, the data is also scaled by the number of cells:

$$Z = \frac{Z_m \cdot A_{cell}}{n_{cell}}$$

Eq 2-8

where n_{cell} is the number of cells in the stack.

Because all impedances are scaled to area the impedance units are consistently in $\Omega \cdot cm^2$.

In a practical device, the ability to detect a fault occurring in a single cell of a large stack is required. More stack data under actual operating conditions is required to effectively determine if EIS has this ability, and to determine how accurately a fault can be detected with a given number of cells. This question is considered in the for membrane resistance in Section 6.

Impedance data is typically represented in two types of plots: the Nyquist/Argand Plot and the Bode Plot.

The Nyquist Plot, is a graphical portrayal of complex numbers in the Argand plane; where the X-axis represents the real part and the Y-axis represents the imaginary part of the complex number. In the case of plotting impedance data, the positive Y-axis conventionally represents the negative imaginary portion of the impedance and there is a complex impedance point for every frequency at which the impedance was measured, creating a plot with impedance features. The shape of these impedance features is what is indicative of failure modes in fuel cell impedance and is further discussed in Section 3.

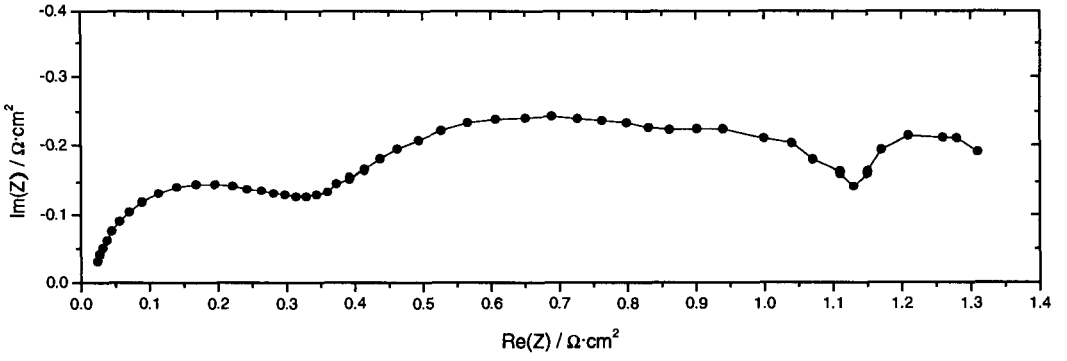

Figure 2.1: Nyquist/Argand representation of a typical fuel cell impedance spectrum (See Section 3.3)

The Bode Plot consists of two graphs: one with the phase of the admittance (the negative phase of the impedance) (φ) on the Y-axis and the logarithmic frequency ($\log_{10}(\omega)$) on the X-axis, the other with the log of the magnitude of the impedance ($\log_{10}|Z(\omega)|$) on the Y-axis and the logarithmic frequency ($\log_{10}(\omega)$) on the X-axis.

The majority of the fitting for this work was done using the Nyquist/Argand representation of measured impedance spectra. This is because there are characteristic impedance shapes which are much more evident in this representation.

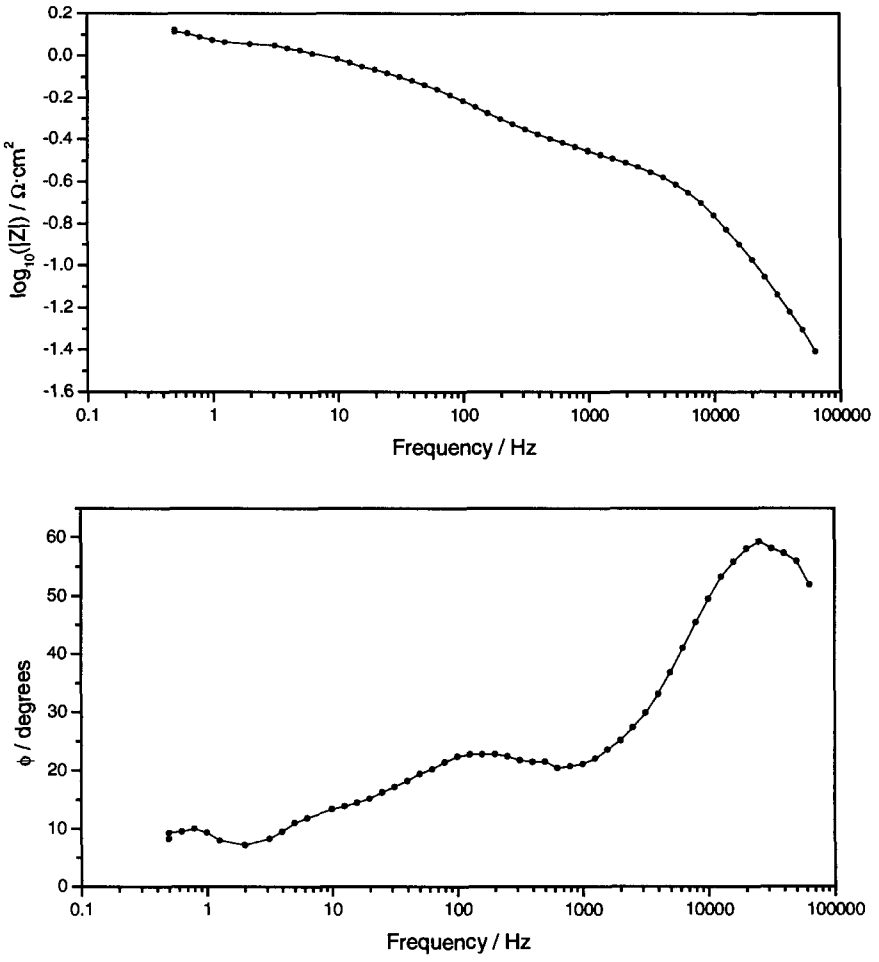

Figure 2.2: Bode Plot representation of a typical fuel cell impedance spectrum (See Section 3.3)

2.2 Equivalent Circuit Fitting

Equivalent circuits are traditionally used to model AC impedance data[13,14,15,16]. An equivalent circuit is an electrical circuit with the same impedance spectrum as the experimental data. The values and arrangement of the circuit elements ideally represent physical properties or phenomena. Changes in the values of circuit elements can help in understanding system response.

2.2.1 Background on equivalent circuit elements

2.2.1.1 Resistors

Eq 2-9 shows the expression for the impedance of a pure resistor, where R is the resistance.

$$Z_R = R$$

Eq 2-9

In the Nyquist plane a pure resistor appears as a single point on the real axis (Figure 2.3).

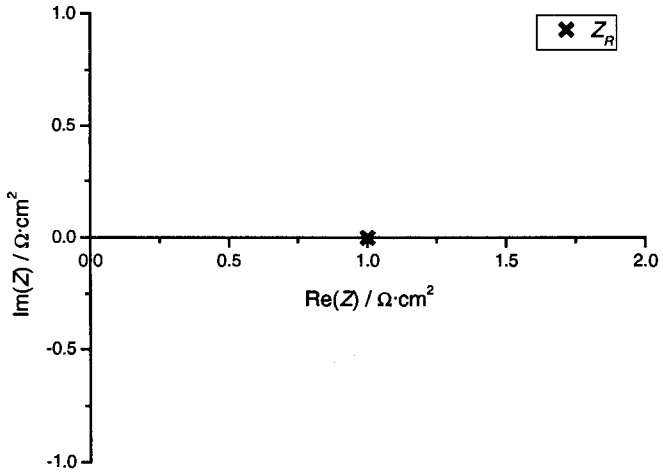

Figure 2.3: Nyquist Representation of the Impedance of a Pure Resistance (R=1Ω·cm^2).

There are two primary types of resistances investigated for the equivalent circuit modeling of fuel cells in this work: the electrolyte resistance and the charge transfer resistance.

2.2.1.1.1 Electrolyte Resistance[14,15]

The electrolyte resistance (R_s), also referred to as the solution resistance, is the resistance to current flow through the electrolyte. It is proportional to the electrolyte resistivity ρ, and is dependant on the cell geometry (planar in this case) where d is the thickness of the electrolyte (Eq 2-10).

$$R_S = \rho \cdot d$$

Eq 2-10

The resistance to current flow, in the metal of the electrode, is referred to as the metal resistance (R_M). The ohmic resistance (R_Ω) is the sum of the electrolyte resistance and the metal resistance (Eq 2-11).

$$R_\Omega = R_s + R_m$$

Eq 2-11

2.2.1.1.2 Charge-Transfer Resistance[14,15,17]

The charge transfer resistance (R_{ct}) is the resistance associated with the charge transfer mechanism for electrode reactions. This is the resistance to electrons crossing the interface. It is defined as the partial derivative of the faradaic current density (j_F) with respect to potential (E) (Eq 2-12):

$$R_{ct} = \left(\frac{\partial j_F}{\partial E} \right)^{-1}$$

Eq 2-12

2.2.1.2 Capacitors

Eq 2-13 shows the expression for the impedance of a pure capacitor, where C is the capacitance:

$$Z_C = (\mathrm{i} \cdot \omega \cdot C)^{-1}$$

Eq 2-13

The impedance of a pure capacitor is entirely imaginary and negative (Figure 2.4).

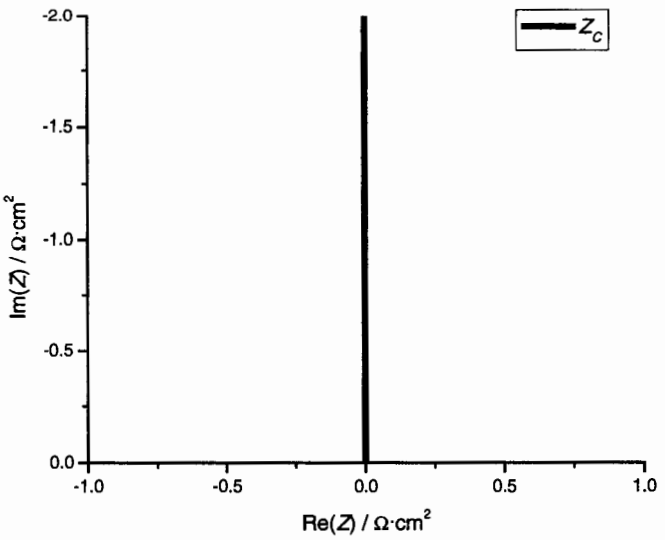

Figure 2.4: Nyquist Representation of the Impedance of a Pure Capacitance (C=1 F·cm^{-1}).

There are two primary types of capacitances investigated for the equivalent circuit modeling of fuel cells in this work: the double-layer capacitance and the geometric (bulk) capacitance.

2.2.1.2.1 Double-Layer Capacitance[14,15]

The double layer capacitance (C_{dl}) arises from an electrical double-layer that forms at the interface between the electrode and the electrolyte. Eq 2-14 shows the expression for the double-layer capacitance where σ_E is the charge density at the electrode, E is the interfacial potential, T is the temperature, p is the pressure, and μ is the chemical potential:

$$C_{dl} = \left(\frac{\partial \sigma_E}{\partial E} \right)_{T,p,\mu}$$

Eq 2-14

2.2.1.2.2 Geometric Capacitance[14,15]

The geometric (bulk) capacitance (C_G) is the capacitance that arises between the two electrodes in an electrochemical cell. In Eq 2-15, d is the characteristic distance between

the two electrodes, ε_r is the dielectric constant of the electrolyte, and ε_o is the permittivity of vacuum:

$$C_G = \frac{\varepsilon_o \cdot \varepsilon_r}{d}$$

Eq 2-15

2.2.1.3 Inductors

Eq 2-16 shows the expression for the impedance of a pure inductor, where L is the inductance:

$$Z_L = i \cdot \omega \cdot L$$

Eq 2-16

The impedance of a pure inductor is entirely imaginary and positive (Figure 2.5).

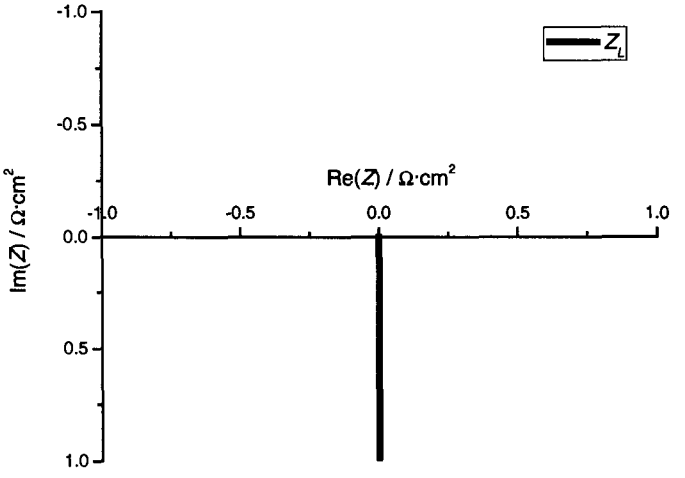

Figure 2.5: Nyquist Representation of the Impedance of a Pure Inductor (L= 1 H.cm^{-1})

Inductive behaviour in EIS data is often attributed to be an artifact due to cabling or electrical equipment[18].

2.2.1.4 Distributed Elements

Combinations of purely resistive, capacitive, or inductive behaviours do not necessarily describe the response of all systems: to account for this distributed elements are used to

model behaviour. There are two principal forms of distributed elements that are closely related: the constant phase element (CPE) and the Warburg element.

2.2.1.4.1 Constant Phase Elements (CPEs)

The impedance of a constant phase element (CPE) is expressed as follows, where T and φ are CPE parameters:

$$Z_{CPE} = (T(i \cdot \omega)^{\phi})^{-1}$$

Eq 2-17

The CPE can be used to describe pure resistor ($\varphi = 0$, $T = R^{-1}$), a pure capacitor ($\varphi = 1$, $T = C$), or a pure inductor ($\varphi = -1$, $T = L^{-1}$). It is also associated with the Warburg element if $\varphi = 0.5$.

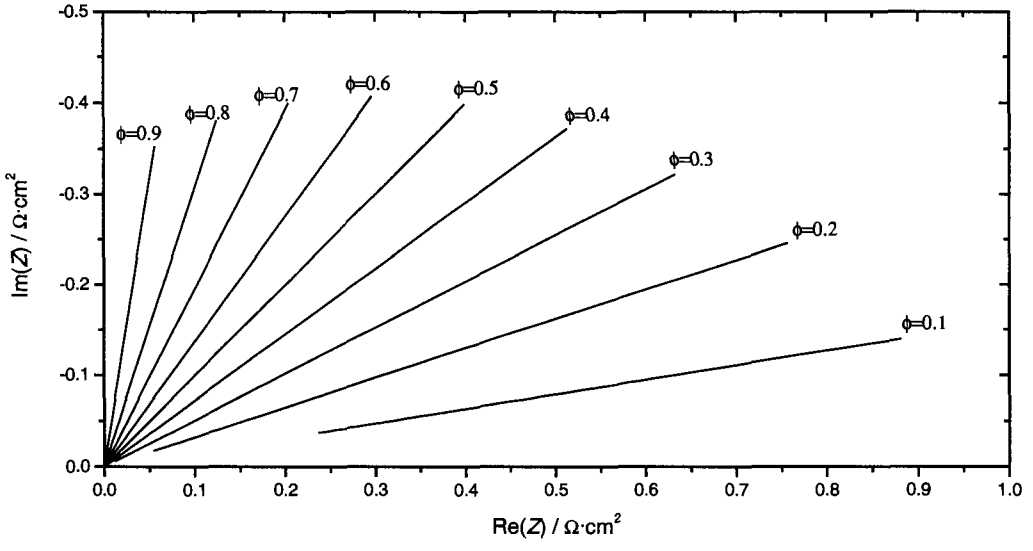

Figure 2.6: Nyquist Representation of Impedance of CPE with Varying φ Parameter (T Parameter = 1 F·cm^{-1}·s$^{-\varphi}$) for f = 0.5Hz to 25 kHz.

In general the impedance of CPEs is used to describe the double layer charging characteristics of rough irregular electrode surfaces. The true physical significance of the CPE with $\varphi \neq -1$, 0, 0.5, or 1 has yet to be resolved but there are numerous attempts at explanations for the physical meaning of CPEs.[13-15, 19-32]

2.2.1.4.2 Warburg Elements [13,14,15,17,33]

The Warburg impedance is the impedance arising from one-dimensional diffusion of a species to the electrode. The general case, describing the effect of the diffusion of species a, is shown in Eq 2-18 where σ_a is a Warburg parameter, dependant on the diffusivity of species a, the reaction rate, the concentration of species a, the current density, and the potential.

$$Z_{W,a} = \sigma'_a (i \cdot \omega)^{-1/2} = \frac{\sigma_a}{\omega^{1/2} \cdot (1+i)}$$

Eq 2-18

Using a finite length diffusion boundary condition, over a diffusion length of δ, can be used to derive the short terminus Warburg element (STWE). Eq 2-19 describes the impedance of the STWE where R_w is a Warburg R parameter, and T_w is described in Eq 2-20 where D_a is the diffusivity of species a.

$$Z_{Wst} = \frac{R_w \cdot \tanh\left[(i \cdot T_w \cdot \omega)^{\phi}\right]}{(i \cdot T_w \cdot \omega)^{\phi}}$$

Eq 2-19

$$T_w = \frac{\delta^2}{D_a}$$

Eq 2-20

A short terminus Warburg element acts like a resistor at low frequencies and has a characteristic "45 degree angle" behaviour at high frequencies (Figure 2.7). For pure diffusive behaviour the φ parameter is fixed at 0.5 but for fitting purposes in this work it is usually allowed to be a free parameter.

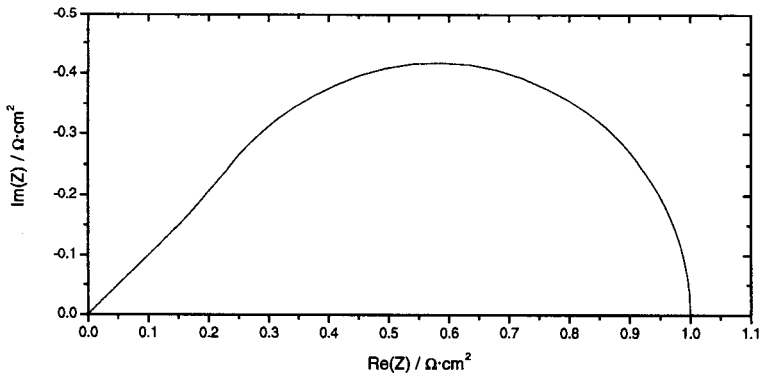

Figure 2.7: Nyquist Representation of Short Terminus Warburg Element (STWE) with R = 1 Ω·cm², T = 1 s, and φ = 0.5.

It was of interest to determine the effect of an increase of any individual parameter (*R, T* or φ) on the shape of the impedance. In Figure 2.8, Figure 2.9, and Figure 2.10, a single parameter is changed while the others were kept constant. Constant values of Warburg R = 0.5 Ω·cm², Warburg T = 0.01 s, and Warburg φ = 0.28 were used to simulate the impedance of the 7 parameter model from Section 4.5.4.2. Other parameters used were: $R1$ = 0.0225 Ω·cm², $R2$ = 0.3 Ω·cm², $C1$ = 0.00013 F·cm^{-2}, and $C2$ = 0.0004 F·cm^{-2}. These parameters were determined using the average of the parameters determined through fitting with the 7 parameter model (Section 4.5.4.2) for the normal operating conditions impedance from the Drying 1, Drying 2, and CO Poisoning datasets (Sections 3.4.1, 3.4.2, and 3.6 respectively. The simulated impedance with the averaged parameters is portrayed as a heavier line in Figure 2.8, Figure 2.9, and Figure 2.10.

As the Warburg R parameter increases (Figure 2.8) the diameter of the "semicircle" affected by the Warburg Impedance grows, effectively increasing the real part of the impedance or the resistive behaviour.

As the Warburg φ parameter increases (Figure 2.9) the curvature of the arc affected by the Warburg impedance increases, effectively changing the imaginary part of the impedance significantly more than the real part.

As the Warburg T parameter increases (Figure 2.10) the diameter of the "semicircle" affected by the Warburg impedance gets smaller, effectively decreasing the real part of the impedance at lower frequencies.

All of these parameters also affect the overlap between the impedance features associated with the Warburg element and other impedance features. This is of interest because this overlap is affected greatly during CO poisoning but less so during drying.

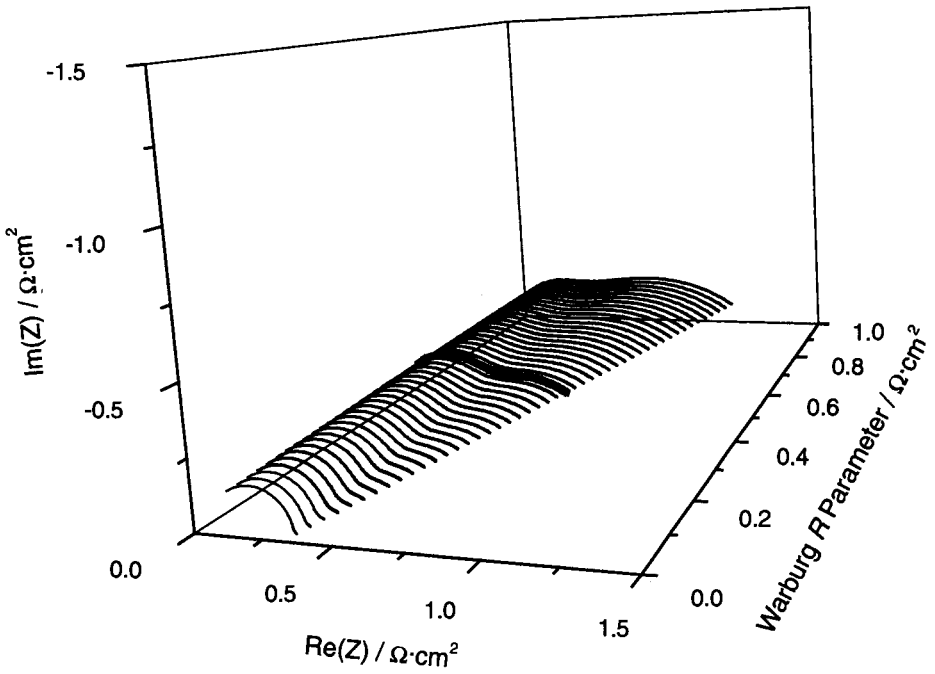

Figure 2.8: Change in impedance shape of simulated Model 2 impedance with changing Warburg R parameter

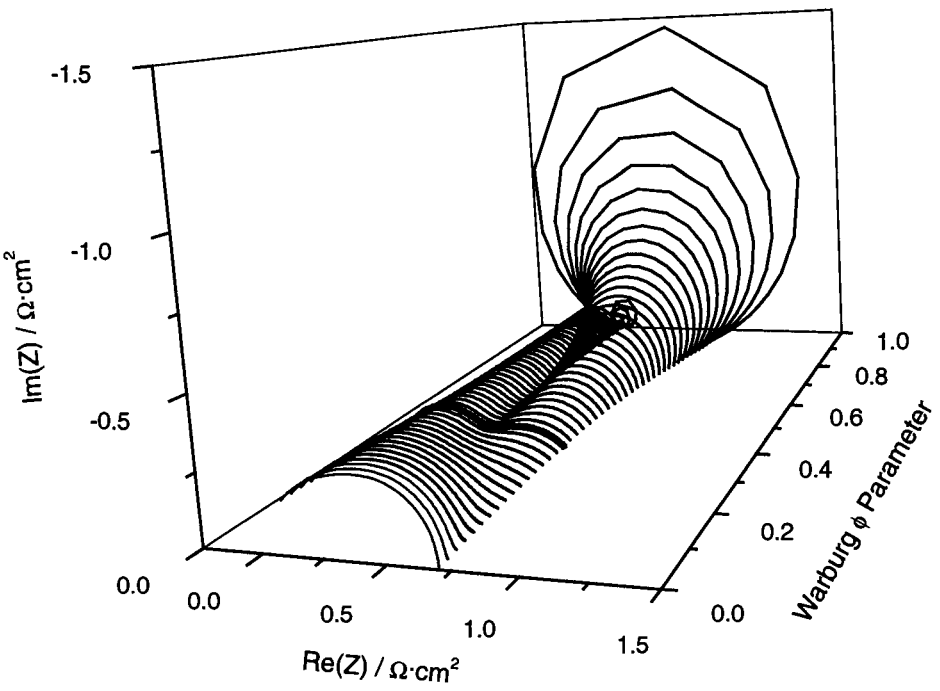

Figure 2.9: Change in impedance shape of simulated Model 2 impedance with changing Warburg φ parameter

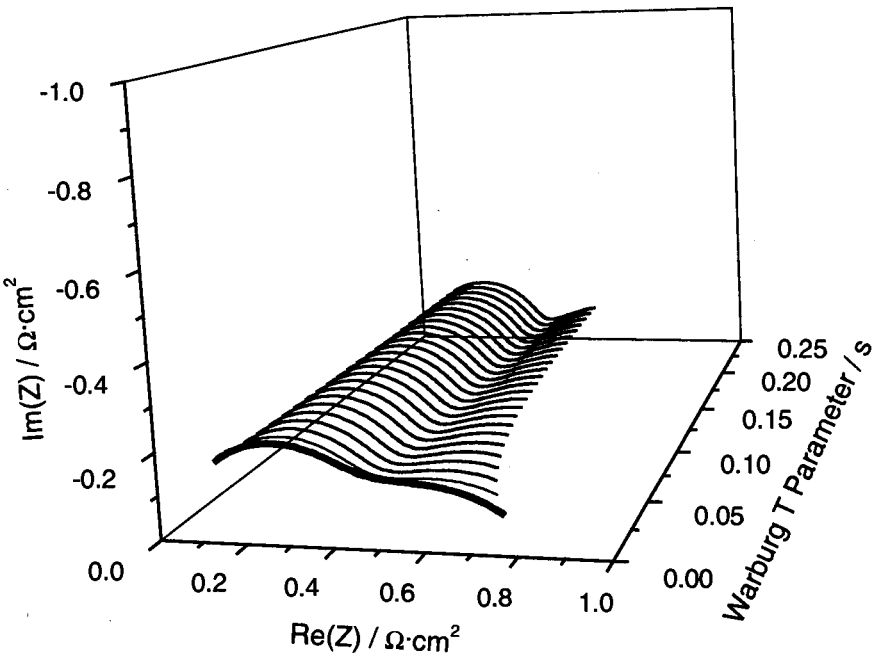

Figure 2.10: Change in impedance shape of simulated Model 2 impedance with changing Warburg T parameter

2.2.2 Circuit Ambiguity

One of the problems with the use of equivalent circuit fitting is that equivalent circuit models can be non-unique; different circuits can have the same impedance signature (Figure 2.11).

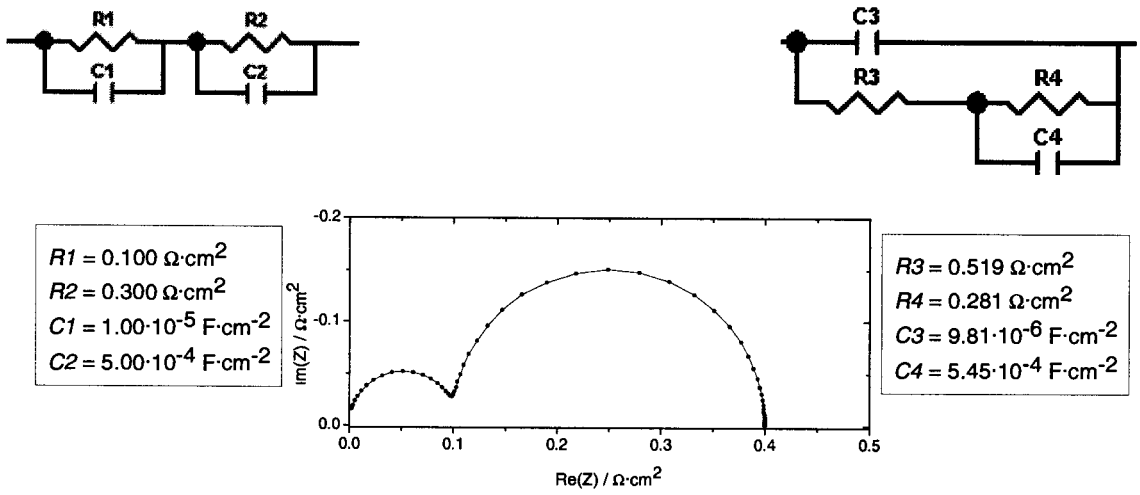

Figure 2.11: Different circuits and their parameters with the same impedance signature

The possibility of multiple configurations with the same impedance signature can lead to questions about the physical significance of model parameters. Circuit models do not always need to have clear physical significance to be used as a data-fitting tool. If there is not a clear matching of circuit elements with physical elements, then a "cross coupling" of elements can occur making it hard to distinguish between two physical changes, and leading to ambiguities about the significance of fit parameters.

2.2.3 Fitting Algorithms

2.2.3.1 Complex Non-Linear Least Squares (CNLS) Algorithm

The complex nonlinear least squares (CNLS) method is one of the most common approaches for modeling impedance data. This is partially due to commercial fitting programs like Zplot and LEVM which use the CNLS method. CNLS is used to fit the real

and imaginary parts or the magnitude and phase of experimental impedance or admittance data to an equivalent circuit or a rational function. It is a convenient method for fitting data to functions or circuits with many (upwards of 10) free parameters. The primary concerns with CNLS are its sensitivity to initial parameters, the correct choice of the number of free parameters, and the possibility of convergence to a local minimum. The choice of minimization algorithm is also an important consideration. Problems arise, particularly when the number of free parameters is large. In general CNLS the weighted sum of squares is minimized[15]:

$$S = \sum_{i=1}^{N} \{w_i^a [f_{ex}^a - f_{calc}^a(\omega_i, P)]^2 + w_i^b [f_{ex}^b - f_{calc}^b(\omega_i, P)]^2\}$$

Eq 2-21

where N is the number of data points and P is a set of model parameters. If the real and imaginary parts of the impedance are used for the fit, f_{ex}^a (f_{ex}^b) is the real (imaginary) part of the measured impedance at point i and f_{theo}^a (f_{theo}^b) is the real (imaginary) part of the theoretical impedance calculated at frequency ω_i. If the phase and magnitude are being used for the fit, f_{ex}^a (f_{ex}^b) is the magnitude (phase) part of the measured impedance at point i and f_{theo}^a (f_{theo}^b) is the magnitude (phase) part of the theoretical impedance calculated at frequency ω_i. Here w_i^a and w_i^b are the statistical weighting coefficients.

2.2.3.2 Weighting for CNLS fitting

The statistical weighting coefficients are important to CNLS fitting because measured data can often vary by several orders of magnitude over the frequency range acquired in a single experiment. When unit weighting is used ($w_i^a = w_i^b = 1$) and there is variation above one order of magnitude, the larger points tend to dominate the fitting. This creates poor convergence and poor parameter fits. Macdonald suggests several methods for weighting data such as proportional weighting[15] where the weighting for a point (w_i) is proportional to the square of the measured impedance (Z_i) at that point:

$$w_i = \frac{1}{(Z_i)^2}$$

Eq 2-22

In function proportional weighting[34, 35] the weighing is proportional to the function fitting parameters and thus varies with each fitting iteration. Boukamp suggests using modulus weighting[36] ($w_i = 1/(|Z_l| + |Z_h|)^{1/2}$) where $|Z_l|$ and $|Z_h|$ are the vector lengths of the impedance at the highest and lowest frequency. Another version of this method [36] uses $|Z_l|$ and $|Z_h|$ as the absolute values of the real and imaginary impedance function at a point.

The choice of weighting function will depend heavily on the characteristics and error distribution of the measured impedance data itself and the parameters being sought.

2.2.3.3 Initial Values for CNLS Fitting

Initial values are critical to the quality of fit of CNLS because of its iterative nature. If they are not close to the real values, the CNLS fit may not reach convergence. The fit may also converge on local, rather than global, minimum. One method for determining starting values is through trial and error; using several different sets of starting values in an attempt to reach convergence on a single circuit. If convergence is reached, to different parameters, with differing starting values the better starting values can be chosen by comparing the fit results with the χ^2 statistical test (Section 2.2.4.1).

Another method is to build the model by fitting fewer elements and adding on more until a model with good initial values is built. These methods will work on some equivalent circuits with a small number of elements or relatively predictable initial values, but are not efficient for more complex problems. Other methods used in the past are geometric interpolation and grid methods[37]

2.2.3.4 Minimizing Algorithms for CNLS

There are several algorithms that can be used to minimize CNLS fitting functions. The most commonly used algorithm in the software packages[38] is the Levenberg-Marquardt algorithm, but others like genetic algorithms and combinatorial optimization can also be

used depending on the number of allowable iterations and the quality of the initial parameters

In the gradient method, minima are found by finding the steepest slope and searching in that direction. This can be slow to converge. This method also has a relatively small search area and can easily converge on local minima. The Levenberg-Marquardt algorithm performs an interpolation between the Taylor series and the gradient methods of minimizing least squares functions [39]. In this algorithm the direction of search is determined by solving for the search vector. This algorithm only looks in the direction of the search vector. Because it only searched in one direction, convergence on a local minima rather than the global one is possible. It has the advantage of relatively fast convergence and relatively few iterations necessary, particularly if good initial values are provided.

2.2.4 Statistical Comparison

The objective of the statistical analysis in this work is to determine if the addition of an additional parameter to a model improves the fit of that model to a single spectrum in a statistically significant manner. Adding a parameter to a model usually gives a better fit (lower sum of squares) but this improvement may not always be statistically significant. To determine when the addition of a parameter is statistically significant, a statistical test on the F-ratio was applied.

2.2.4.1 Chi-Squared Test

The Chi-Squared Test is a measure of the goodness of fit of a model compared to experimental data. χ^2 is defined as follows:

$$\chi^2 \equiv \sum_{i=1}^{2N} \left\{ \frac{1}{\sigma_i^2} [y_i - y(x_i)]^2 \right\}$$

Eq 2-23

where i indexes individual data points, σ_i^2 is the variance of the parent distribution for each data point, y_i are the data, $y(x_i)$ are the fitted function values, and N is the number of frequencies at which the impedance was measured in a spectrum. In this case, for i=1...N, y_i will be the real part of the impedance for each individual frequency in the spectrum. For i=N+1...2N, y_i will be the imaginary part of the impedance for each individual frequency in the spectrum.

The error relating to the impedance at different frequencies is known to be uncorrelated. This error can depend on the measurement system, for example errors might depend on the magnitude of the signal measured due to range changing. One simple model could be that the percent error is constant for all data points, leading to a larger absolute error for larger impedances. Therefore the standard deviation for a replicate measurement can depend on the frequency. In general, there is a different parent distribution (and variance σ_i^2) for each frequency. Furthermore the errors in the real and imaginary part of the data points at each frequency are known to be uncorrelated for impedance data acquired with an FRA setup[40] but correlated for impedance acquired with a lock-in amplifier setup[41]. All spectra used for statistical comparison were acquired with the FRA setup (Section 3.1.3.1).

In the fitting scheme the weighting for a given data point i should be chosen to be inversely proportional to the known or estimated variance σ_i^2. Since in our case, the magnitude did not change significantly with frequency, unit weighting was chosen. This implicitly assumes that σ_i is independent of i, allowing for the comparison of the fit of an individual spectrum to several models with the F-test. Under these assumptions the χ^2 and sum of squares quantities are proportional.

2.2.4.2 F- Test for Additional Terms

Normally the F-test is used to test if two observed standard deviations come from the same population. For data regression use, as here, it is used to determine if addition of a parameter is significant. In our context, the F-Test is used only to compare the fit of a

single spectrum to different models, not to compare different spectra. An F-ratio can be calculated to determine how much the addition of a parameter improves the fit [42]. The ratio is defined as follows[i]:

$$F_x = \frac{\chi^2(n-1) - \chi^2(n)}{\chi^2(n)/(2N-n)}$$

Eq 2-24

where F_x is the F-ratio, n is the number of parameters in the model, and $2N$ is the number of points in the experimental dataset.

If the fit is substantially better then χ^2 is smaller and the F-ratio is larger. The F-Test is a statistical test on whether or not the F-ratio could be that large by chance. The null hypothesis of this test is that an F-ratio this large could have arisen by chance.

The F-ratio is a statistic which follows the F distribution with $v_1 = 1$ and $v_2 = 2N - n$. The F-ratio can be used with an F-distribution table to determine a F values by looking up $F(2N - n, 1)$. This value can then be used to look up the probability of achieving the same fit or better by chance in F probability tables: $P_F(F, 1, 2N - n)$.

For example, if a function with k parameters and a function with k+1 parameters are being compared, the function with k+1 parameters should be accepted if $F_x(k+1) > F_x(k)$, and rejected if $F_x(k+1) << F_x(k)$. If $F_x(k+1) \approx F_x(k)$ then a judgment must be made as to whether the new model or old model better describes the system. If this likelihood (P_F) is small (typically <1%) the addition of the new parameter was reasonable, otherwise it was not statistically significant.

Maple's F-function was used to compare equivalent circuit models using the F-Test, because some F-tables do not cover the ranges of degrees of freedom required in our work, and because it avoided manual interpolation between table values.

---

[i] Eq 2-24 is adapted from the equation found in reference [42] because it is used for polynomial fitting with a constant term in their context but not in ours.

3 Data

The analysis rather than the experimental acquisition of fuel cell fault condition data was the purpose of this work, but a description of the experimental data used is necessary to understand its interpretation. All the data used in this work was acquired by Dr. Jean-Marc Le Canut for the Greenlight Power Systems. A further discussion of the experimental methods, conditions, and rationale for all the data used in this work can be found in the work of Mérida[1], and the Greenlight Power Systems reports by Le Canut *et al.*[2,3,4,5]

3.1 Summary of Experimental Setup

The experimental setup used to acquire the experimental impedance data used in this work consists of 3 primary components: the fuel cell test station, the fuel cell stack, and the EIS equipment. Below there is a brief overview of these components. A more in-depth description of the experimental setup is beyond the scope of this work but can be found in Refs.1 and 2.

3.1.1 Fuel Cell Test Station[1,2]

The fuel cell test station was manufactured by ASA Automation Systems (now Greenlight Power Technologies) for Ballard Power Systems. The test station provides conditioned fuel and oxidant streams to the fuel cell[2,43] with the possibility of the delivery of nitrogen to the cell. The pressure and flow of these gases are controlled through pressure regulators, rotameters, and flow meters. The station also delivers deionized water. The test station controls the cooling and heating of the cell through a control loop.

An attached humidification test station allows the control of the temperature and humidification of the reactant gases, independent for fuel and oxidant streams. A

manifolding systems allows for the independent delivery of dry or humidified gases to the fuel cell, or individual cells in the case of the fuel cell stack. The fuel cell test station allows for the monitoring of the cell voltage and gas temperatures through a DAQ (Data Acquisition System) and a Labview program.

The test station is kept in a fume hood, and there are hydrogen sensors and safeguards as well as a CO alarm in the room for safety reasons.

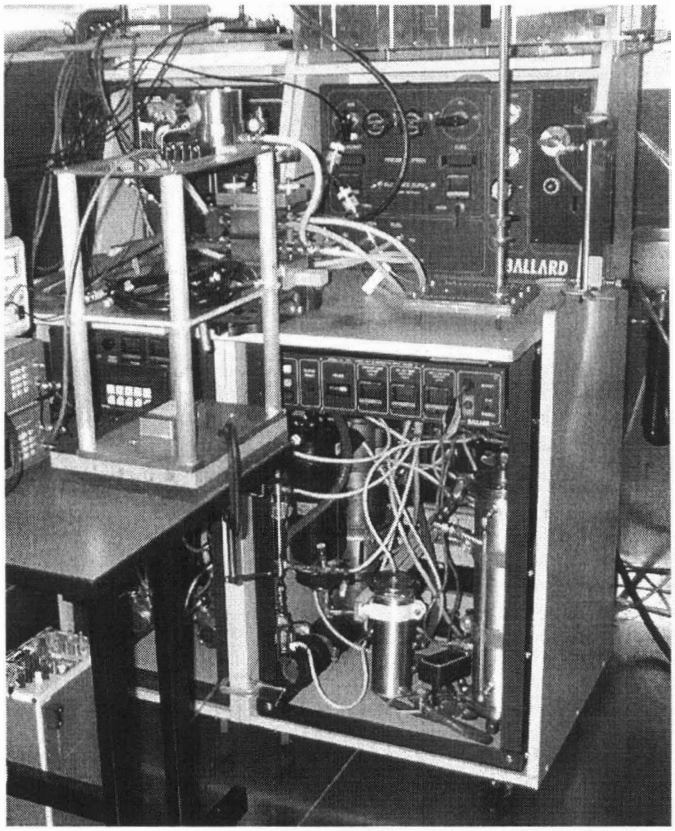

Figure 3.1: Fuel Cell Test Station.

3.1.2 Fuel Cell Stack

Two fuel cell stack test rigs were used to acquire the data used in this project. All the fault datasets (Sections 3.4-3.7) were acquired using the single cell test rig. The varied gas composition datasets (Section 3.8) were acquired using the four-cell stack test rig.

3.1.2.1 Single Cell Test Rig

The single cell test rig is made of a single cell: two graphite flow-field plates with an MEA between them, sealed with gaskets. This cell is placed between two current collectors, made of gold plated copper. The cell temperature is controlled through two stainless steel parts, sandwiching the current collectors, that allow for cooling/heating with deionized water. They also allow the passage of the fuel and oxidant gasses. This assembly is held together by two large aluminum plates, separated from the cell by insulating plates, connected to each other by threaded rods. Pressure can be applied to a stack by a sliding piston in the upper aluminum plate which uses pressurized nitrogen.

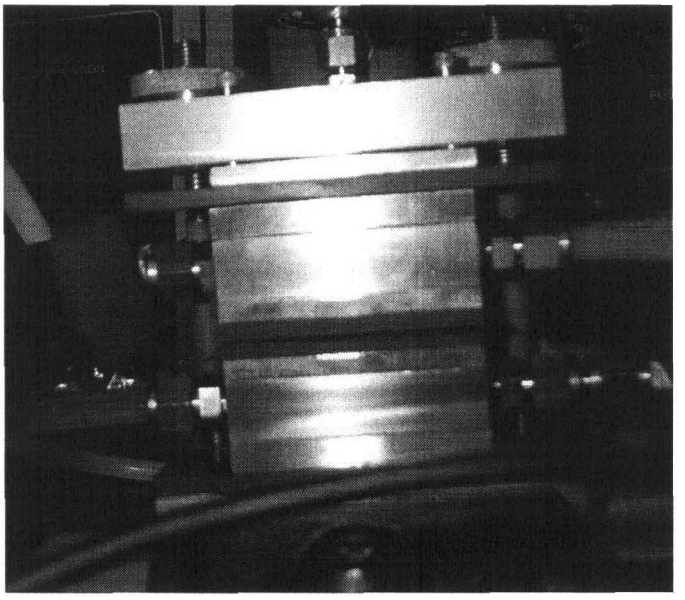

Figure 3.2: Single Cell Stack Assembly

3.1.2.2 Four Cell Test Rig

The four cell test rig is quite similar to the single cell test rig. The major differences are that there are four cells used instead of one, and that the fuel, oxidant, and cell cooling/heating water are controlled independently for each cell. In depth discussion regarding the design and function of the four cell stack can be found in Ref. 1.

3.1.3 EIS Equipment

Most of the EIS Measurements (Sections 3.4-3.6, and 3.8) were made with a Frequency Response Analyzer (FRA) Setup, but the Dual Fault dataset was acquired using a Lock-in Amplifier setup.

3.1.3.1 Frequency Response Analyzer (FRA) Setup

Most impedance data used in this work was acquired using the setup shown in (Figure 3.3).

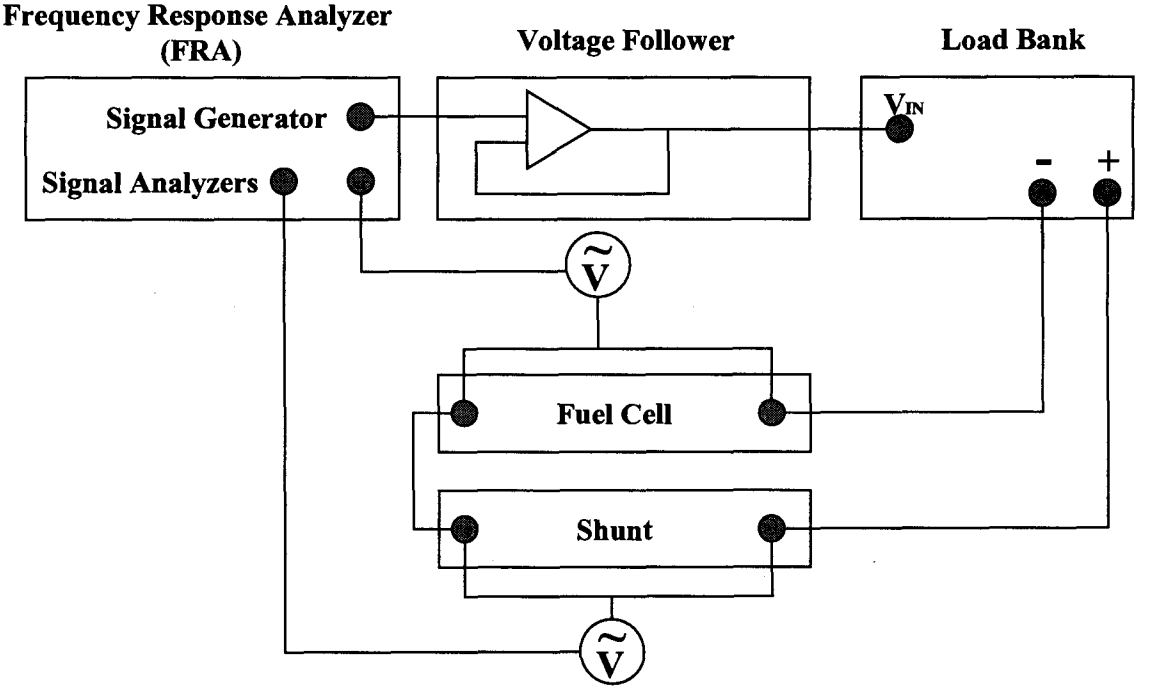

Figure 3.3: FRA Data Acquisition Setup.

The Load bank used was a Dynaload Load Bank which controls the DC current delivered to the stack and allow the superimposition of an AC perturbation (from the FRA).

The Frequency Response Analyzer used was a Solartron Analytical model (FRA 1255B). The instrument generates the AC sine wave imposed over the DC delivered to the stack. It also includes two independent input channels to monitor current and voltage. The input

channel measuring voltage is connected across the fuel cell and the input channel measuring current is connected across the shunt. Care was taken with the placement of the cabling.

The FRA is controlled though a computer using an IEEE488 interface board and a commercial software package: Zplot ™. Another software package, Zview ™, was used to view and analyze impedance data.

3.1.3.2 Lock-in Amplifier (LIA) Setup [5]

Two E.G.& G. Instruments 7265 DSP lock-in amplifiers (LIAs) were used for some impedance acquisition. The setup used is shown in Figure 3.4.

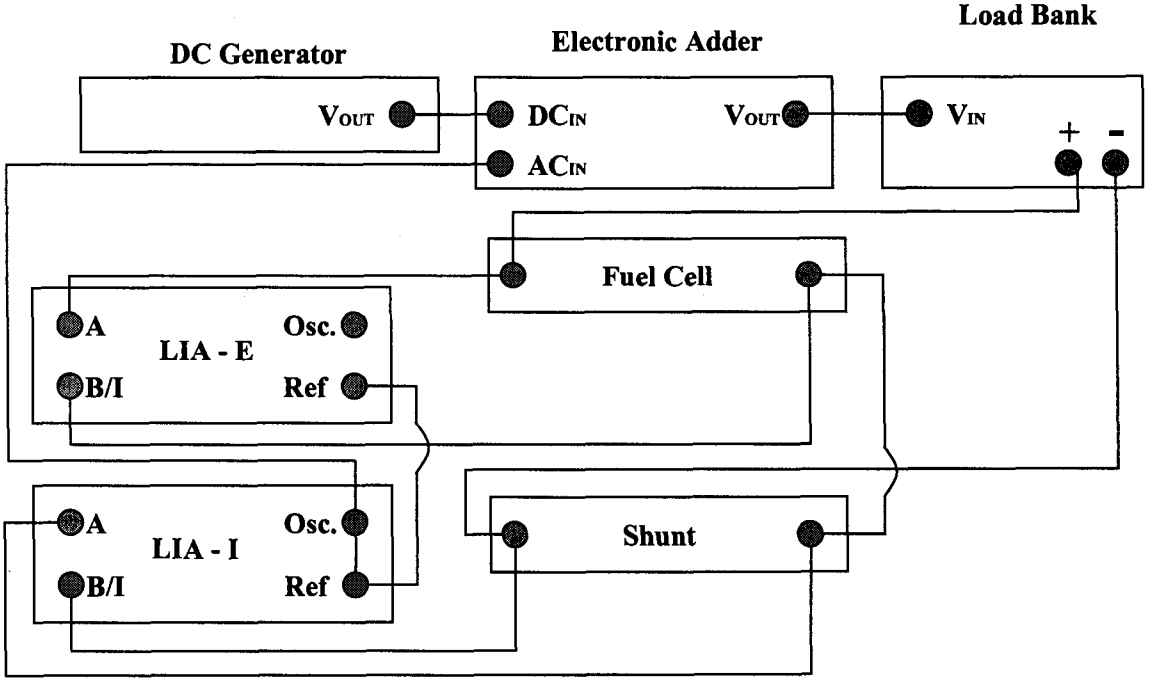

Figure 3.4: Lock-in Amplifier Impedance Acquisition Setup[44].

3.2 Definitions for Dataset Terms

The term spectrum will be used to describe a single set of impedance points measured at individual frequencies, acquired consecutively, in a single experiment.

The terms dataset and fault dataset are used throughout this work. The term dataset refers to a set of chronological spectra acquired on a given day with generally fixed conditions. In a given dataset everything but the condition being examined is held constant. A fault dataset refers specifically to a dataset where the condition being examined is a fault.

Normal operating conditions in the context of the work are the conditions prior to fault. In this context, the first impedance spectra acquired in a dataset is considered to represent the normal operating conditions for the set of conditions to which the fault was applied. This is also referred to as the baseline impedance spectrum.

Care was taken to ensure that full humidification was achieved before each experiment. Drying failure mode tests were exceptions because of the conditions required to achieve drying.

3.3 Typical Spectrum

A typical impedance spectrum for a fuel cell has three features shaped like semicircles. The first high frequency semi-circle, on the left in Figure 3.5, is where drying behaviour exhibits. The second mid frequency arc, is were CO poisoning and flooding behaviour exhibits; an increase in the real part for CO poisoning and an increase in the imaginary part for drying.

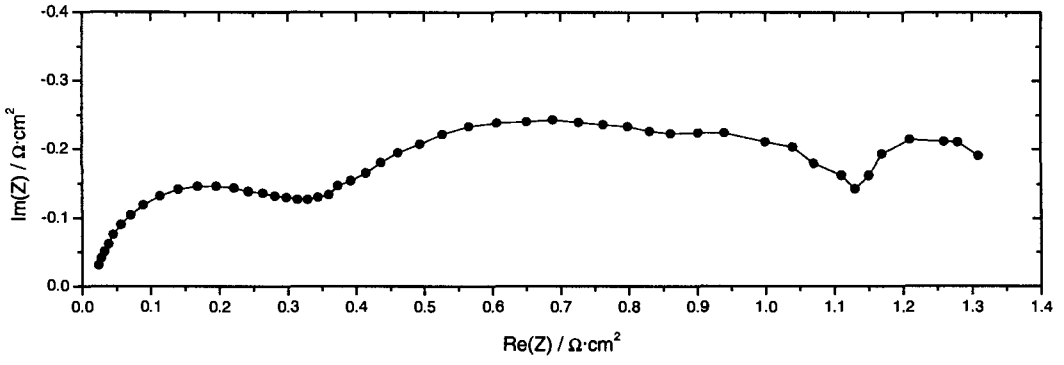

Figure 3.5: Typical fuel cell impedance spectra for pure H_2 and air, four cell stack data normalized to a single cell. : j=0.3 A·cm^{-2} (Conditions - Section 3.8.2).

3.4 Drying Datasets

Two Drying datasets were chosen as being representative for this work. Both were acquired with hydrogen as the fuel and air as the oxidant. Section 3.7 describes another dataset which includes a drying sequence using reformate as the fuel and air as the oxidant. Although both these drying datasets exhibit periodic drying and recovery behaviour, their EIS signature is the same as for non oscillating drying behaviour[1]. This oscillation is therefore not due to an artifact such as droplets blocking the inlet.

3.4.1 Drying 1 [3]

This drying dataset was acquired by maintaining the cell temperature higher than the gas temperature (Table 3-1). This caused the partial pressure of the water vapour to decrease and limited the humidification of the cell[3]. For this experiment impedance was recorded continuously, taking about 3 minutes per spectra, with spectra recorded one after another. The potential was recorded between acquisitions of spectra. Table 3-1 lists the experimental conditions for the Drying 1 experiment.

Table 3-1: Drying 1 Experimental Conditions

Fuel	Oxidant	j	MEA	MEA	anode Pt	cathode Pt	p_{fuel}	p_{ox}	T_{cell}	T_{fuel}	T_{ox}	Min f	Max f
		$A \cdot cm^{2}$	Man.	Material	$mgPt \cdot cm^{-2}$	$mgPt \cdot cm^{-2}$	psig	psig	°C	°C	°C	Hz	kHz
H_2	Air	0.4	MER	Nafion 115	0.5	1	30	30	80	70	70	0.5	250

Figure 3.6 shows the fluctuation of cell voltage with drying. The cell voltage decreases and partly recovers periodically. This is also reflected in the change in the size of the high frequency impedance arc, which gets larger as the voltage decreases (Figure 3.8). There is little change in the shape of the low frequency arcs with the exception of when the voltage changes abruptly during acquisition of an impedance spectra (t =12 min).

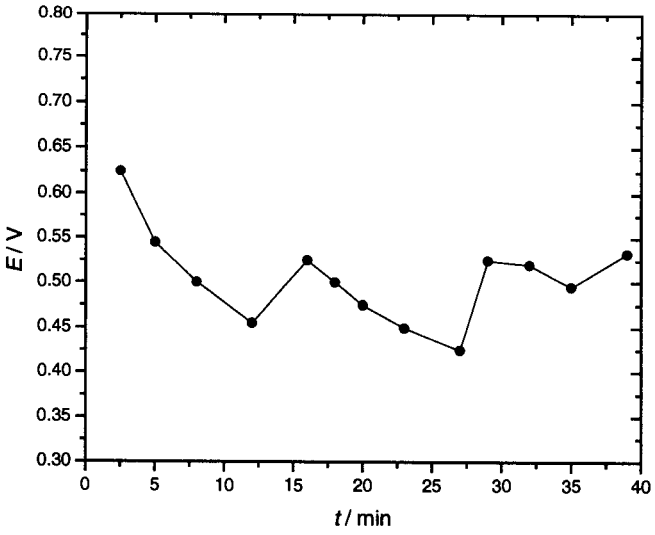

Figure 3.6: Drying 1 – Change in Cell Voltage with Time.

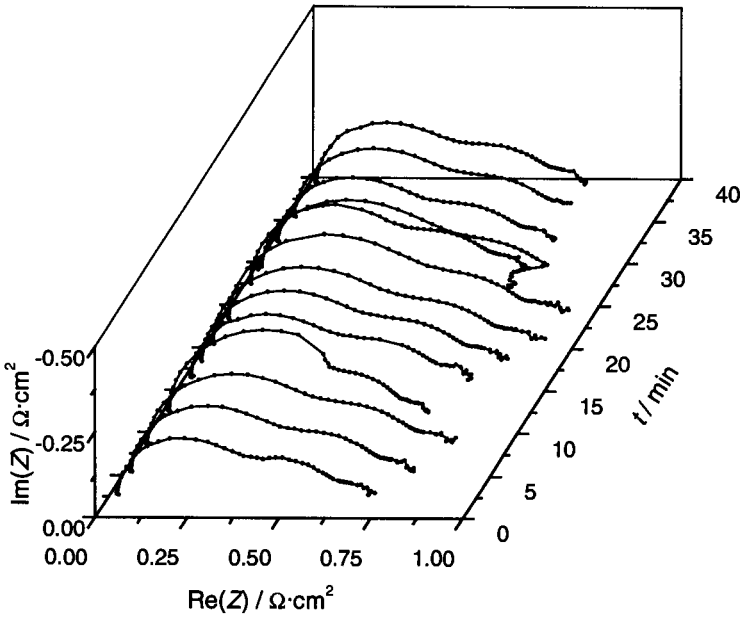

Figure 3.7: 3-D Nyquist for Drying 1 Dataset Impedance with Time.

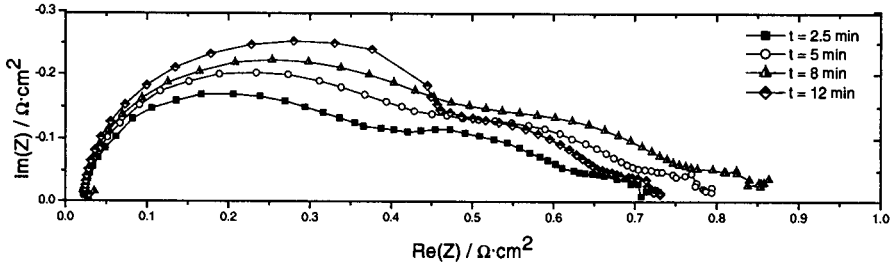

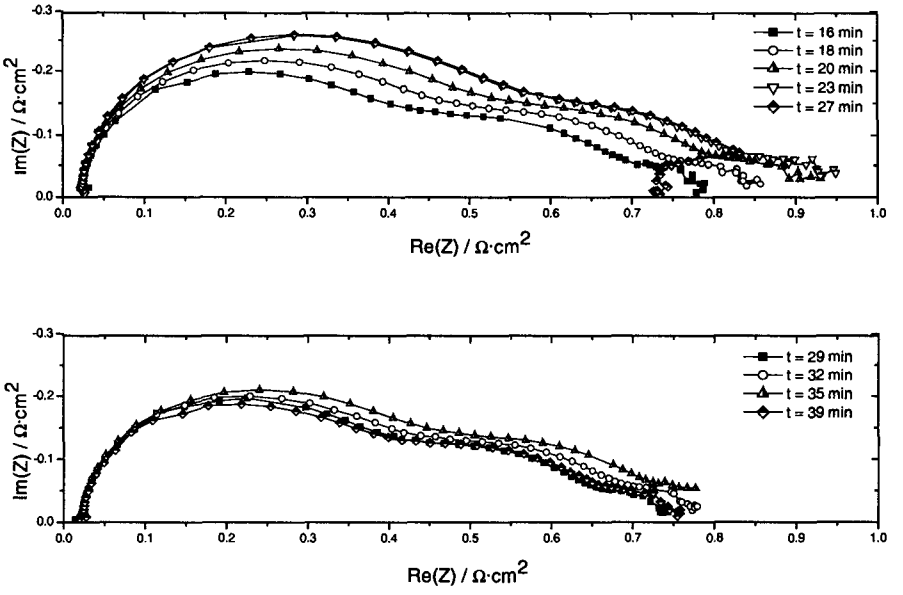

Figure 3.8: Change in Drying 1 Dataset Impedance with Time.

3.4.2 Drying 2 [3]

This drying dataset was acquired by maintaining the cell temperature (T_{cell} = 90°C) higher than the gas temperature (Table 3-2). For this experiment, impedance was recorded continuously, taking about 2.5 minutes per spectra, with spectra recorded one after another. The potential was recorded between the acquisition of spectra. The experimental conditions for the Drying 2 dataset are shown in Table 3-2.

Table 3-2: Drying 2 Experimental Conditions

Fuel	Oxidant	j	MEA	MEA	anode Pt	cathode Pt	p_{fuel}	p_{ox}	T_{cell}	T_{fuel}	T_{ox}	Min f	Max f
		$A \cdot cm^2$	Man.	Material	$mgPt \cdot cm^{-2}$	$mgPt \cdot cm^{-2}$	psig	psig	°C	°C	°C	Hz	kHz
H_2	Air	0.4	MER	Nafion 115	0.5	1	30	30	90	70	70	50	250

The frequency range for acquisition was reduced in order to focus on the high frequency impedance (where the effect of drying is most evident in the impedance). This also reduces acquisition time since lower frequency measurements take more time.

Figure 3.9 shows the fluctuation of cell voltage with drying. As in the Drying 1 dataset (Section 3.4.1), the cell voltage decreases and partly recovers periodically. This is also

reflected in the change in the size of the high frequency impedance arc, which gets larger as the voltage decreases due to drying.

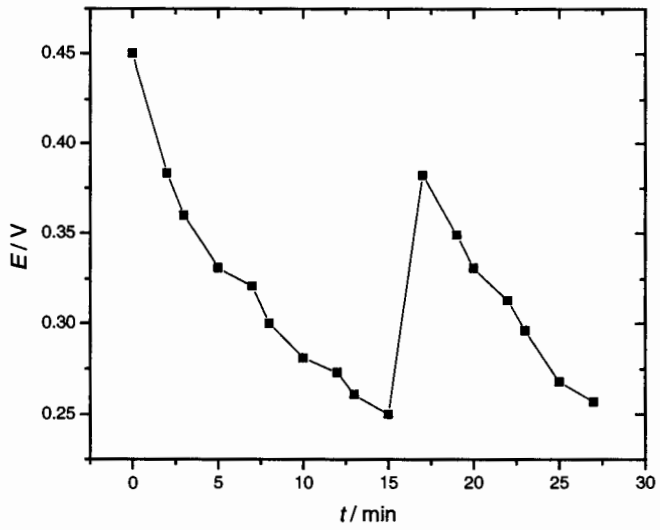

Figure 3.9: Drying 2 – Change in Cell Voltage with Time.

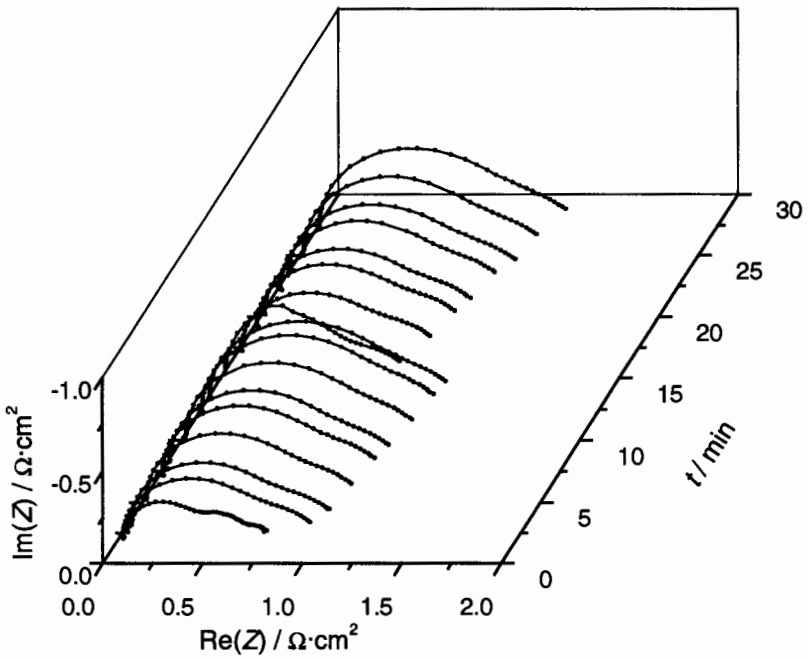

Figure 3.10: 3-D Nyquist Representation of Drying 2 Dataset.

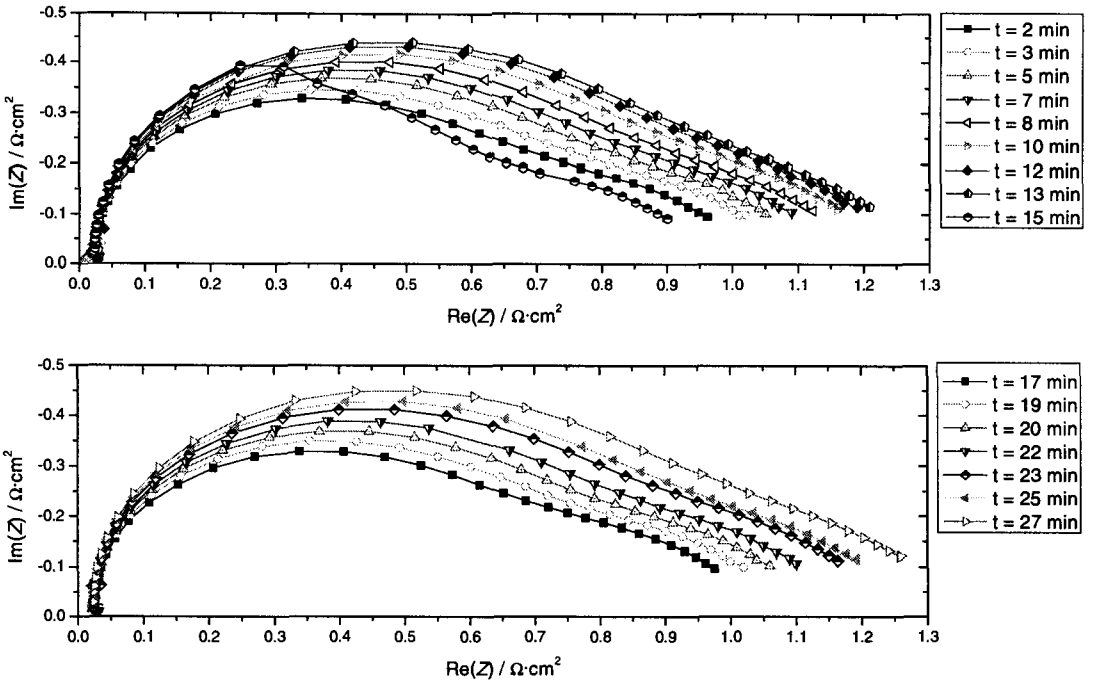

Figure 3.11: Change in Drying 1 Dataset Impedance with Time.

3.5 Flooding Dataset [3]

The flooding dataset is quite different from the other fault datasets. This is due primarily to the speed of flooding events and the relative difficulty of acquiring impedance spectra during a flooding event (as they are not always predictable). Because of this the "flooding dataset" is made up of the impedance spectra from various flooding events on different days under different conditions. They were not acquired chronologically so they are labeled with letters. Two different flooding acquisitions have been combined for this dataset: flooding set 1 and flooding set 2. Flooding set 1, which consist of flooding impedance spectra A-D (Figure 3.12 and Figure 3.14) was acquired under the conditions listed in Table 3-3. Flooding set 2, which consist of flooding impedance spectra E - I (Figure 3.13 and Figure 3.14) was acquired under the conditions listed in Table 3-4.

The impedance of flooding events is characterized by an increase in the size of the lower frequency (f<1 kHz) feature (Figure 3.12, Figure 3.13, and Figure 3.14). The high frequency semicircle does not seem to be affected by flooding.

Table 3-3: Experimental Conditions for Flooding Data Files A-D (Flooding Set 1).

Fuel	Oxidant	j	MEA	MEA	anode Pt	cathode Pt	p_{fuel}	p_{ox}	T_{cell}	T_{fuel}	T_{ox}	Min f	Max f
		$A \cdot cm^{-2}$	Man.	Material	$mgPt \cdot cm^{-2}$	$mgPt \cdot cm^{-2}$	psig	psig	°C	°C	°C	Hz	kHz
H_2	Air	0.5	MER	Nafion 115	0.5	1	30	30	35	90	95	1	150

Table 3-4: Experimental Conditions for Flooding Data Files D-I (Flooding Set 2).

Fuel	Oxidant	j	MEA	MEA	anode Pt	cathode Pt	p_{fuel}	p_{ox}	T_{cell}	T_{fuel}	T_{ox}	Min f	Max f
		$A \cdot cm^{-2}$	Man.	Material	$mgPt \cdot cm^{-2}$	$mgPt \cdot cm^{-2}$	psig	psig	°C	°C	°C	Hz	kHz
H_2	Air	varied	MER	Nafion 115	0.5	1	30	30	50	95	95	0.5	1000

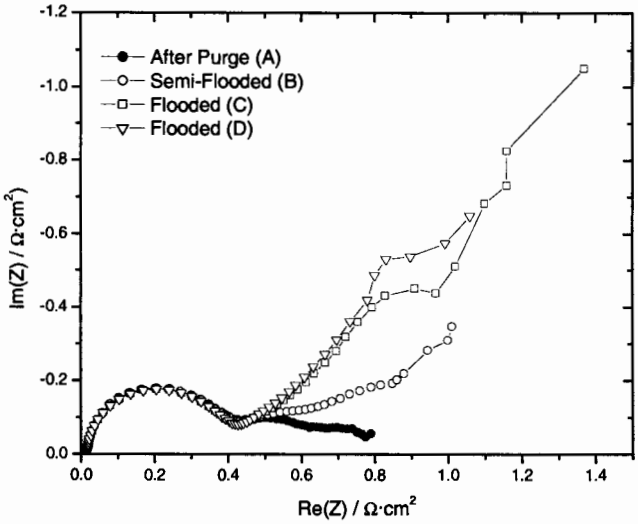

Figure 3.12: Change in Fuel Cell Impedance with Flooding Conditions (Flooding Set 1).

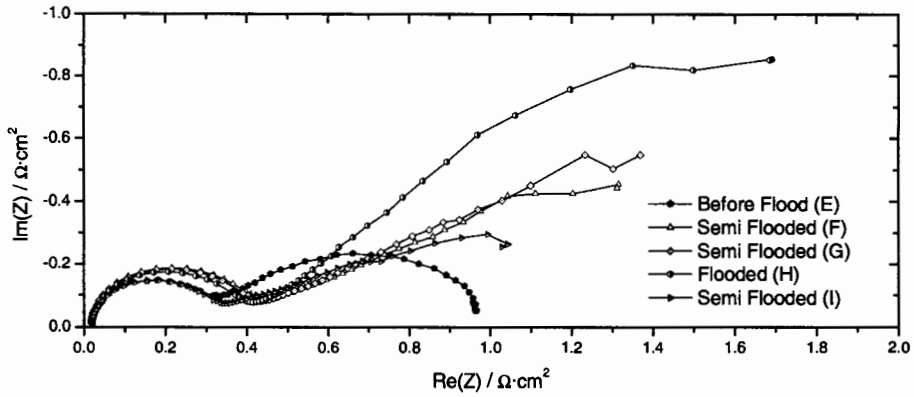

Figure 3.13: Change in Fuel Cell Impedance with Flooding Conditions (Flooding Set 2).

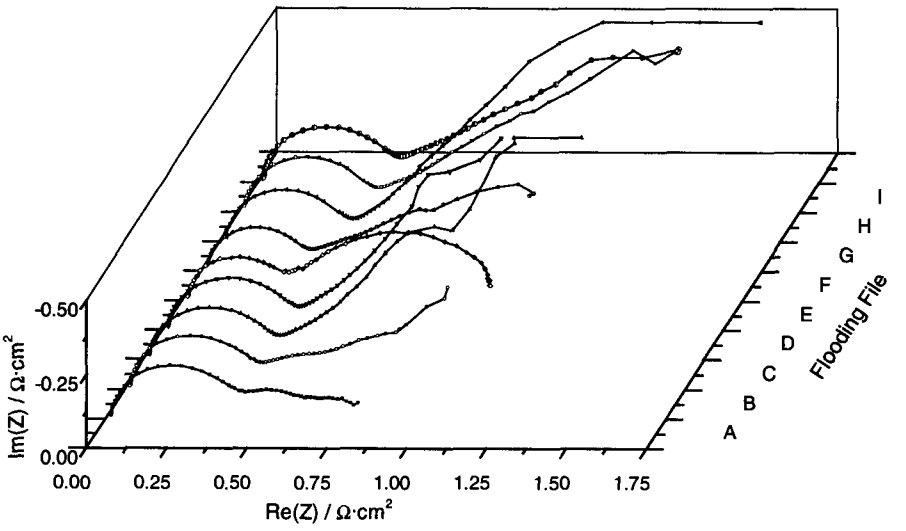

Figure 3.14: : 3-D Nyquist Representation of Flooding Impedance Data.

3.6 CO Poisoning Datasets[3]

The CO Poisoning dataset was acquired by replacing hydrogen with reformate with 10 ppm CO as the fuel gas. The composition of the reformate used is: 70% H_2, 24% CO_2 24%, and 6% N_2. While the fuel reformate (10ppm CO) was used as the fuel, the voltage decreased for approximately 80 minutes. The voltage decreased fairly slowly for the first hour and then more swiftly for another 20 minutes. At t = 80 min, approximately 1% air was bled into the fuel compartment and the cell voltage recovered rapidly over 5 minutes. Table 3-5 shows the experimental conditions for the CO poisoning experiment.

Table 3-5: CO Poisoning Experimental Conditions

Fuel	Oxidant	j	MEA	MEA	anode Pt	cathode Pt	p_{fuel}	p_{ox}	T_{cell}	T_{fuel}	T_{ox}	Min f	Max f
		$A \cdot cm^{-2}$	Man.	Material	$mgPt \cdot cm^{-2}$	$mgPt \cdot cm^{-2}$	psig	psig	°C	°C	°C	Hz	kHz
H_2	Ref	0.4	MER	Nafion 115	0.5	1	30	30	60	70	70	0.5	250

As CO poisoning progresses the second semicircle feature of the impedance gets larger while the first stays relatively the same.

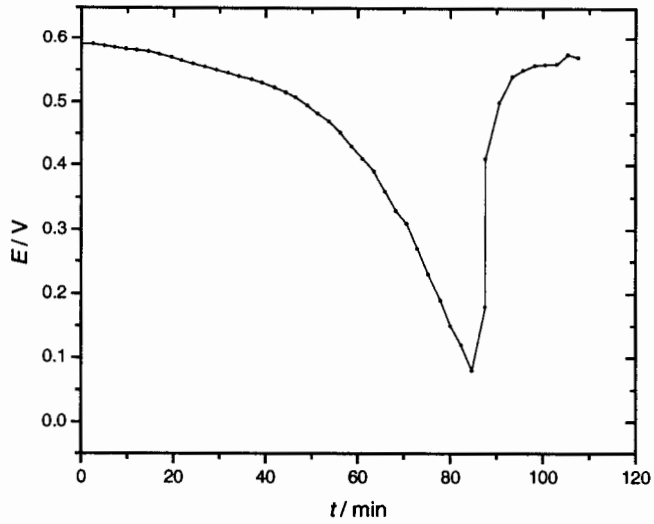

Figure 3.15: CO Poisoning – Change in Cell Voltage with Time.

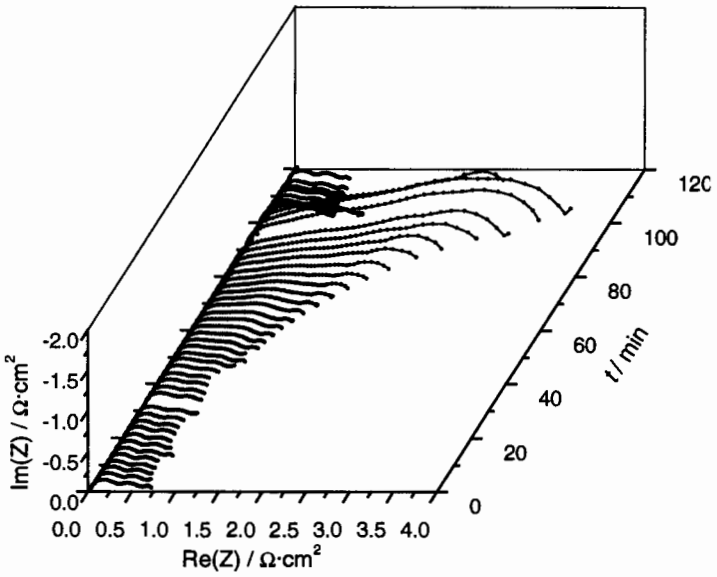

Figure 3.16: 3-D Nyquist Representation of CO Poisoning Dataset.

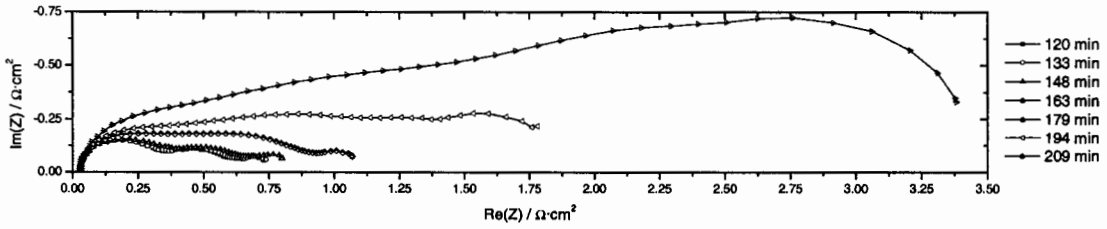

Figure 3.17: Change in CO Poisoning Dataset Impedance with Time (Selected Files) Before Recovery.

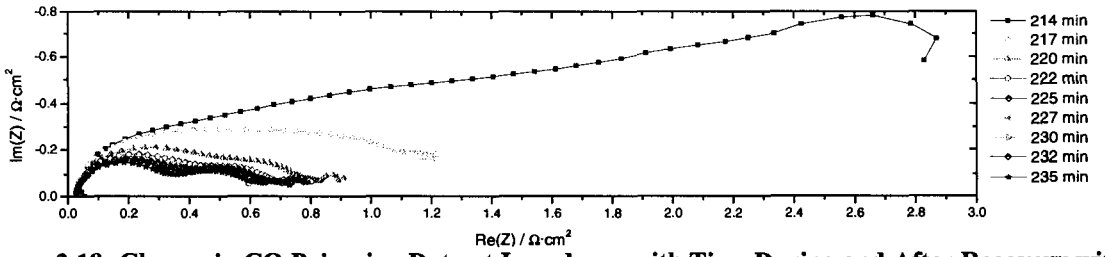

Figure 3.18: Change in CO Poisoning Dataset Impedance with Time During and After Recovery with Air Bleed.

3.7 Dual Fault Dataset[5]

For the dual fault dataset the fuel cell was poisoned with CO, recovered, then dried. The CO poisoning part of the dual fault dataset was acquired using the reformate with 10 ppm CO as the fuel. The composition of the reformate used is: 70% H_2, 24% CO_2 24%, and 6% N_2. At t = 80 min, approximately 1% air was bled into the fuel compartment and the cell voltage recovered rapidly over 10 minutes. The fuel cell membrane was then dried by switching the humidified fuel stream to a dry stream and by turning off the humidification to the air stream. Table 3-6 shows the experimental conditions for the dual fault dataset. Figure 3.19 and Figure 3.20 show the change in potential and impedance respectively with time for the dual fault dataset.

Table 3-6: Experimental Conditions for Dual Fault Dataset.

Fuel	Oxidant	j	MEA	MEA	anode Pt	cathode Pt	p_{fuel}	p_{ox}	T_{cell}	T_{fuel}	T_{ox}	Min f	Max f
		$A \cdot cm^{-2}$	Man.	Material	$mgPt \cdot cm^{-2}$	$mgPt \cdot cm^{-2}$	psig	psig	°C	°C	°C	Hz	kHz
Ref	Air	0.3	MER	Nafion 115	0.7	0.4	30	30	60	85	80	10	5

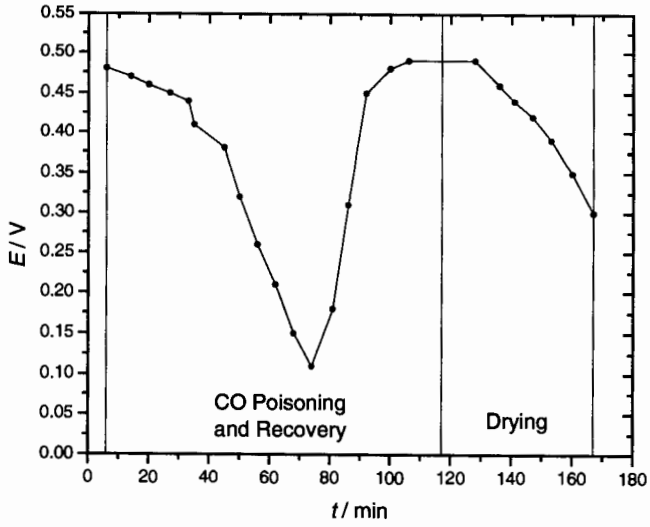

Figure 3.19: Dual Fault – Change in Cell Voltage with Time.

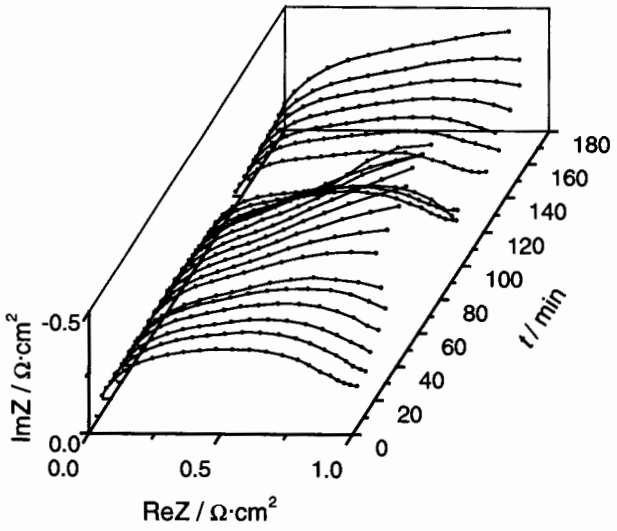

Figure 3.20: 3-D Nyquist Representation of Dual Fault Dataset.

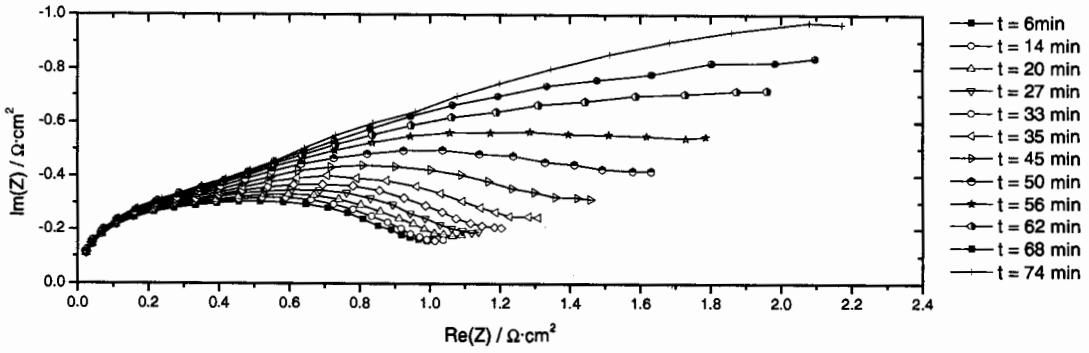

Figure 3.21: Change in Dual Fault Dataset Impedance with Time During CO Poisoning.

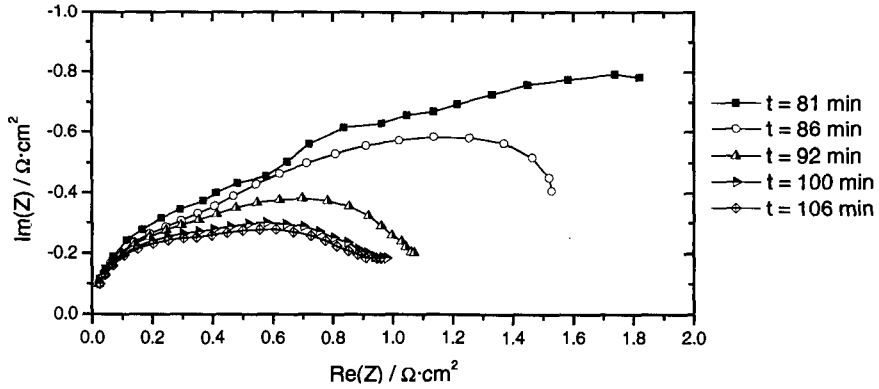

Figure 3.22: Change in Dual Fault Dataset Impedance with Time During CO Poisoning Recovery Due to Air Bleed.

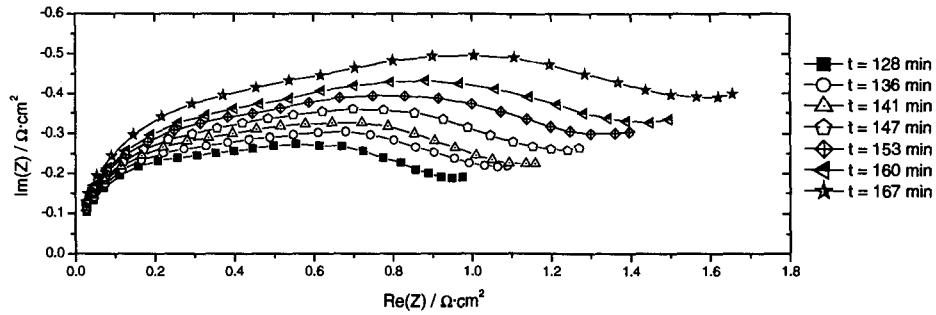

Figure 3.23: Change in Dual Fault Dataset Impedance with Time During Drying Sequence.

3.8 Varying Gas Composition Datasets

The varying gas composition datasets were acquired using different gas compositions for the fuel and oxidant streams and acquiring impedance spectra over a range of current densities. Five combinations of gas compositions were used: H_2-O_2, H_2-60% O_2, H_2-Air, Reformate –60% O_2, and Reformate-Air. All were acquired on the four cell stack assembly, with the impedance of each cell measured. For data analysis purposes, only the data from Cell 1 was used.

3.8.1 Pure Hydrogen and Oxygen (H_2-O_2)[4]

The conditions, polarization curves, and impedance diagrams for the H_2-O_2 experiment are shown in Table 3-7, Figure 3.24, and Figure 3.25 respectively.

Table 3-7: Experimental Conditions for H_2-O_2 Gas Composition Dataset.

Fuel	Oxidant	MEA	MEA	anode Pt	cathode Pt	p_{fuel}	p_{ox}	T_{cell}	T_{fuel}	T_{ox}	Min f	Max f
		Man.	Material	mgPt·cm^2	mgPt·cm^2	psig	psig	°C	°C	°C	Hz	kHz
H_2	O_2	MER	Nafion 115	0.7	0.4	30	30	65	85	70	0.5	50

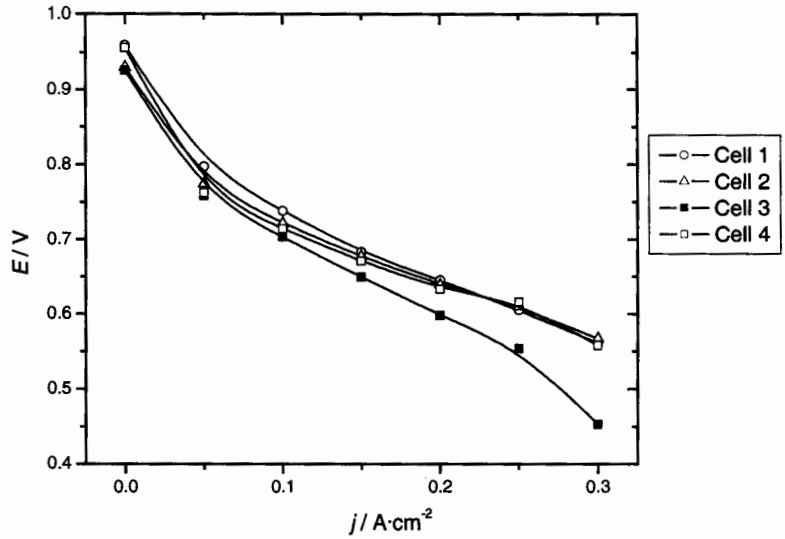

Figure 3.24: Polarization Curves for H_2-O_2 Gas Composition Dataset.

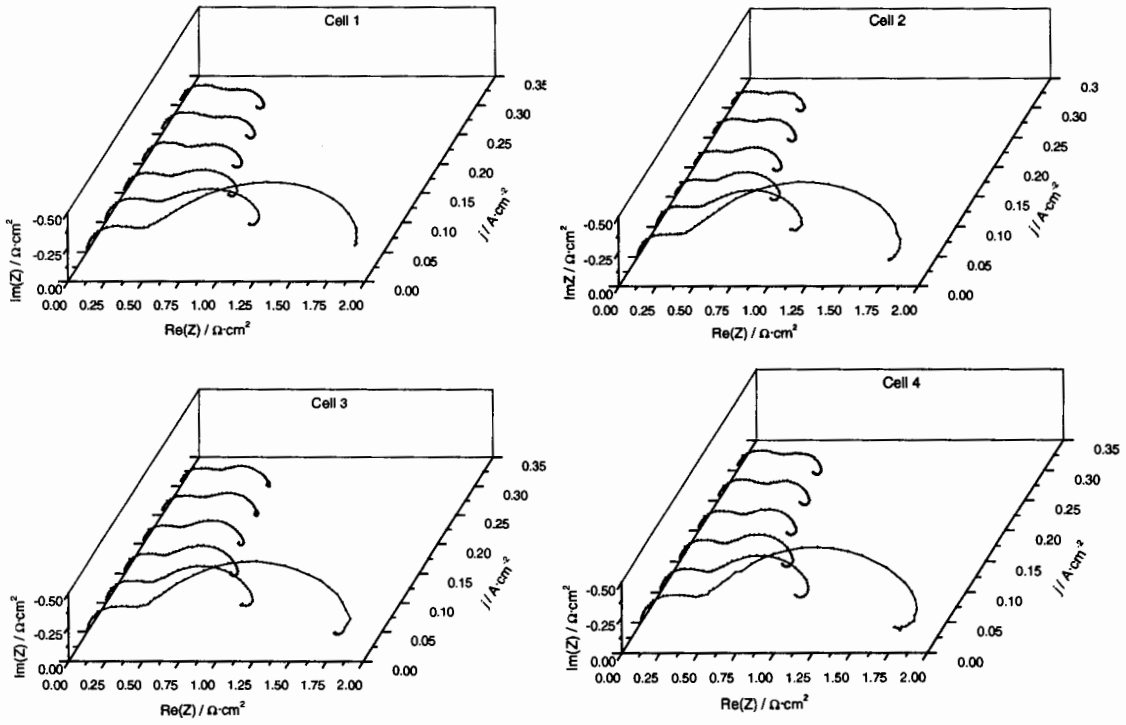

Figure 3.25: 3-D Nyquist Representations of H_2-O_2 Impedance Data.

3.8.2 Pure Hydrogen and Air (H_2-Air)[4]

The conditions, polarization curves, and impedance diagrams for the H_2-Air experiment are shown in Table 3-8, Figure 3.26, and Figure 3.27 respectively.

Table 3-8: Experimental Conditions for H_2-Air Gas Composition Dataset.

Fuel	Oxidant	MEA	MEA	anode Pt	cathode Pt	p_{fuel}	p_{ox}	T_{cell}	T_{fuel}	T_{ox}	Min f	Max f
		Man.	Material	mgPt·cm^{-2}	mgPt·cm^{-2}	psig	psig	°C	°C	°C	Hz	kHz
H_2	Air	MER	Nafion 115	0.7	0.4	30	30	65	85	70	0.5	50

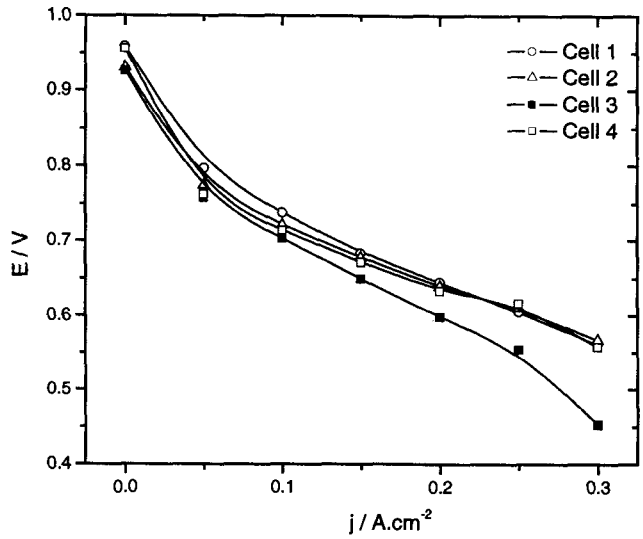

Figure 3.26: Polarization Curves for H_2-Air Gas Composition Dataset.

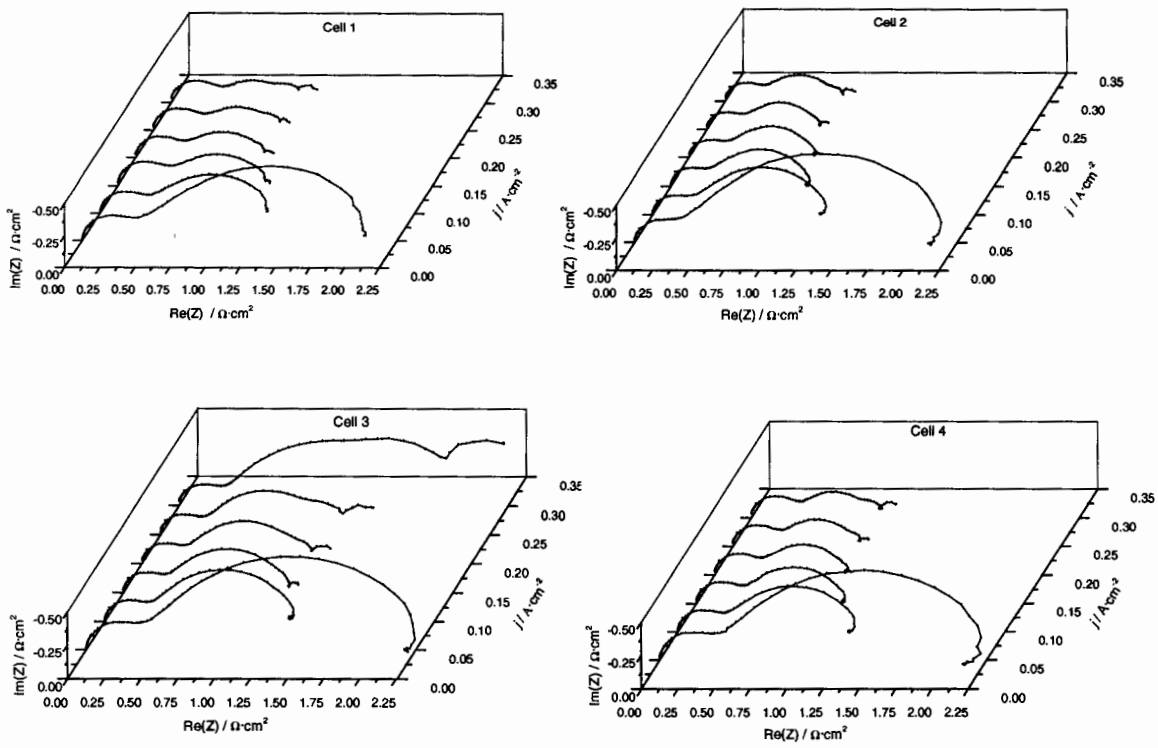

Figure 3.27: 3-D Nyquist Representations of H_2-Air Impedance Data.

3.8.3 Pure Hydrogen and 60% Oxygen, 40 % Nitrogen (H_2-$O_2$60%)[4]

The conditions, polarization curves, and impedance diagrams for the H_2-60% O_2 experiment are shown in Table 3-8, Figure 3.26, and Figure 3.27 respectively.

Table 3-9: Experimental Conditions for H_2- 60% O_2 Gas Composition Dataset.

Fuel	Oxidant	MEA	MEA	anode Pt	cathode Pt	p_{fuel}	p_{ox}	T_{cell}	T_{fuel}	T_{ox}	Min f	Max f
		Man.	Material	mgPt·cm^{-2}	mgPt·cm^{-2}	psig	psig	°C	°C	°C	Hz	kHz
H_2	60% O_2 40% N_2	MER	Nafion 115	0.7	0.4	30	30	65	85	70	0.5	50

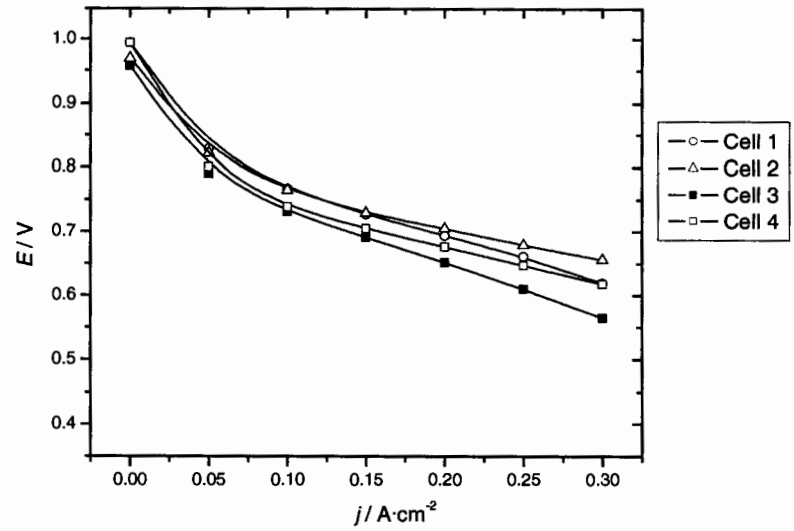

Figure 3.28: Polarization Curves for H_2- 60% O_2 Gas Composition Dataset.

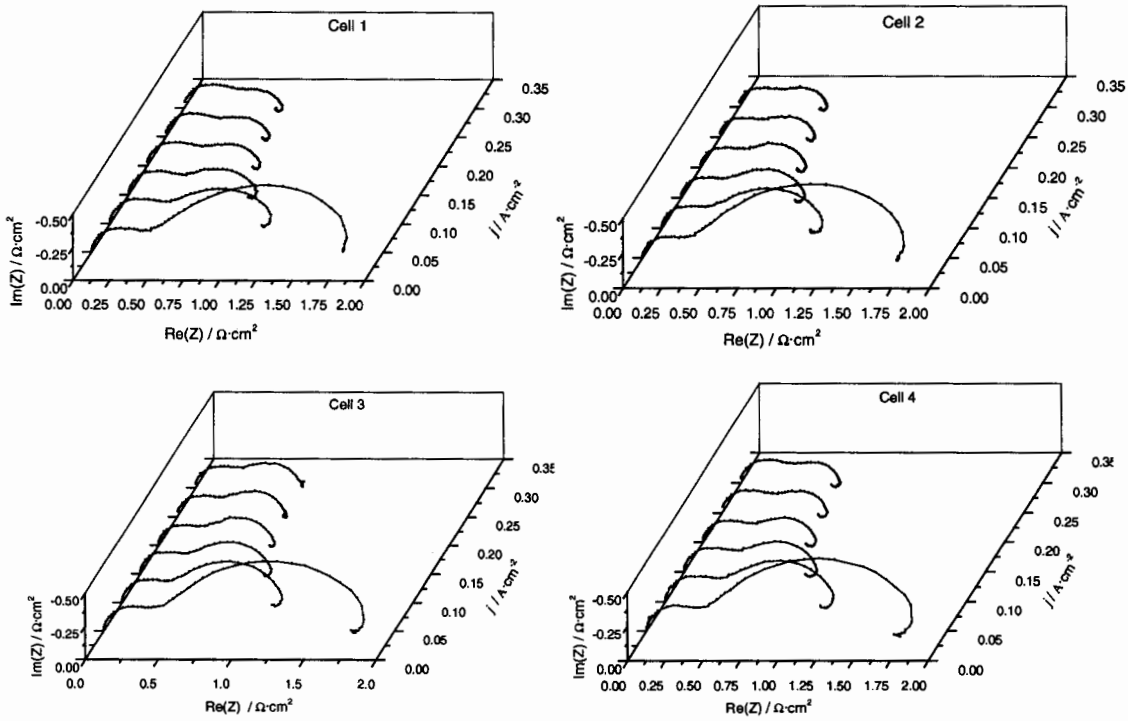

Figure 3.29: 3-D Nyquist Representations of H_2-60% O_2 Impedance Data.

3.8.4 Reformate and 60% Oxygen, 40 % Nitrogen (Ref-$O_2$60%)[4]

The reformate used for this experiment was a mixture of the following composition: 70% H_2, 24% CO_2 24%, and 6% N_2. The conditions, polarization curves, and impedance diagrams for the Ref –60% O_2 experiment are shown in Table 3-10, Figure 3.30, and Figure 3.31 respectively.

Table 3-10: Experimental Conditions for Ref - 60% O_2 Gas Composition Dataset.

Fuel	Oxidant	MEA	MEA	anode Pt	cathode Pt	p_{fuel}	p_{ox}	T_{cell}	T_{fuel}	T_{ox}	Min f	Max f
		Man.	Material	mgPt·cm^{-2}	mgPt·cm^{-2}	psig	psig	°C	°C	°C	Hz	kHz
Ref	60% O_2 40% N_2	MER	Nafion 115	0.7	0.4	30	30	65	85	70	0.5	50

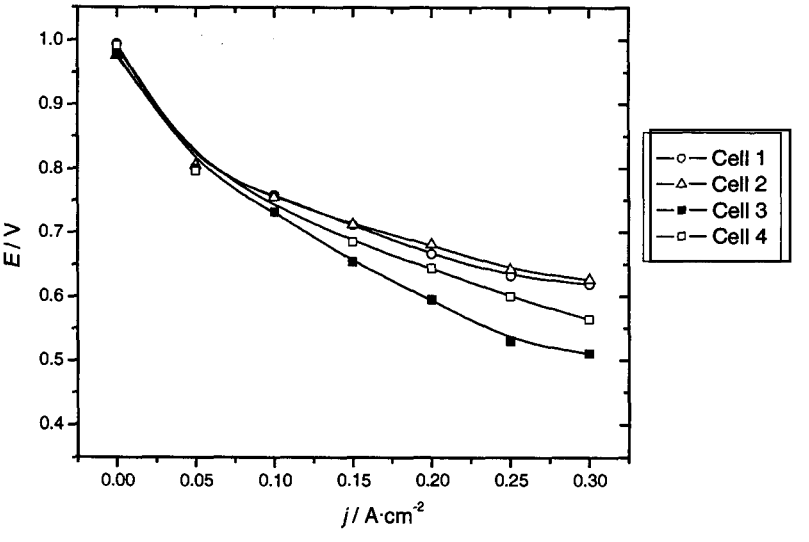

Figure 3.30: Polarization Curves for Ref- 60% O_2 Gas Composition Dataset.

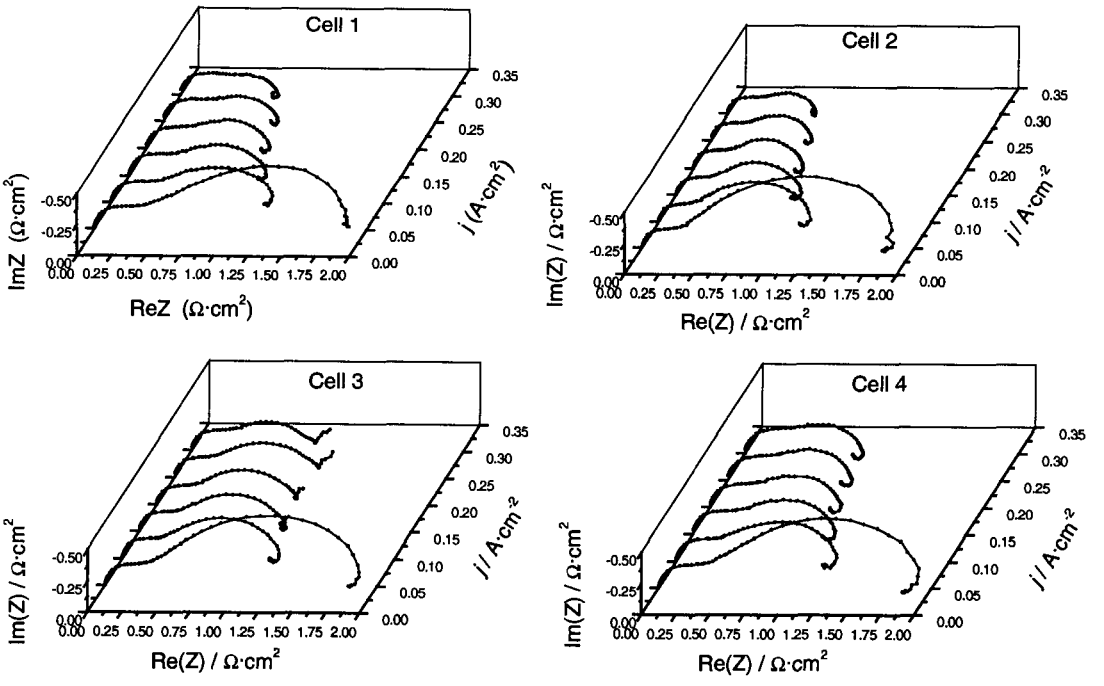

Figure 3.31: 3-D Nyquist Representations of Ref-60% O_2 Impedance Data.

3.8.5 Reformate and Air (Ref-Air)[4]

The reformate used for this experiment was a mixture of the following composition: 70% H_2, 24% CO_2 24%, and 6% N_2. The conditions, polarization curves, and impedance diagrams for the Ref-Air experiment are shown in Table 3-11, Figure 3.32, and Figure 3.33 respectively.

Table 3-11: Experimental Conditions for Ref –Air Gas Composition Dataset.

Fuel	Oxidant	MEA	MEA	anode Pt	cathode Pt	p_{fuel}	p_{ox}	T_{cell}	T_{fuel}	T_{ox}	Min f	Max f
		Man.	Material	mgPt·cm^{-2}	mgPt·cm^{-2}	psig	psig	°C	°C	°C	Hz	kHz
Ref	Air	MER	Nafion 115	0.7	0.4	30	30	65	85	70	0.5	50

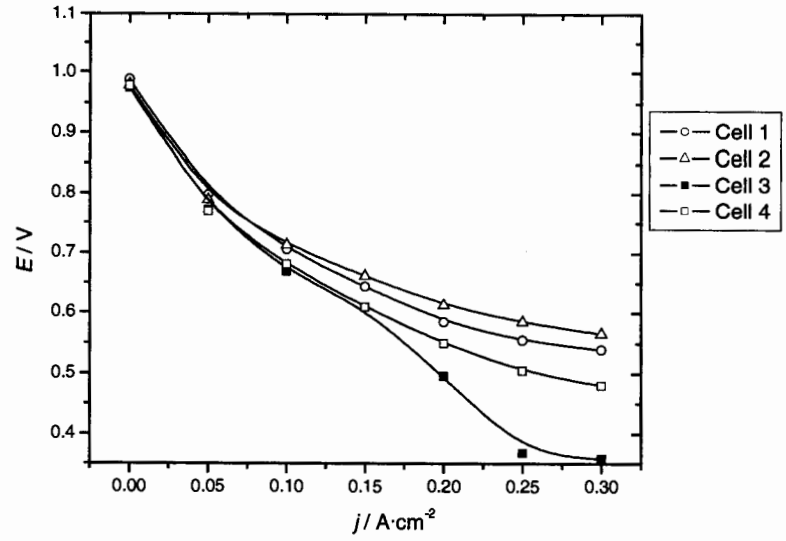

Figure 3.32: Polarization Curves for Ref- Air Gas Composition Dataset.

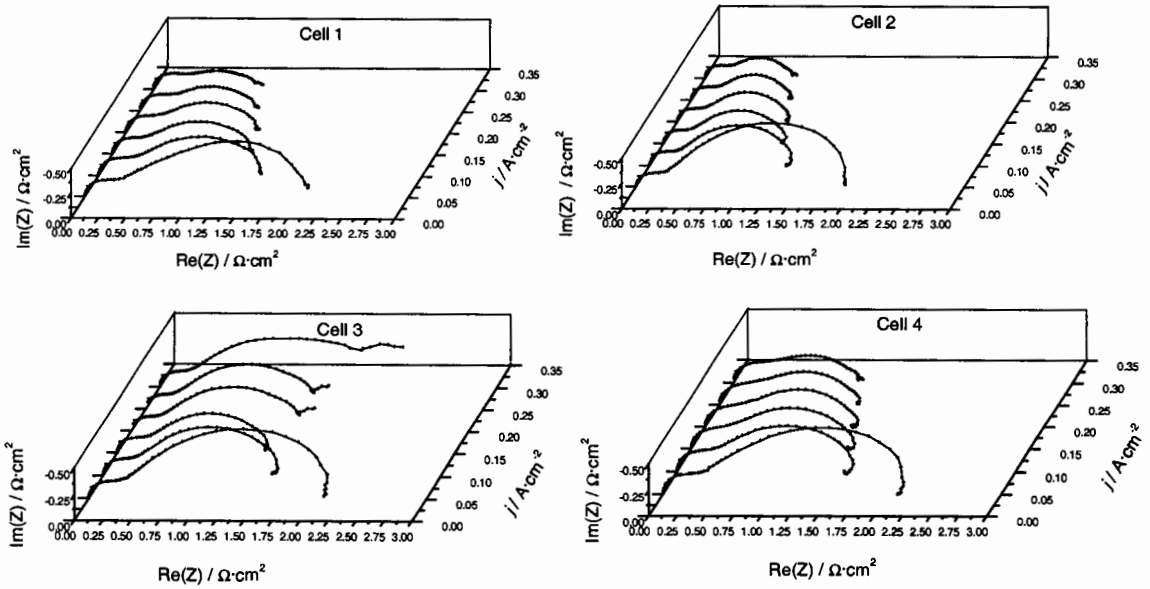

Figure 3.33: 3-D Nyquist Representations of Ref-Air Impedance Data.

4 Equivalent Circuit Model Development

Equivalent circuit fitting has the ability to be quite useful as a fuel cell diagnostic algorithm, particularly in an off-board setting. Through the possible relationship between equivalent circuit element values and physical characteristics of the fuel cell, there is the potential to identify not just fault conditions but also the part of the fuel cell affected. Equivalent circuit fitting would be less useful in an onboard diagnostic device because of the sensitivity to initial conditions (sufficiently so that one set of initial conditions would not necessarily be useable for all operating conditions) and the time required to achieve convergence.

As an initial basis for this work, fuel cell models from the literature were surveyed. These models were examined, modified, and compared in an attempt to develop a model with good fitting properties and logical physical significance. Models from the literature and in-house models were used as the basis for modification through subtraction methods and trial and error. All models were compared using the χ^2 test for models with an equal number of parameters and the F-test for models with different numbers of parameters.

4.1 Early In-House Models

Initial studies were performed using the model developed by Dr. Jean-Marc Le Canut in earlier work on this project.[44] This circuit (Figure 4.1) was used to model the PEMFC impedance assuming that the impedance at the anode is small compared to the cathode and membrane impedances. In Figure 4.1 the membrane resistance contributes to both R_Ω, and R_m, C_m is a capacitance associated with the membrane (likely the geometric capacitance), and W_c is a Warburg parameter related to diffusion at the cathode:

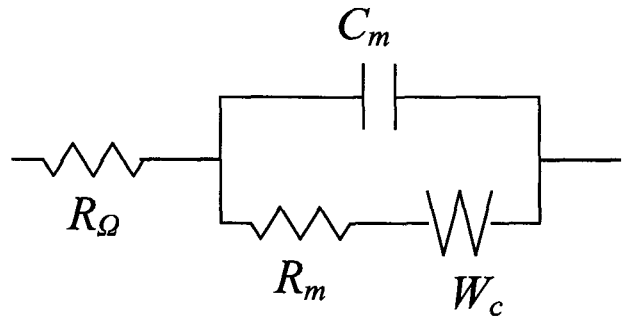

Figure 4.1: Early In-House Circuit 1[44].

This circuit was later used again as part of another model (Figure 4.2) where the anode contribution is considered but diffusion is considered to be very fast at the anode while the resistance is ignored at the cathode. In this model C_{dl} is the double layer capacitance.

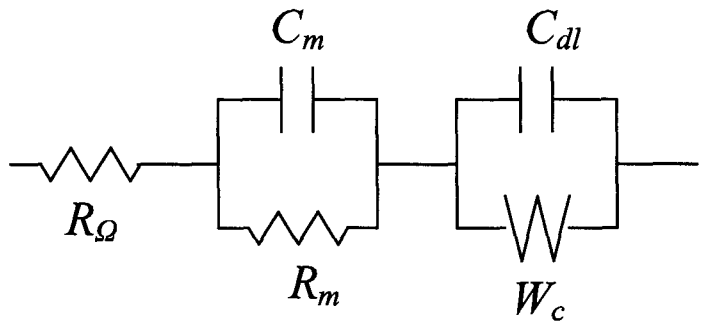

Figure 4.2: Early In-House Circuit 2[44].

4.2 Models from the Literature

Many equivalent circuit models can be found in the literature to describe the impedance of fuel cells. Elements of these models were used in an attempt to fit our results but none were more successful than later in-house models. Though PEM fuel cell impedance models were the primary focus for the modeling in this work, models for solid oxide and direct methanol fuel cell impedance were also investigated.

4.2.1 PEM Fuel Cells

The PEM fuel cell models in the literature fall into two primary categories: entire fuel cell models and membrane specific models.

4.2.1.1 Entire Fuel Cell Models

Several groups have developed models for the impedance of operating PEM fuel cells.

4.2.1.1.1 Schiller et al.[45,46] *and Wagner* et al.[47,48] *Models*

Schiller *et al.* [45,46] and Wagner *et al.* [47] propose the model in Figure 4.3 to describe the impedance of fuel cells during normal operating conditions [46] and during CO poisoning [45,47]. In this model L_w is an inductance attributed to wiring, R_Ω is the membrane resistance, $CPE_{dl\text{-}c}$, and $CPE_{dl\text{-}a}$ are approximations of the double-layer capacity at the cathode and the anode respectively, $R_{ct\text{-}c}$, and $R_{ct\text{-}a}$ are charge transfer resistances associated with the cathode and the anode reactions respectively, and Z_c is the finite diffusion impedance. The Nernst impedance (Z_N) is used to define the finite diffusion impedance [47] (Eq 4-1). Here R_W is the Warburg R parameter, D_k is the diffusion constant (for diffusion of species k to the anode), and d_N is the diffusion layer thickness:

$$Z_N = \frac{R_w}{\sqrt{i \cdot \omega}} \cdot \tanh \sqrt{\frac{i \cdot \omega}{D_k \cdot (d_N)^{-2}}}$$

Eq 4-1

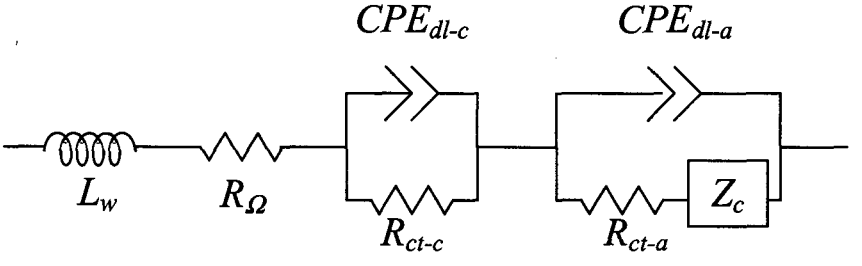

Figure 4.3: Model Proposed by Schiller *et al.* [45,46] and Later by Wagner *et al.* [47] to Describe the Impedance of Fuel Cells During CO Poisoning, and During "normal" Operation.

Another model was later proposed by Wagner *et al.* [48] (Figure 4.4) which is similar to the model in Figure 4.3. All the elements have the same interpretation, with the exception of the removal of the wiring inductance element (L_w) and the addition, on the anode circuit branch, of a parallel "relaxation impedance" characterized by a series relaxation resistance (R_K) and pseudo-inductance (L_K) which is defined in Eq 4-2 where τ_K is the relaxation time constant.

$$L_K = \tau_K \cdot R_K$$

Eq 4-2

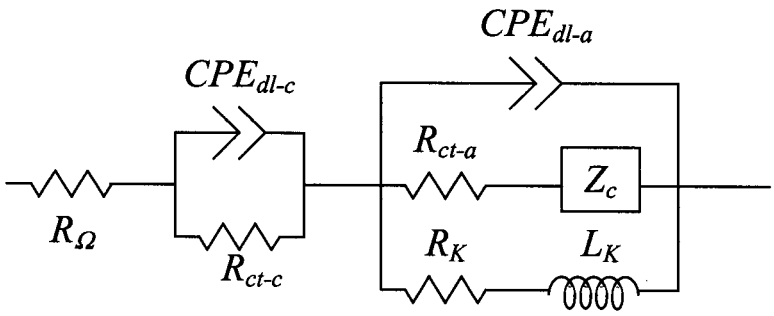

Figure 4.4: Model Proposed by Wagner *et al.* [48] to Describe Fuel Cell Impedance During CO Poisoning.

4.2.1.1.2 Andreaus et al. *Models*[49,50]

Andreaus *et al.* have proposed both an idealized model for the only the fuel cell cathode[50] (Figure 4.5) as well as for the entire fuel cell[49] (Figure 4.6).

In Figure 4.5 R_Ω is the membrane resistance, C_{dl-c} is the double layer capacitance associated with the cathode, R_{ct-c} is the charge transfer resistance associated with the cathode reaction, and W_c is the Warburg impedance associated with the diffusion of oxidant to the cathode.

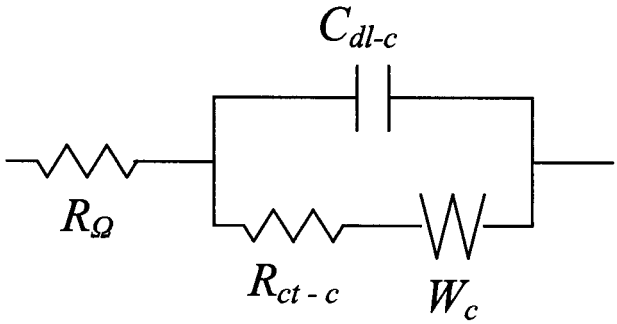

Figure 4.5: Model Proposed by Andreaus *et al.* [50] to Describe the Cathode Impedance of Fuel Cells.

In Figure 4.6 R_Ω is the membrane resistance, C_{dl} is the double layer capacitance of the entire cell, R_{ct} is the charge transfer resistance associated with the entire reaction, and Z_N is the Nernst impedance.

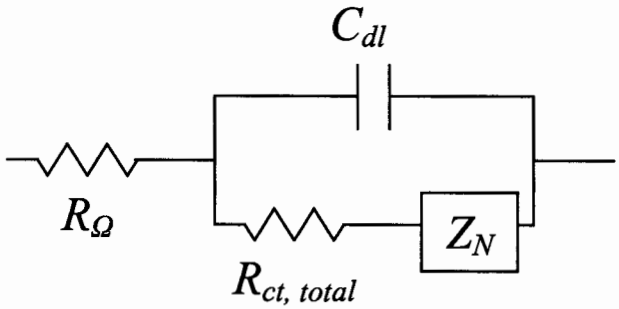

Figure 4.6: Model Proposed by Andreaus *et al.*[49] to Ideally Describe the Impedance of Fuel Cells.

4.2.1.1.3 Ciureanu et al. *Models*[51,52,53]

Ciureanu *et al.* [51,52,53] propose several models to describe the behaviour of fuel cells, with a particular interest in the behaviour of the anode. They initially proposed a circuit (Figure 4.7) to describe the anode and membrane impedance using an H_2/H_2 fed cell. In the first paper[51] the physical meaning of the parameters is addressed: R_Ω is the membrane resistance, C_1 is the double layer capacitance, and R_1 is the charge transfer resistance, and C_2 and R_2 are described as the "capacitance and resistance of an adsorbed species". The other papers[52,53] do not discuss the physical significance of parameters.

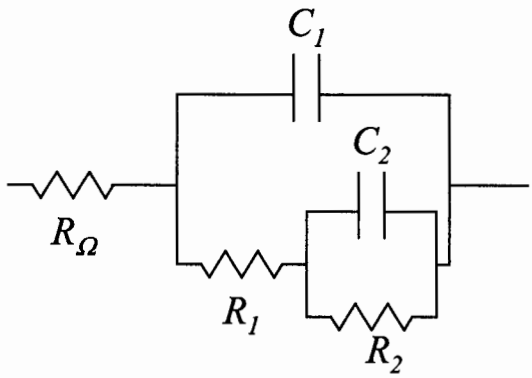

Figure 4.7: Model Proposed by Ciureanu *et al.* [51,52,53] for the Impedance of an H_2/H_2 fed Fuel Cell.

They also proposed a circuit (Figure 4.8) to describe the anode and membrane impedance using an H_2/H_2+CO fed cell to model the effect of CO poisoning. For this circuit R_Ω, R_1,

R_1, are attributed the same physical significance as those in Figure 4.7, while CPE_1 and CPE_2 are associated with the same processes as C_1 and C_2 respectively.

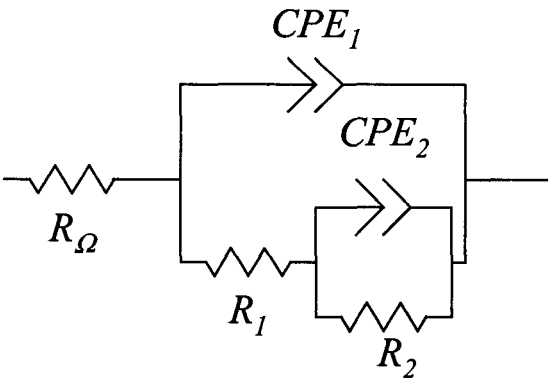

Figure 4.8: Model Proposed by Ciureanu *et al.* [51,52,53] for the Impedance of an H_2/H_2+CO fed Fuel Cell.

Another model (Figure 4.9) is proposed in the first two papers[51,52] but is omitted from the third paper[53] to describe the anode and membrane impedance using an H_2/H_2+CO fed cell to model the effect of CO poisoning. In this model all the circuit parameters are attributed the same physical significance as those with the same name in Figure 4.7 with the exception of C_3 and R_3 which are associated with the process of oxidative removal of CO.

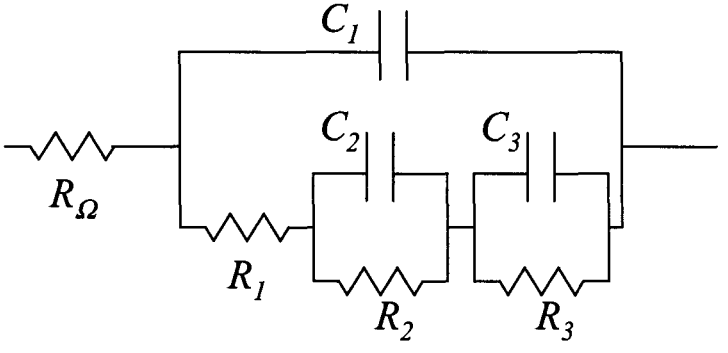

Figure 4.9: Early Model Proposed by Ciureanu *et al.* [51,52] for the Impedance of an H_2/H_2+CO fed Fuel Cell.

Another model (Figure 4.10) is proposed in the most recent paper[53] to describe the "typical complex impedance response of a humidified PEM". In this model the physical significance of circuit elements are described as follows: R_1 is the bulk resistance of the

specimen, C_1 is the cell capacitance, and W is related to the diffusion of protons within the membrane.

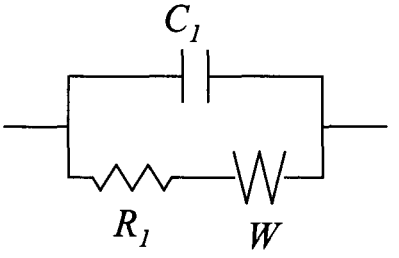

Figure 4.10: Model Proposed by Ciureanu *et al.* [53] for the Impedance of an H_2/O_2 fed Fuel Cell.

4.2.1.2 Membrane Specific Models

There have been many groups who have studied and modeled the impedance of just the MEA or the electrolyte. These studies differ from our work in that the MEA or electrolyte is studied outside of a working fuel cell application.

4.2.1.2.1 Beattie et al. *Model*[54]

Beattie *et al.* [54] have studied the impedance of humidified BAM membranes in direct contact with a gold electrode. They proposed the model in Figure 4.11 to describe the impedance response for interface between the gold electrode and the electrolyte. In Figure 4.11 R_m and C_m are the membrane resistance and capacitance, respectively, R_c is the contact resistance, C_{dl} is the double-layer capacitance, R_{ct} is the charge transfer resistance, and W is the Warburg impedance.

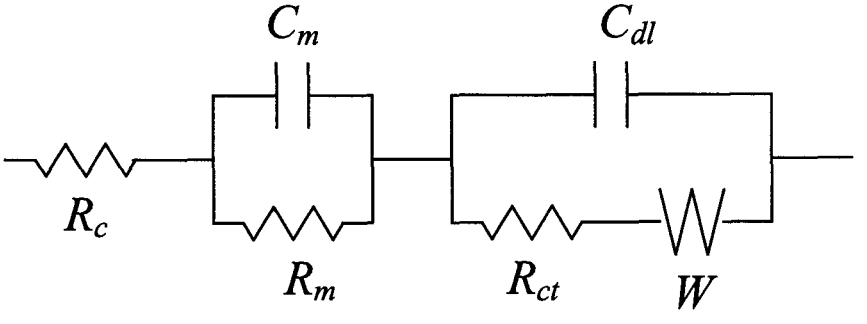

Figure 4.11: Model Proposed By Beattie *et al.*[54] for gold electrode/BAM membrane interface impedance.

4.2.1.2.2 Eikerling et al. *Model* [55]

Eikerling *et al.* [55] model the catalyst layer as a one dimensional transmission line equivalent circuit with R_p is the proton resistance, R_{ct} is the charge transfer resistivity, R_{el} is the electron resistance, and C_{dl} is the double layer capacitance.

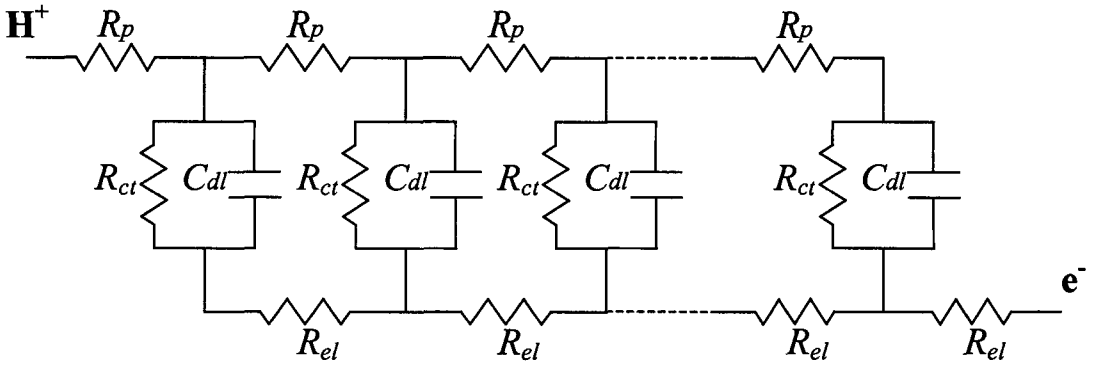

Figure 4.12: Model Proposed by Eikerling *et al.* [55] to Model the Catalyst Layer.

4.2.1.2.3 Baschuk et al. *Model* [56]

Baschuk *et al* propose a model for the ohmic losses at the fuel cell electrode and plate interface (Figure 4.13).

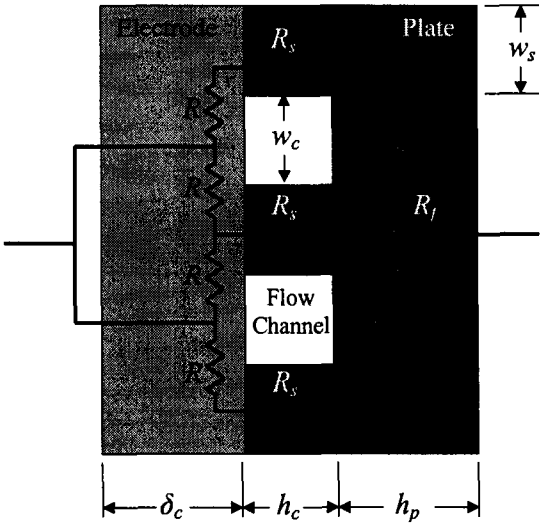

Figure 4.13: Model proposed by Baschuk *et al.* [56] to describe the effective equivalent electrical resistance of the electrode and flow-field plate.

In the Baschuk *et al.* model [56] the total resistance of the electrode (R_t - effectively ΣR from Figure 4.13) can be expressed as follows:

$$R_t = \frac{\rho_{R,e}^{eff}}{8 \cdot n_g \cdot \delta_c \cdot l} \cdot (w_c + w_s)$$

Eq 4-3

Where w_c is the width of the flow channel, w_s is the width of the flow plate support, n_g is the number of flow channels, δ_c is the thickness of the electrode, l is the length of the electrode and $\rho_{R,e}^{eff}$ is described in Eq 4-4.

$$\rho_{R,e}^{eff} = \frac{\rho_{R,e}}{(l - \Phi_e)^{3/2}}$$

Eq 4-4

Where $\rho_{R,e}$ is the bulk resistivity of the electrode, and Φ_e is the void fraction of the electrode.

The total resistance of the plate R_p is described by Baschuk *et al.* [56] as follows:

$$R_p = \frac{\rho_{R,p}}{L} \cdot \left(\frac{h_p}{W} + \frac{h_c}{W - n_g \cdot w_c} \right)$$

Eq 4-5

Where $\rho_{R,p}$ is the resistivity of the plate, h_p is the height of the solid portion of the plates, h_c is the height of the flow channels, and W is the width of the plate.

4.2.2 Solid Oxide Fuel Cell (SOFC) Models

Equivalent circuits used to model SOFC impedance were also examined (Figure 4.14 to Figure 4.17) because of similarities between published SOFC impedance data and PEMFC experimental data. SOFC equivalent circuits were used to model data and modified to develop further models. All the models below were used to fit our experimental data from PEMFCs but none fit well enough to pursue further. Less focus

will be given to the physical significance of the parameters in the models in this section as they are for a different type of fuel cell.

Jiang *et al.* [57], Diethelm *et al.* [58], Bieberle *et al.* [59] Matsuzaki *et al.* [60] and Wagner *et al.* [61] have all proposed equivalent circuit models to model the impedance of SOFC (Figure 4.14 to Figure 4.17).

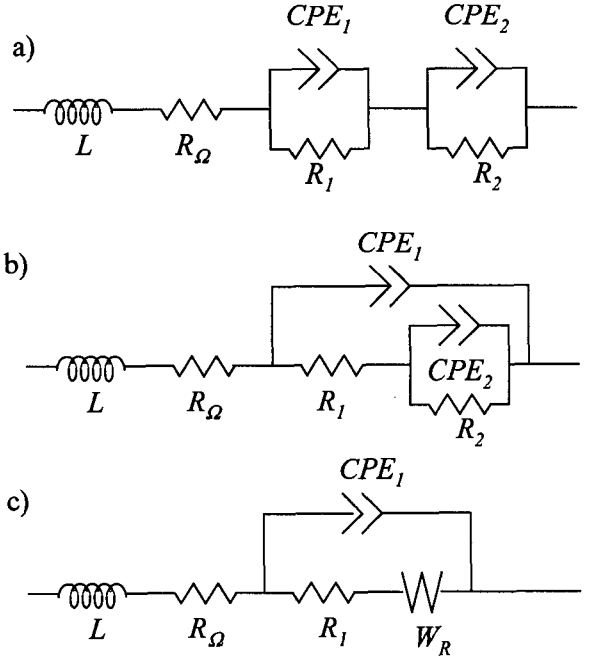

Figure 4.14: Models Proposed by Jiang *et al.* [57] to model SOFC impedance: a) A series Rc, b) nested RC, c) R-type impedance.

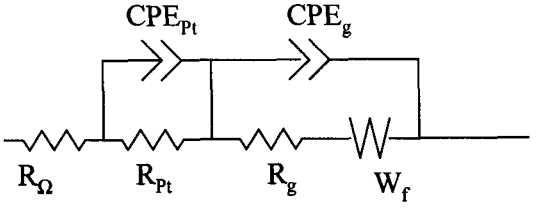

Figure 4.15: Model Proposed by Diethelm *et al.* [58] to Model SOFC Impedance.

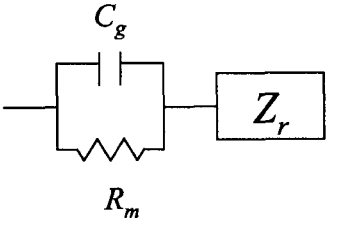

Figure 4.16: Model Proposed by Bieberle *et al.* [59] to Model SOFC Impedance.

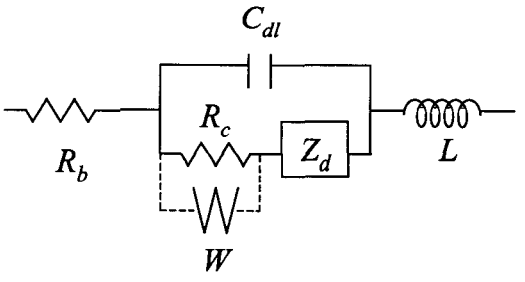

Figure 4.17: Model Proposed by Matsuzaki *et al.* [60] to Model SOFC Impedance.

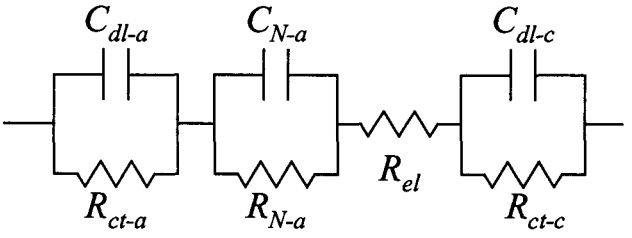

Figure 4.18: Model Proposed by Wagner *et al.* [61] to Model SOFC Impedance.

4.2.3 Direct Methanol Fuel Cell Model

Müller *et al.* [62,63] have also done impedance studies on direct methanol fuel cells (DMFC) that display some similarities to the work done on PEMFCs. Their equivalent circuit model (Figure 4.19) has been used as a part of several of the modified models explored.

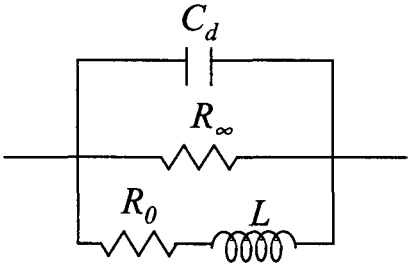

Figure 4.19: Model Proposed by Müller *et al.* [63] to Model DMFC Fuel Cell Anode Impedance Behavior.

This model was also used, on its own and as a series sub-circuit in data modeling but is not a useful model alone for PEMFC experimental data.

4.3 Subtraction

A subtraction method was used as an approach to develop an equivalent circuit model piece by piece from the experimental data. A model was developed using this method but was later found to be flawed because of problems found with the precision of parameters used in its development. The work using the subtraction method and subsequent problems led to further work on the determination of the circuit parameters used to describe the high frequency semi-circle (Section 6) but did not lead directly to a viable circuit.

When circuit elements are in series (Figure 4.20), the total impedance (Z_t) is the sum of the impedances of each of the series elements (Z_i), where n is the number of series elements:

$$Z_t = \sum_{i=1}^{n} Z_i$$

Eq 4-6

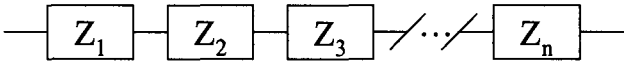

Figure 4.20: Circuit elements in series

This implies that a series element or branch can be removed by subtracting its impedance from the total impedance to leave a remainder (Z_R). So to determine the impedance without the first series loop (Z_1), Z_1 is subtracted off the total impedance (Z_t) to give the remaining impedance (Z_R):

$$Z_R = Z_t - Z_1$$

Eq 4-7

4.4 Trial and Error

A certain amount of educated trial and error was used to develop new models. Components of models developed through subtraction and circuit equivalence as well as from models found in the literature and early in-house models were combined to develop new models.

4.5 Comparison Results

4.5.1 Model Comparisons for Non-Fault Condition Data

Early work was done fitting non-fault condition data. From this work models were compared to determine the best model for non-fault condition impedance data. The models chosen were determined to be the best fit through an averaging of the χ^2 parameter for the fits to several spectra. The χ^2 values shown are from a single representative spectrum.

Through trial and error, modification, and comparison with the χ^2 and F-Test statistics, four models were found to be the best fits with 7, 8, and 9 parameters (Figure 4.21-Figure 4.23). These models were used to only fit data in the 50 Hz-50 kHz frequency range; none of them fit the third semicircle feature. The physical features of the impedance data led to these choices for the number of parameters. The shape of impedance data can also be used as a simple indicator of the number and type of parameters for the equivalent circuit to model it. For example, three semicircles indicate that a six-parameter model (with three time constants) would be appropriate. In our case, two of the semicircles have flattened sections, indicating the possibility of another parameter for the corresponding semicircle, leading to an 8 or 9 parameter model for the entire impedance spectrum. Sometimes the second semicircle has two poorly-resolved arcs which is why 7-9 parameter models were used to fit only in the 50 Hz to 50 kHz region. Models with more than 9 parameters were examined but were found with the F-Test to not be statistically significant improvements.

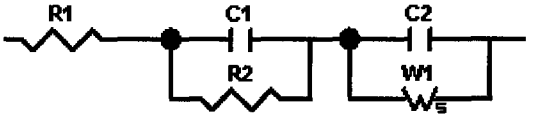

Figure 4.21: Best 7 parameter model from model modification tests: Model Mod 25; Chi-squared = 8.8051E-6, Sum of Weighted Squares = .00064277

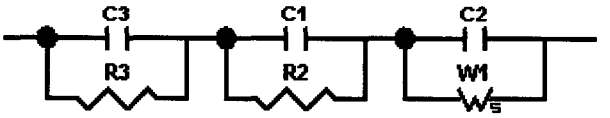

Figure 4.22: Best 8 parameter model from modification tests: Model Mod 23; Chi-squared = 7.1674E-6, Sum of Weighted Squares = .00051605

Figure 4.23: Best 9 parameter model from modification tests: Model Mod 17; Chi-squared = 6.9691E-6, Sum of Weighted Squares = .00049481

Between the best 7-parameter model (Figure 4.21) and the best 8-parameter model (Figure 4.22) the F-ratio percent is 0.014% suggesting that the 8-parameter model is a better fit. Between the 8-parameter model (Figure 4.22) and the 9-parameter model (Figure 4.23) the F-ratio percent is 16.25%, suggesting that the 8-parameter model is statistically better

Of note, the fitting error associated with several parameters when using the 8-parameter model (Figure 4.22) is higher than with some previous models with an average error of 17 % on individual parameters (Table 4-1). A maximum parameter error of 5% or less would be preferred. Despite this issue, when the χ^2 values are compared between this 8-parameter model and others, it is found to be the better model.

Table 4-1: Parameter Values and Error for Best 8 Parameter Model (Figure 4.22) fit ti Typical Impedance Spectra (Section 3.3).

Parameter	Value	%Error
C3	0.029 $F \cdot cm^{-2}$	34
R3	0.029 $\Omega \cdot cm^2$	42
C1	0.00012 $F \cdot cm^{-2}$	2.3
R2	0.20 $\Omega \cdot cm^2$	1.9
C2	$1.2 \cdot 10^{-5}$ $F \cdot cm^{-2}$	43
W1-R	0.80 $\Omega \cdot cm^2$	1.8
W1-T	0.011 s	9.4
W1-P	0.38	2.2

Another 10-parameter model (Figure 4.24) has been explored as well for fitting the entire spectrum. It was not compared statistically with other models because the range of frequencies it fits is quite different.

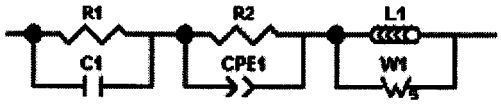

Figure 4.24: 9 Parameter Model Which Fits the Entire Frequency Range.

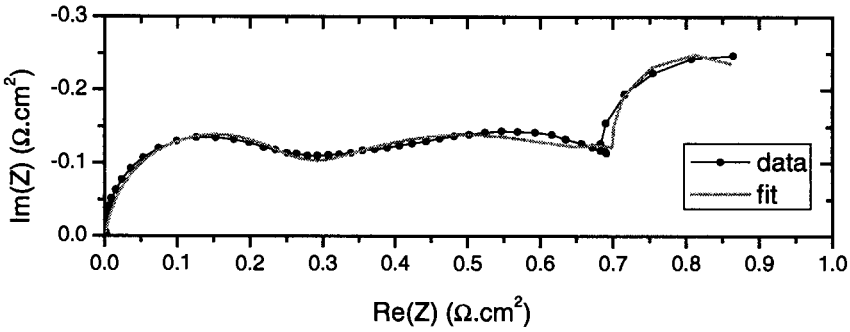

Figure 4.25: Nyquist Plot of Experimental Impedance Data[ii] and Fit with Full Frequency 9 Parameter Model (Figure 4.24)

4.5.2 Models for Fault Condition Impedance

The best models from the analysis on non-fault condition impedance data were used to analyze the fault condition dataset impedance. Because CNLS is very sensitive to the starting parameters for a fit, the same starting parameters were chosen for all the files in each fault dataset. Starting parameters are the initial values of parameters which the CNLS fitting algorithm uses as an initial "guess" to begin looking for convergence. The initial set of starting parameters for a dataset was determined through fitting a standard set of starting parameters to the initial "normal conditions" file in the dataset. In this manner a consistent set of starting parameters was used for each file within a single fault dataset, but different starting parameters were used for each fault dataset.

[ii] Spectrum conditions April 17 2002: H_2/O_2, T_{cell} 70 °C, Ballard MEA, j=0.4 A.cm^{-2}.

4.5.3 Model for Entire Frequency Range

The full frequency 9 parameter model shown in Figure 4.24 was determined in to be a good fit over the entire frequency range for normal operating conditions datasets. It was also shown to be a good fit for drying fault datasets ($\chi^2 = 8.5 \times 10^{-5}$) but does not converge for severe CO poisoning fault conditions.

At high levels of CO poisoning the Warburg and CPE parameters will not consistently converge to specific values. This means that fits performed with converged fit parameter values as starting values will not converge to similar values, if they converge at all. This leads to concerns about this model's suitability to fit CO poisoning impedance and thus as a tool to differentiate between drying and CO poisoning faults.

4.5.4 Limited Frequency Range Models

4.5.4.1 8 Parameter Model

The 8 parameter model shown in Figure 4.22, which was shown to have statistically the best fit of models attempted for non-fault condition datasets, will fit drying datasets ($\chi^2 = 2.8 \times 10^{-5}$) but with some problems with the consistent convergence of the *C2* parameter. This model experiences similar problems to the 9 parameter model (Section 4.5.3) with respect to fitting CO poisoning impedance data. Both the Warburg and *C2* parameters will not consistently converge. The problems with convergence for this model for both drying and CO poisoning data prevent it from being an effective tool to differentiate between drying and CO poisoning condition.

4.5.4.2 7 Parameter Model

The best, limited frequency, 7 parameter model (Figure 4.21) was investigated because of the problems encountered fitting fault condition impedance data with the full frequency 9 parameter model, and the limited frequency 8 parameter model. The 7 parameter model

fits well for drying dataset ($\chi^2 = 3.8 \times 10^{-5}$) and well for CO poisoning datasets ($\chi^2 = 5.3 \times 10^{-6}$). This model consistently converged for all CO poisoning and drying impedance spectra.

4.5.4.3 Other Models

In the literature[51,52,53] there is some suggestion that replacing capacitors in models which fit normal PEM impedance with CPEs provides a better fit to CO poisoning impedance data. Several models were developed (Figure 4.26-Figure 4.28) using this concept based on the 7 parameter model (Figure 4.21). None of the models were a statistically significant improvement over the 7 parameter model when the χ^2 results for CO and drying dataset fittings were compared straight on and using the F-test . Further information about the F-Test can be found in Section 2.2.4.2.

The first model modification, and 8 parameter model, is not an improvement over the 7 parameter model (χ^2 = 5.07E-06) as the χ^2 value is higher. The second model modification, also an 8 parameter model, is an improvement (has a lower χ^2) but the improvement is not sufficiently significant for a 56 degree of freedom system with an F-ratio of 5.42 and an F-percent of 2.01%. The third model is a significant improvement over the first and the second but its relationship to the 7 parameter model is difficult to establish.

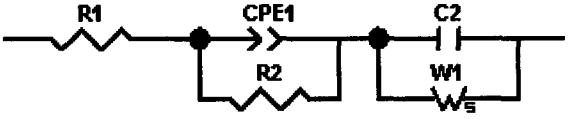

Figure 4.26: Equivalent Circuit Model Modification 1: Capacitor C1 from Figure 4.21 Replaced with a CPE. χ^2 = 4.99E-05.

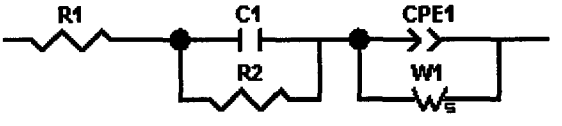

Figure 4.27: Equivalent Circuit Model Modification2: Capacitor C2 from Figure 4.21 Replaced with a CPE $\chi^2 = 4.60E-06$.

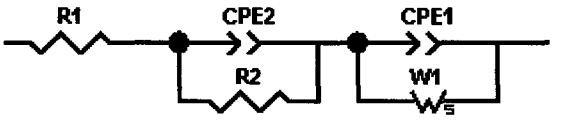

Figure 4.28: Equivalent Circuit Model Modification 3: Capacitors C1 and C2 from Figure 4.21 Replaced with CPEs. $\chi^2 = 3.53E-06$.

4.6 Conclusions

Because of its relatively good ability to fit non-fault impedance data, and its ability to converge on fault condition impedance data, the 7 parameter model shown in Figure 4.21 was chosen as the best model, of those attempted, for the purposes of differentiating between drying and CO poisoning fault conditions.

5 Equivalent Circuit Model Results

The philosophy of our approach to equivalent modeling was to take a more empirical and less physical approach. Parameters were only added if their statistical significance could be proven. No attempts were made to determine anodic and cathodic contributions to the fuel cell impedance through the equivalent circuit modeling, but this is certainly an area for future work. More data from separate experiments measuring anode and cathode impedances individually in a functioning fuel cell would really be required to satisfactorily separate the contributions. This is outside of the diagnostic scope of this work.

The equivalent circuit used in this work to generally model the impedance of fuel cells is shown in Figure 4.21. Figure 5.1 shows the three sections of the circuit as they are discussed in this section: Resistor *R1*, Parallel Resistor *R2* and Capacitor *C1*, and Parallel Capacitor *C2* and Warburg *W1*.

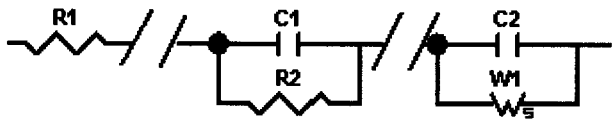

Figure 5.1: Three Section of Equivalent Circuit Shown in Figure 4.21

All of the fault datasets described in Section 3 were fit with this circuit using ZView™, an EIS data fitting program. This program uses a CNLS fitting algorithm to fit a specified range of experimental impedance data to an equivalent circuit model. Unit weighting was used as the weighting option. Each dataset was fit within the 50 Hz to 50 kHz frequency range. The Drying1, Drying2, CO Poisoning, and Dual Fault dataset fit results for each parameter are shown together on plots with time. Because the Flooding Dataset is not chronological the fit results are shown on separate graphs.

For reference, Figure 5.2 shows the change in potential with time for the Drying1, Drying2, CO Poisoning, and Dual Fault datasets. The degree of fault can, to some degree, be indicated by the degree of decrease in potential.

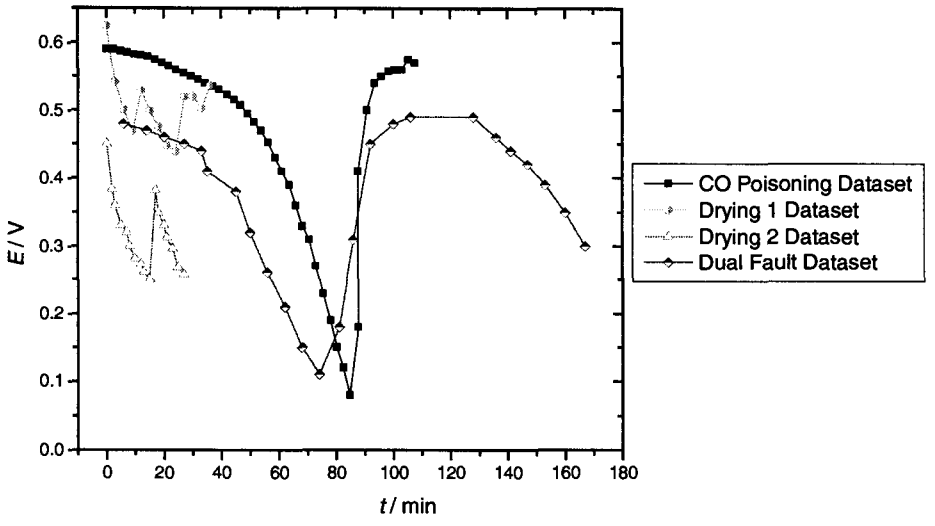

Figure 5.2: Potential Vs. Time for CO Poisoning, Drying 1, Drying 2, and Dual Fault Datasets.

5.1 Resistor R1

The resistance of the resistor *R1* element is thought to be associated with a contact resistance originating from contact between the GDL, electrode, and the collector plates. This resistance can be seen on Nyquist representations as the real intercept of the high frequency impedance with the Nyquist Re(Z) axis. Although the resistor R1 values shows some small change with fault data and could possibly be used for diagnostics based on that fact, it is likely that this change is due to a fitting artifact associated with the fact that the frequency range of data fitted does not extend all the way to the real axis so this is an extrapolated value. This is particularly apparent with the dual fault dataset R1 values where there is more variation and much smaller values. In this dataset the impedance was only acquired up to 5 kHz so the spectra from the dual fault dataset could not be fitted in the 5 kHz to 50 kHz regions, creating greater fitting error in the R1 parameter.

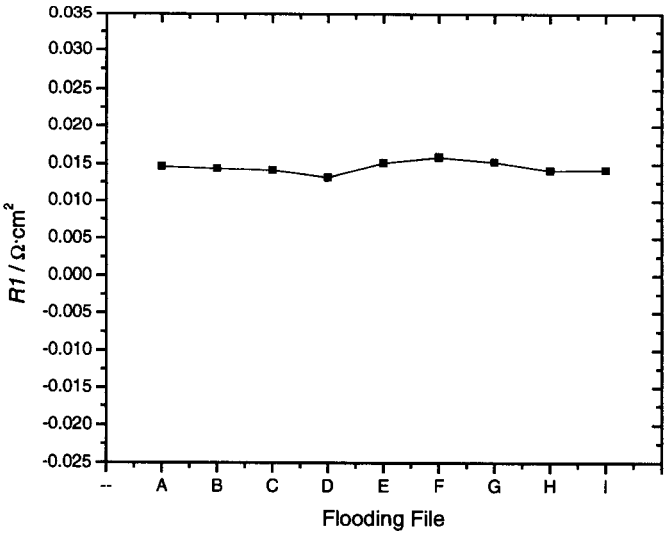

Figure 5.3: Resistor *R1* Values (Figure 5.1) for Flooding Dataset.

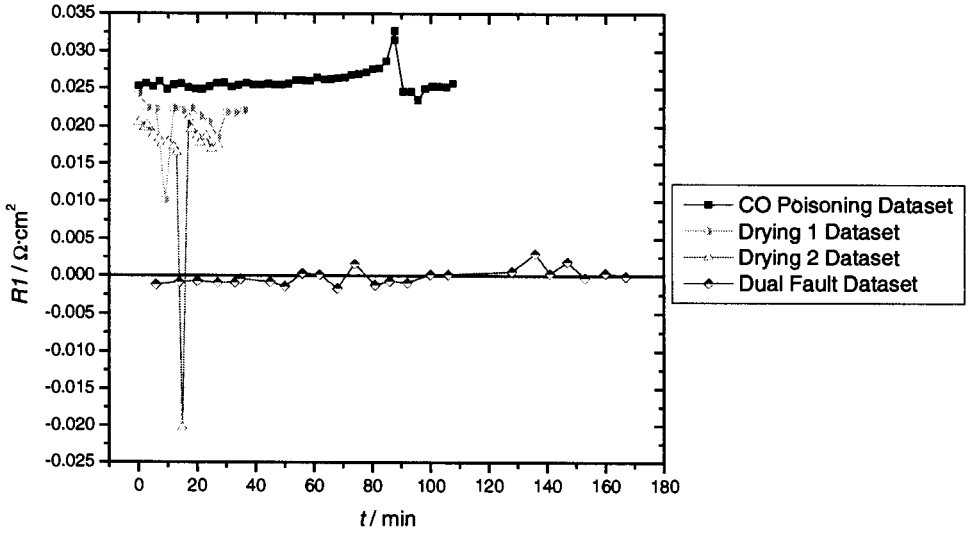

Figure 5.4: Resistor *R1* Values (Figure 5.1) as a Function of Time for CO Poisoning, Drying 1, Drying 2, and Dual Fault Datasets.

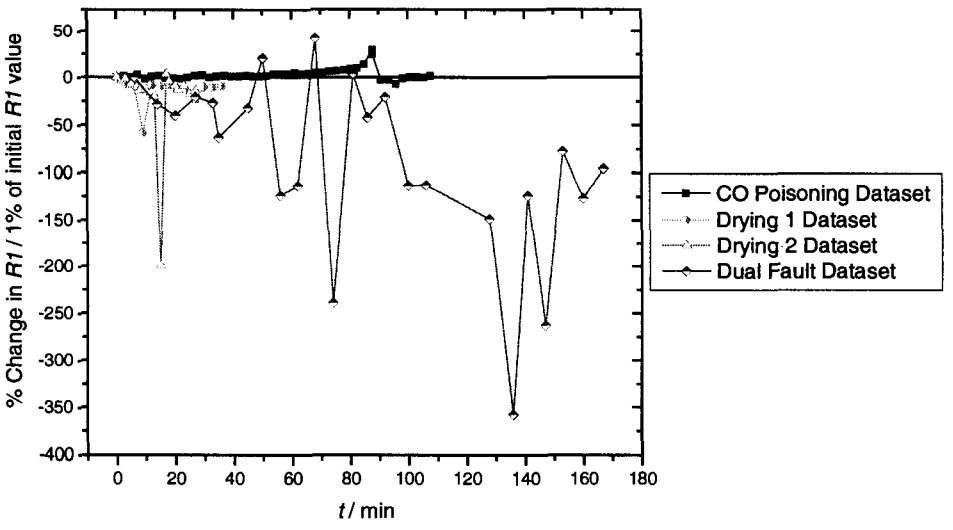

Figure 5.5: Percent Change in Resistor *R1* Values (Figure 5.1) from Normal Conditions as a Function of Time for CO Poisoning, Drying 1, Drying 2, and Dual Fault Datasets.

There is very little change in the R1 parameter with flooding.

Compared to other parameters of the equivalent circuit, the resistance of resistor *R1* does not change much with time during faults (Figure 5.3-Figure 5.5). The value decreases as voltage decreases for drying faults, but increases as the voltage decreases for the CO poisoning fault. There is an average fitting error for this parameter of 15% for the Drying 1 dataset and 9% for the Drying 2 dataset. This is within the range of the percent change from original *R1* values for both drying datasets and leads to some concerns about the statistical significance of the decrease of the *R1* parameter during a voltage decrease due to drying. For CO poisoning the average fitting error for the *R1* parameter was 3.7%. This is approximately an order of magnitude smaller than the percent change in *R1* from the original value for CO poisoning. This suggests that the correlation between an increase in the *R1* parameter and a decrease in voltage due to CO poisoning is real. Of note are the point at t = 10 min for the *R1* for Drying 1 and the point at t = 15 min for the *R1* for Drying 2. Both of these points are where recovery from drying is occurring and both have relatively high error (130% and 44% for Drying 1 and Drying 2 points respectively).

For the Dual Fault dataset, there is some correlation between the *R1* parameter and the voltage drops due to drying and CO poisoning. It appears that the *R1* parameter increases as the voltage drops due to CO poisoning and decreases as the voltage drops due to drying, as in the single fault datasets. This is highly suspect though, because the average fitting error for this parameter is 480% (larger than the percent change spread of the data). It is possible that neither of these trends are statistically significant. It should also be noted that the fitting error for the *R1* parameter for this dataset is much higher (480%) than the fitting error for the *R1* parameters for the other datasets (3.7% to 14.9%). This is likely due to the fact that this parameter is most affected by the high frequency impedance and other datasets, were fitted over a 50 Hz to 50 kHz frequency range, while the dual fault dataset was fitted over a 50 Hz to 5 kHz range, as frequencies above 5 kHz were not acquired. The inability to fit the newer data over the 5 kHz to 50 kHz range could be one of the factors influencing the high error for the *R1* parameter when fitting the dual fault dataset.

5.2 Parallel Resistor R2 and Capacitor C1

The first semi-circle feature can consistently be represented by a resistor-capacitor (*R-C*) parallel circuit in series with the remaining impedance (Z_r) (Figure 5.6) for the impedance data collected.

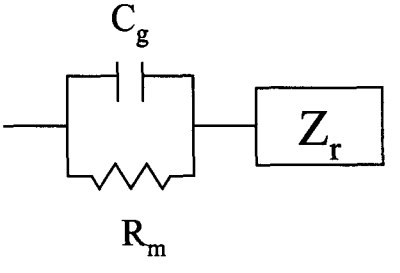

Figure 5.6: Equivalent circuit for the first semicircle, with geometric capacitance (*Cg*) in parallel with membrane resistance (*Rm*) all in series with the remaining impedance (Z_r).

Resistor *R2* is associated with the membrane resistance while *C1* is associated with the geometric capacitance. Work on circuit development with the subtraction method lead to

a thorough investigation of the first semicircle and the *R2* and *C1* parameters and a better understanding of these parameters than of the others.

5.2.1 Resistor R2

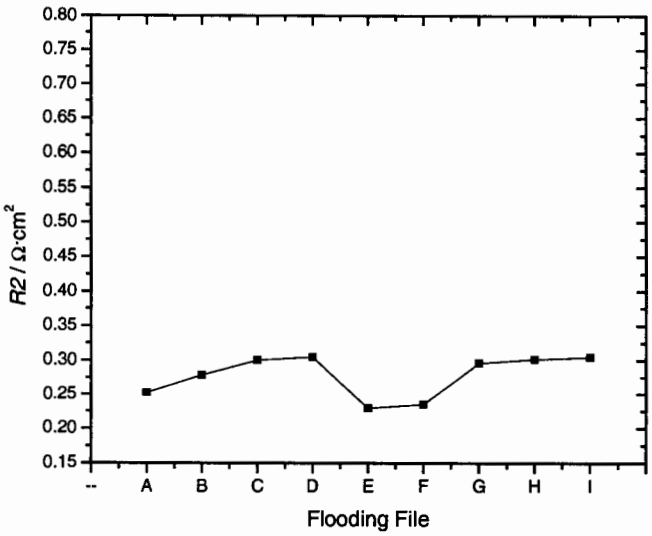

Figure 5.7: Resistor *R2* Values (Figure 5.1) for Flooding Dataset.

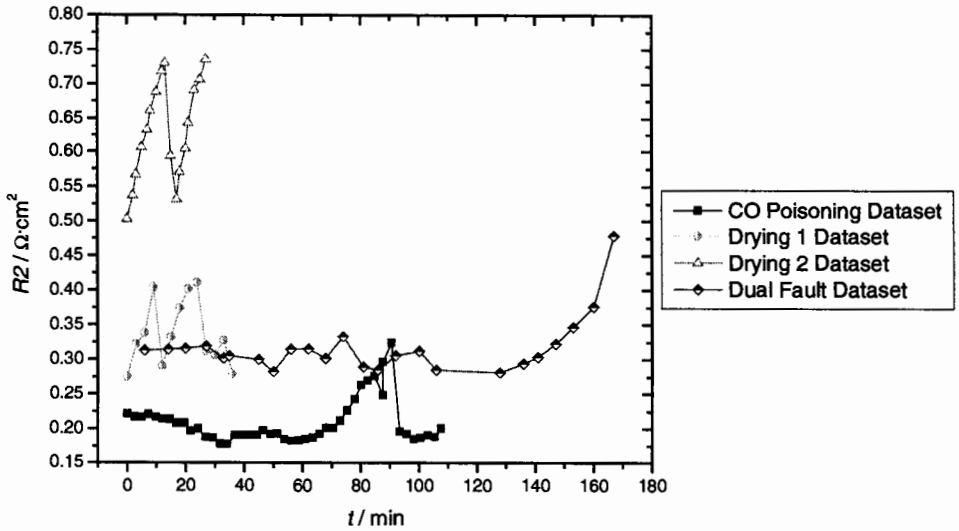

Figure 5.8: Resistor *R2* Values (Figure 5.1) as a Function of Time for CO Poisoning, Drying 1, Drying 2, and Dual Fault Datasets.

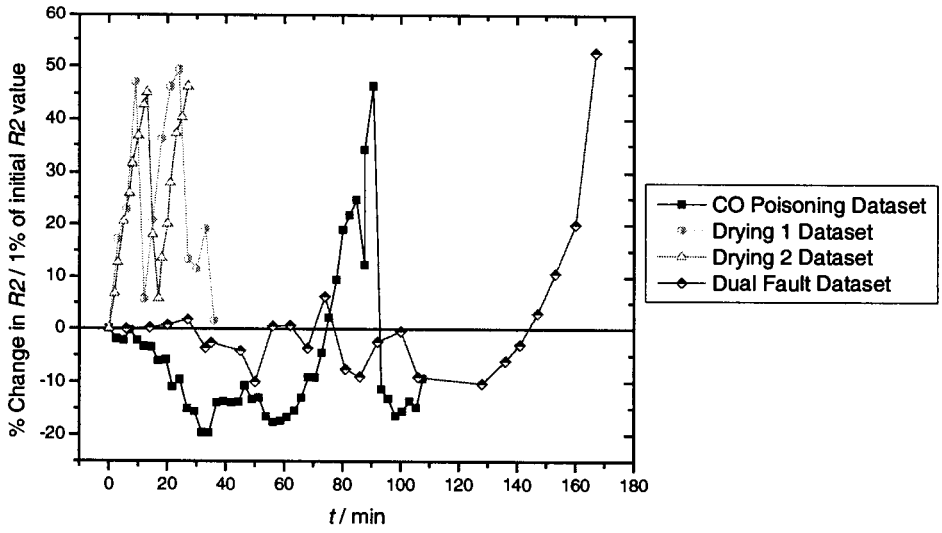

Figure 5.9: Percent Change in Resistor *R2* Values (Figure 5.1) from Normal Conditions as a Function of Time for CO Poisoning, Drying 1, Drying 2, and Dual Fault Datasets.

The *R2* resistance parameter changes as the voltage changes for both drying and CO poisoning faults (Figure 5.8-Figure 5.9). For both drying and CO poisoning faults, the resistance of the *R2* resistor increases as the voltage decreases during fault conditions. The average fitting error for the *R2* parameters are 4.8% for Drying 1, 3.7% for Drying 2, and 5.4 % for CO poisoning datasets. These are all at least an order of magnitude less than the percent change in *R2* due to the faults. For the Drying 1 and Drying 2 datasets this correlates with a clear increase in the size of the first semicircle feature in the impedance with a increase in the *R2* parameter as the degree of drying increases (Figure 5.10).

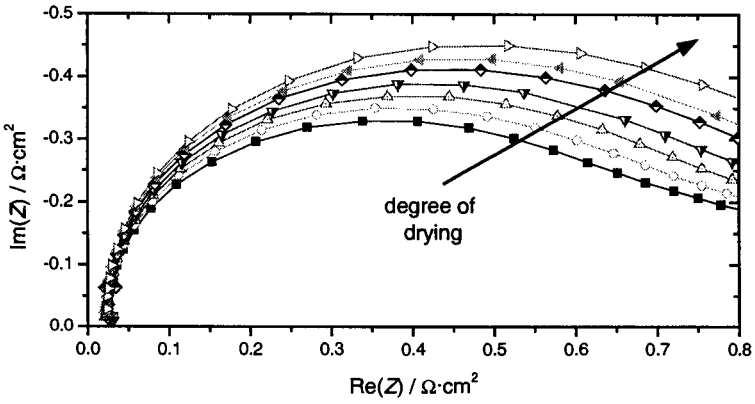

Figure 5.10: Detail of Figure 3.11 with Focus on First Semi-Circle Impedance Feature.

The R2 resistance parameter increases during flooding conditions (Figure 5.7).

For the dual fault dataset the *R2* resistance parameter increases with drying but not with CO poisoning (Figure 5.8-Figure 5.9). This agrees with the Drying 1 and Drying 2 results but not the CO poisoning results. This discrepancy may arise due to the fact that during severe CO poisoning the first arc impedance feature is poorly resolved (Figure 5.11) and there can be difficulties differentiating between the first and second arc when fitting. The fact that the CO Poisoning was likely more severe in the CO poisoning dataset than the dual fault dataset (the decrease in voltage and change in impedance shape were both greater for the CO poisoning dataset) probably played a role in the discrepancy as well. The average fitting error for the *R2* parameter for the dual fault dataset was 5.9%.

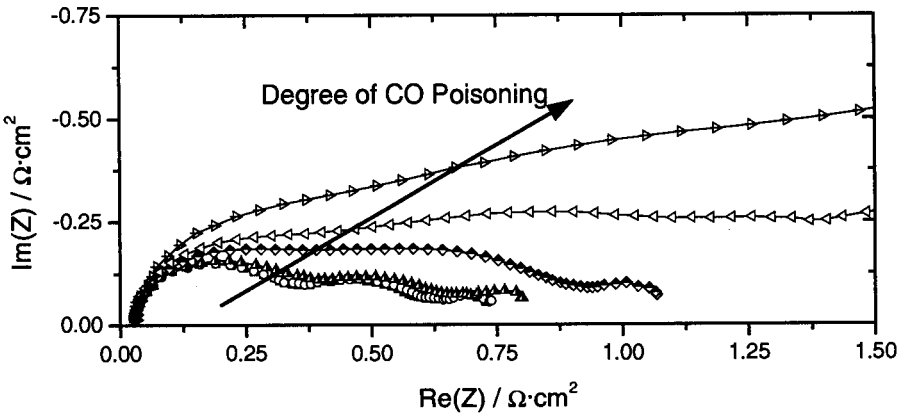

Figure 5.11: Detail of Figure 3.17 with Focus on First Semi-Circle Impedance Feature.

5.2.1.1 Membrane Resistivity

The *R2* parameter can be associated with the membrane resistivity. The comparison of the membrane resistivity results from this work with other published results (Table 5-1) shows that we are within the published range, although the published range varies highly.

Table 5-1: Membrane Resistivity: Comparison with Published Results

Publication	Membrane Resistivity (Ω·cm)
This work	12-60
Friere *et al.*[64iii]	24-32
Andreaus *et al.*[49]	7.42-11.01
Ciureanu *et al.*[52 iii]	12.5-1750[iv]
Ciureanu *et al.*[51 iii]	12.5-750[iv]
Ciureanu *et al.*[53 iii]	2.5-63
Büchi *et al.*[65 iii]	10-11.25

5.2.2 Capacitor C1

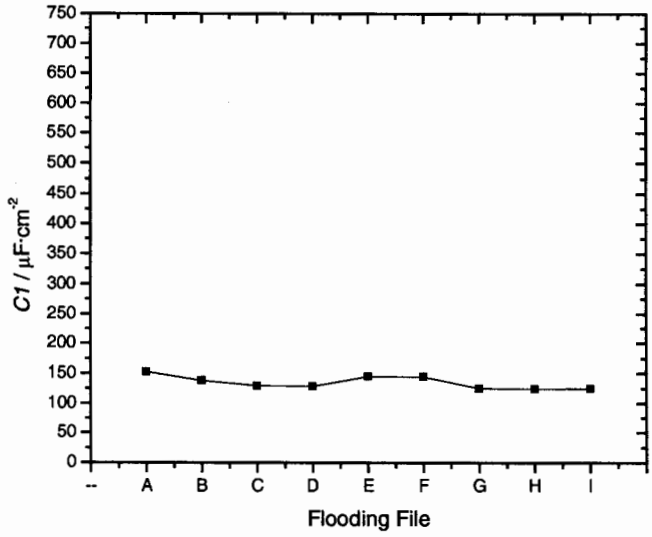

Figure 5.12: Capacitor *C1* Values (Figure 5.1) for Flooding Dataset.

[iii] Taken from resistance and membrane thickness data presented.
[iv] High values associated with CO poisoning results where the first arc is often not well resolved

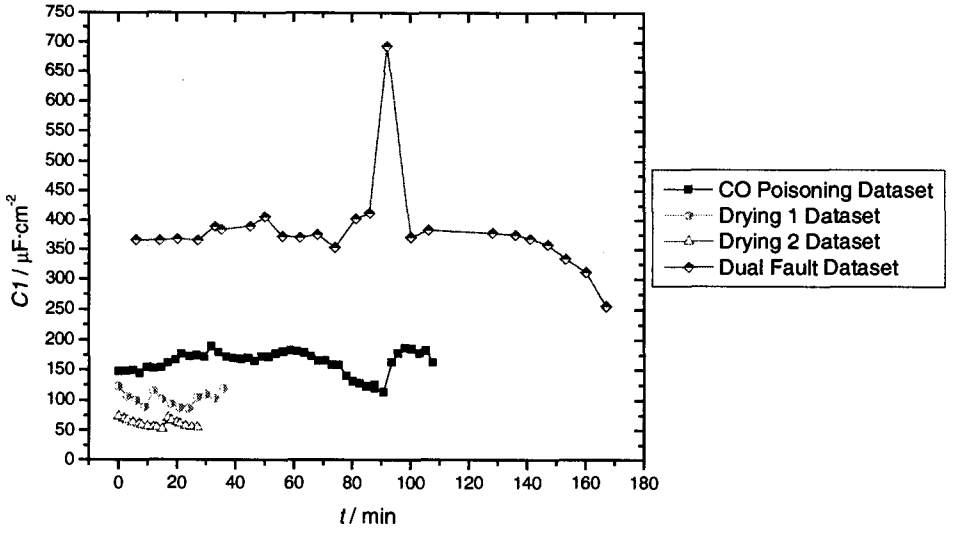

Figure 5.13: Capacitor *C1* Values (Figure 5.1) as a Function of Time for CO Poisoning, Drying 1, Drying 2, and Dual Fault Datasets.

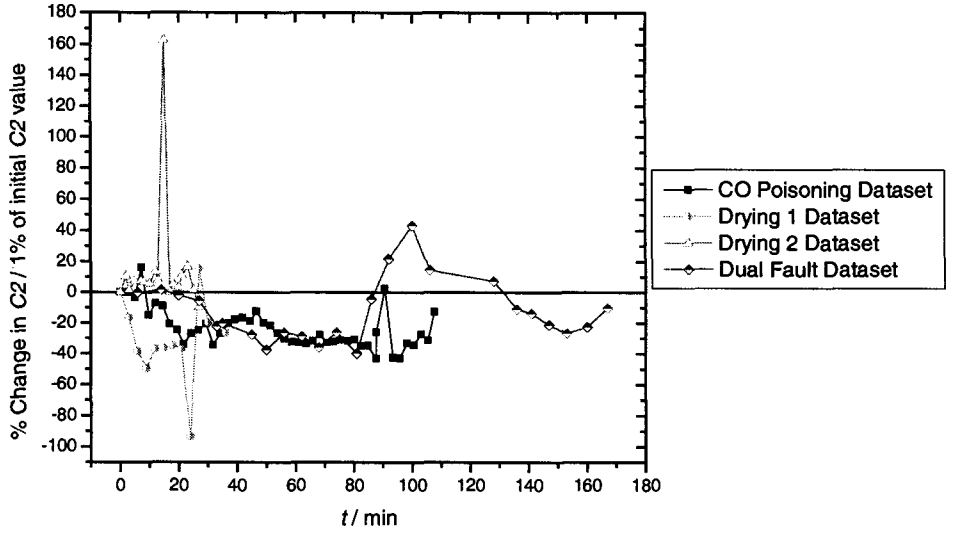

Figure 5.14: Percent Change in Capacitor *C1* Values (Figure 5.1) from Normal Conditions as a Function of Time for CO Poisoning, Drying 1, Drying 2, and Dual Fault Datasets.

The fitted values for the capacitor *C1* correlate fairly well with voltage for drying datasets where the capacitance value decreases as the voltage decreases due to the fault (Fig. 5.9). There is some correlation between the drop in capacitance *C2* and the drop in voltage due to CO poisoning. The average fitting errors for the *C1* parameter are 5.4% for Drying 1, 3.1% for Drying 2, and 6.1% for CO poisoning datasets respectively.

For the dual fault dataset, the capacitance *C1* decreases as the voltage decreases with the drying fault as with the Drying 1 and Drying 2 datasets. The CO poisoning behavior for the dual fault dataset was similar to that of the CO poisoning dataset, a slight decrease in *C1* with a decrease in voltage. There is also a spike in the *C1* value during the air bleed recovery from CO poisoning. The average fitting error for *C1* was 4.2% for the dual fault dataset.

5.2.2.1 Geometric Capacitance

Capacitor *C2* can be associated with the geometric capacitance of the membrane (Section 2.2.1.2.2). If the membrane thickness is known (d = 125 μm in this case), the dielectric constant of the material (ε_r), also referred to as relative permittivity, can be backed out of the capacitance using the following formula (if the capacitance is expressed as $F.cm^{-2}$):

$$\varepsilon_r = \frac{C_g \cdot d}{\varepsilon_o}$$

Eq 5-1

Where ε_o is the permittivity of vacuum ($\varepsilon_o = 8.854 \cdot 10^{-12}$ $F.m^{-1}$). Using the *C2* results shown in Figure 5.13 and Eq 5-1 the dielectric constant of Nafion® was calculated for each of the experiments (Figure 5.15). For all experimental data the average dielectric cosntant of Nafion® was 2700. This is considerably higher than was expected. Published data[66] suggests that the real part of the complex dielectric constant (ε') is generally around 4, but this is in the high frequency range (>MHz). The first semicircle feature with which this capacitance *C2* is associated for our data is generally in the 1-50 kHz frequency range There are also some published results showing the dielectric constant of approximately 3 in the 10^{-1} – 10^{5} Hz frequency range[67] for Nafion methyl ester carboxylate polymers, but the authors of that study cite, without criticism, the work of Mauritz *et al.* Mauritz *et al.* describe the complex dielectric behaviour of NaOH and NaCl containing Nafion® membranes[68], CH_3COONa, KCl, and KI containing Nafion® membranes[69], $ZnSO_4$ and $CaCl_2$ containing Nafion® membranes[70], and the effect on dielectric behaviour of long range ion transport[71]. These papers cite high values for ε', in

the range of 100-2000 for the 1-50 kHz frequency range. Mauritz *et al.* explain these high dielectric as follows[68]:

> "Because there are significant differences in the polarizabilities and charge mobilities across the hydrophilic/hydrophobic phase boundaries, there will occur the inevitable accumulation and dissipation of net charge at these interfaces along the direction of the applied electric field during each half cycle of field oscillation. [...] It is then easy to visualize the field induced oscillating macrodipoles that are of a size of the order of cluster dimensions. This large-scale charge separation will clearly result in a large *induced* dipole moment per unit volume that is responsible for the high observed dielectric constants"

Deng and Mauritz[7273] later published results for ε' for *Dow Chemical Co.* perfluoro-sulfonate ionomer (PFSI) membranes (similar to Nafion® but with a shorter side chain) containing SO_4^{2-} ions. They also studied the effect of water content. In these studies, for the 1-50 kHz frequency range, the ε' was values ranged from 20,000-60,000 for fully saturated membranes, 1,000-9,000 for membranes with 45.5% water content, and 200-700 for dry membranes. This is interesting not only because it supports the possibility of the dielectric properties of the material being reaponsible for the high dielectric constant but also because it supports the decrease in capacitance, and dielectric constant with drying.

The possibility of high dielectric constant in polymer electrolytes is also supported by Schwarz[74]and Michaels *et. al.*[75].

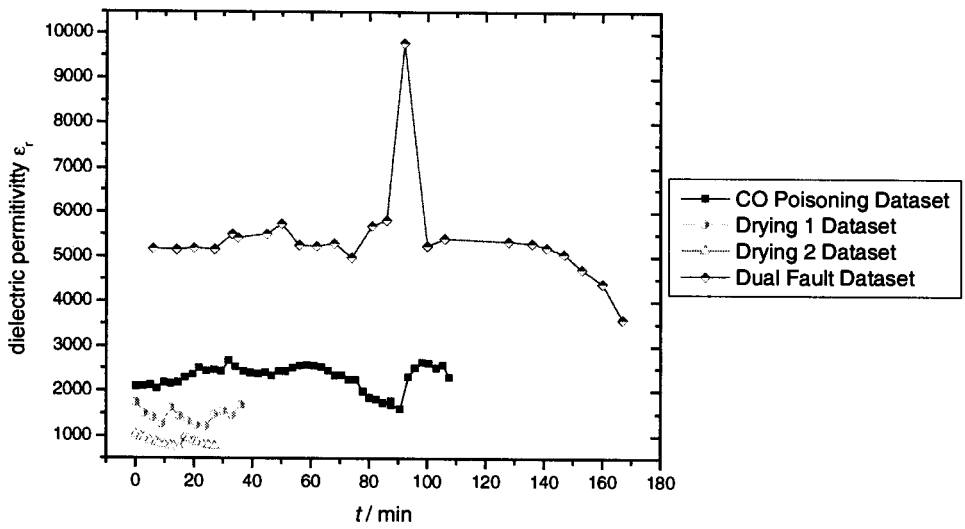

Figure 5.15: Calculated Dielectric Permittivity.

5.3 Parallel Capacitor C2 and Warburg W1

Capacitor *C2* should represent the double layer capacitance and Warburg Element W1 should describe the diffusion.

5.3.1 Capacitor C2

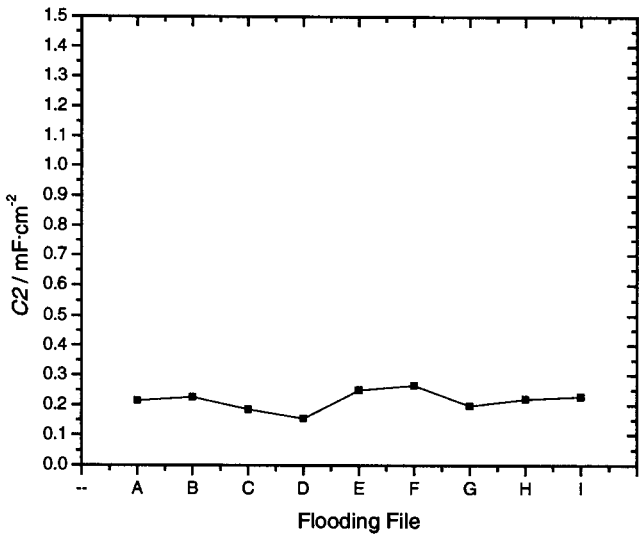

Figure 5.16: Capacitor *C2* Values (Figure 5.1) for Flooding Dataset.

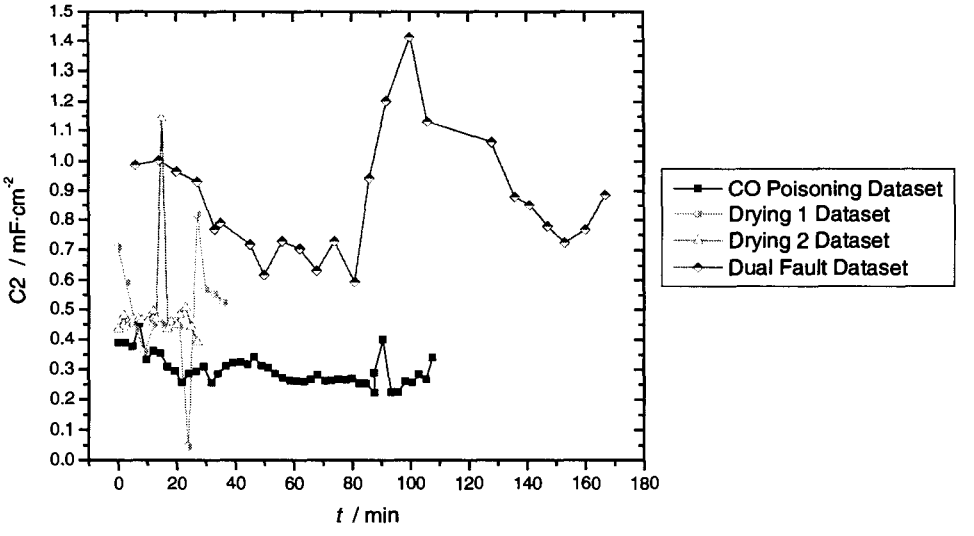

Figure 5.17: Capacitor *C2* Values (Figure 5.1) as a Function of Time for CO Poisoning, Drying 1, Drying 2, and Dual Fault Datasets.

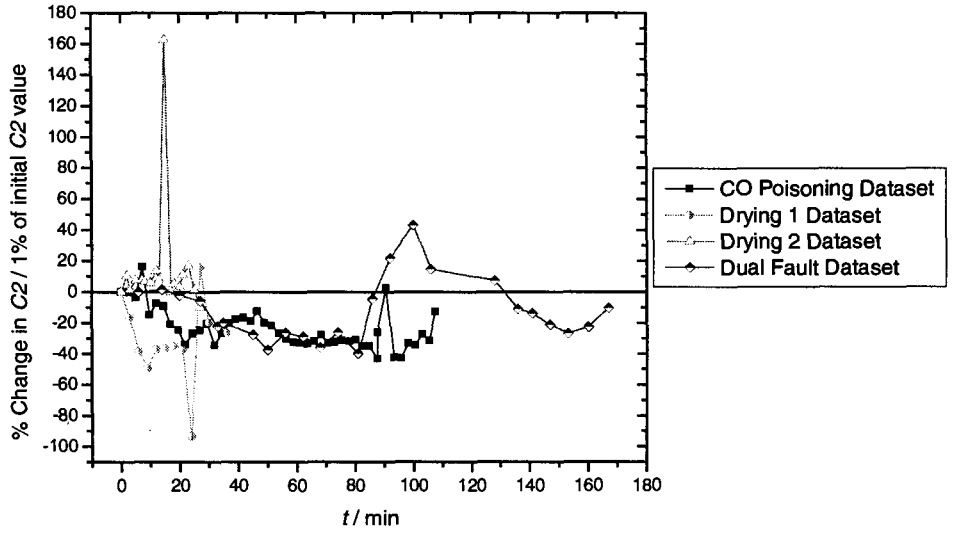

Figure 5.18: Percent Change in Capacitor *C2* Values (Figure 5.1) from Normal Conditions as a Function of Time for CO Poisoning, Drying 1, Drying 2, and Dual Fault Datasets.

Capacitor *C2* values do not appear to be correlated with the voltage for either the drying, flooding or CO poisoning faults. This is supported by the relatively high fitting error and relatively low percent change in this parameter (Figure 5.16-Figure 5.18). The average fitting errors, for the *C2* parameter, are 53.8% for Drying 1, 32.2% for Drying 2, and 17.3% for CO poisoning datasets respectively. Also of note are the points with high percent change for this parameter; t = 15 min for Drying 2, t = 21 min for Drying 1, and t =90 min for CO Poisoning. All of these points are during the fault recovery transition.

For the dual fault dataset the *C2* parameter did not change significantly with voltage decreases due to faults. It did, however, increase significantly during CO poisoning recovery : t =80-110 min (Figure 5.17). The average error for the dual fault dataset *C2* parameters was 12.5%.

The significant changes in the *C2* parameter all occurred during fault recovery. This parameter may be sensitive to impedance spectra acquired during periods of relatively transient conditions. It is likely that *C2* is more are sensitive than *C1* to transient conditions because it is associated with the impedance in a lower frequency range (1-50 kHz for *C1* and 50 Hz – 1 kHz for *C2*) and the lower the frequency, the more likely that transience will affect the acquired data.

5.3.1.1 Double-Layer Capacitance

The double layer capacitance values determined in this work were compared to those from other published results. Our results are within the range of most other results but there is a large spread in the field (4 orders of magnitude).

Table 5-2: Double-Layer Capacitance: Comparison with Published Results

Publication	Double Layer Capacitance ($F \cdot cm^{-2}$)
This work	$1 \cdot 10^{-4} - 2 \cdot 10^{-3}$
Romero-Castañón *et al.*[76]	$1 \cdot 10^{-3} - 2 \cdot 10^{-3}$
Springer *et al.*[77]	$8 \cdot 10^{-3} - 2 \cdot 10^{-2}$
Siroma *et al.*[78]	$1 \cdot 10^{-4} - 6 \cdot 10^{-3}$
Parthasarathy *et al.*[79]	$5 \cdot 10^{-6} - 2 \cdot 10^{-4}$
Ciureanu *et al.*[52]	$7 \cdot 10^{-4} - 9 \cdot 10^{-4}$
Ciureanu *et al.*[51]	$8 \cdot 10^{-4} - 9 \cdot 10^{-4}$

5.3.2 Warburg Element W1

5.3.2.1 Warburg R Parameter

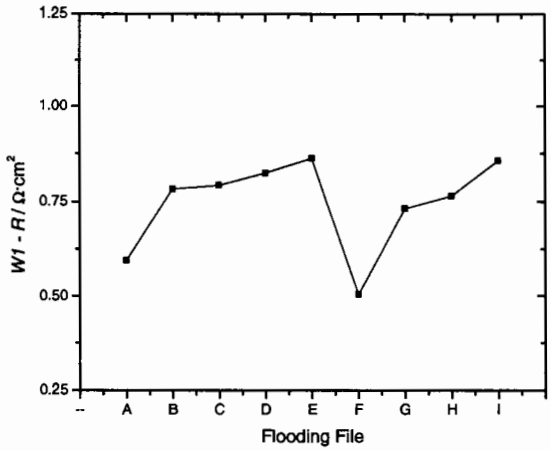

Figure 5.19: Warburg R Parameter (*W1-R*) Values (Figure 5.1) for Flooding Dataset.

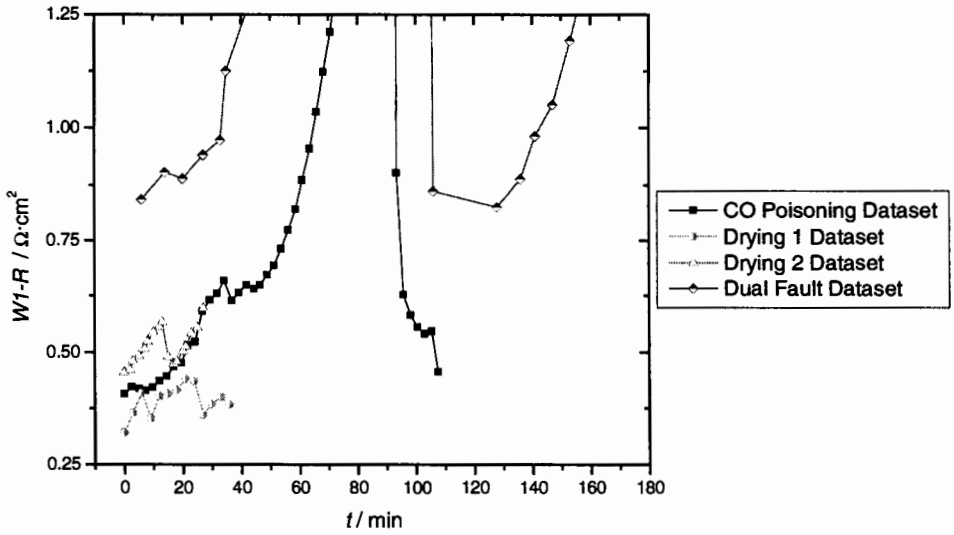

Figure 5.20: Warburg R Parameter (*W1-R*) Values (Figure 5.1) as a Function of Time for CO Poisoning, Drying 1, Drying 2, and Dual Fault Datasets, Partial Scale.

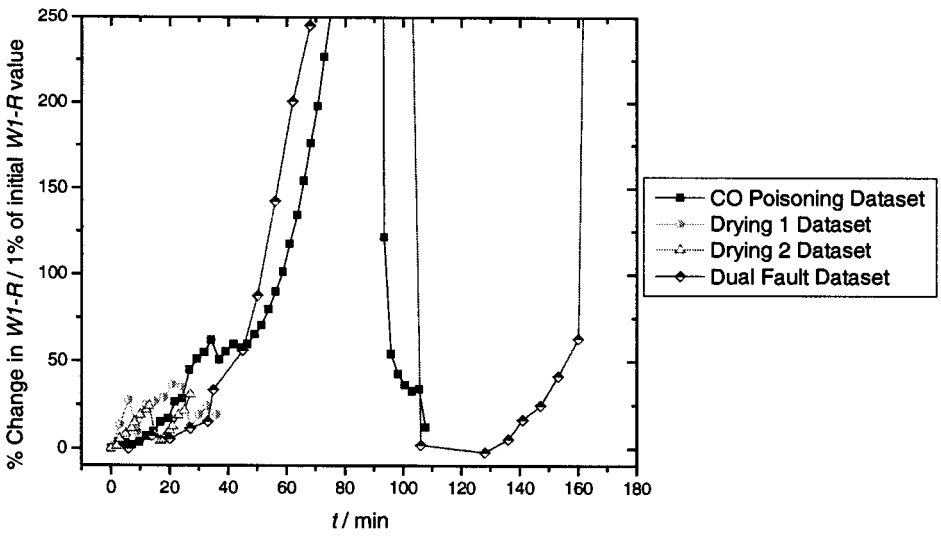

Figure 5.21: Percent Change in Warburg R (*W1-R*) Parameter Values (Figure 5.1) from Normal Conditions as a Function of Time for CO Poisoning, Drying 1, Drying 2, and Dual Fault Datasets, Partial Scale.

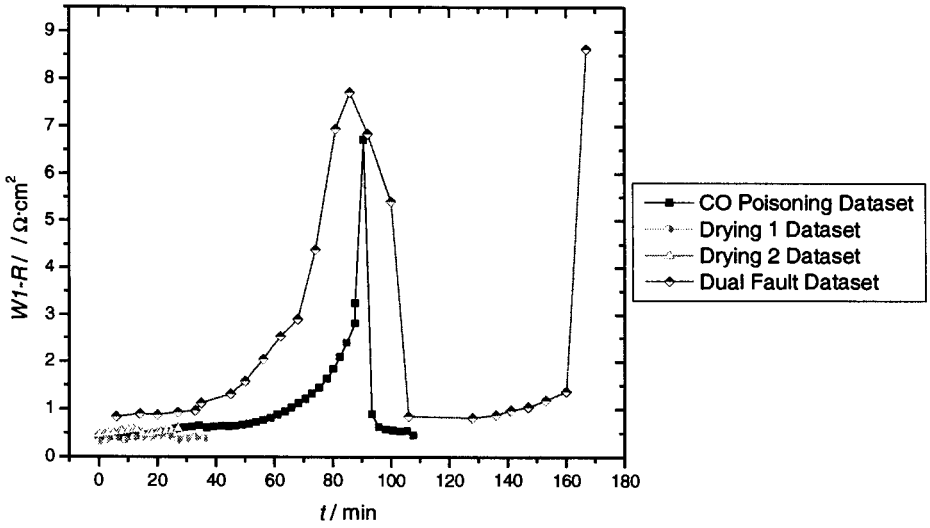

Figure 5.22: Warburg R Parameter (*W1-R*) Values (Figure 5.1) as a Function of Time for CO Poisoning, Drying 1, Drying 2, and Dual Fault Datasets, Full Scale.

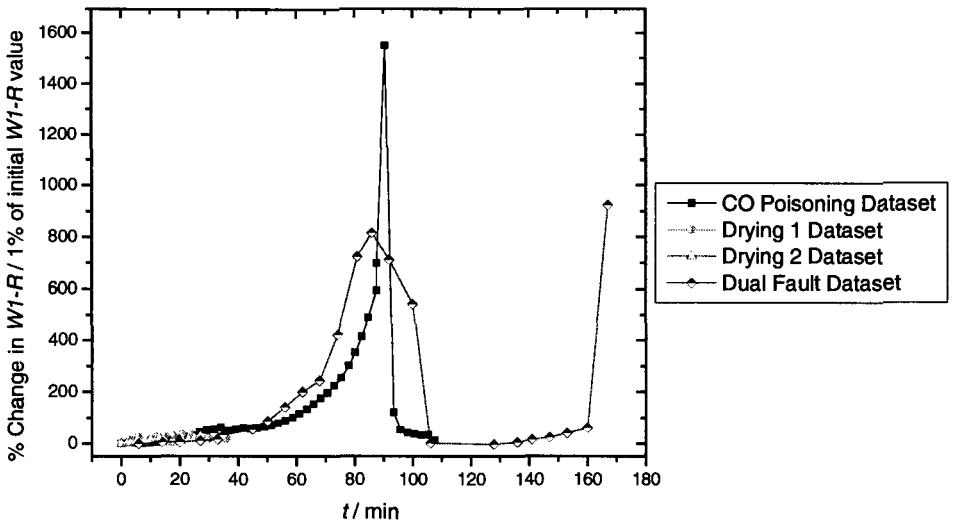

Figure 5.23: Percent Change in Warburg R (*W1-R*) Parameter Values (Figure 5.1) from Normal Conditions as a Function of Time for CO Poisoning, Drying 1, Drying 2, and Dual Fault Datasets, Full Scale.

The Warburg Element *R* parameter is the parameter that affects the width (effective resistance) of the semicircle that it is used to express. It is discussed in Section 2.2.1.4.2. For the CO poisoning dataset this parameter increases substantially as the voltage decreases while for the Drying 1 and Drying 2 datasets, this parameter does increase as the voltage decreases, but not to the same degree as it does with CO poisoning (Figure 5.19-Figure 5.23). The average fitting errors for the Warburg *R* parameters are 5.5% for Drying 1, 7.6 % for Drying 2, and 3.3% for CO poisoning datasets respectively. A change in the Warburg parameter with CO poisoning was not directly expected because the Warburg impedance represents only diffusion. However, coupling between the diffusion and electrochemical phenomena is subtle and might lead to the observed dependence of the Warburg parameter on CO poisoning..

The Warburg R parameter increases as the voltage decreases for both the CO poisoning and the drying sequences. The Warburg *R* parameter increases during flooding conditions (Figure 5.19).

For the dual fault dataset, increases in the Warburg *R* parameter are quite consistent with the Drying 1, Drying 2, and CO Poisoning for the respective fault conditions: 1000% for

CO poisoning and 30% for drying. There is a high (>10^6 %) fitting error for the dual fault dataset points: t =60, 65, 70, 75,85, and 165 min. At these 6 points the average fitting error for this parameter is 3000% while the average fitting error for this parameter for all other times is 2.5%. This Warburg R parameter is likely somewhat sensitive to transient behaviour.

5.3.2.2 Warburg φ Parameter

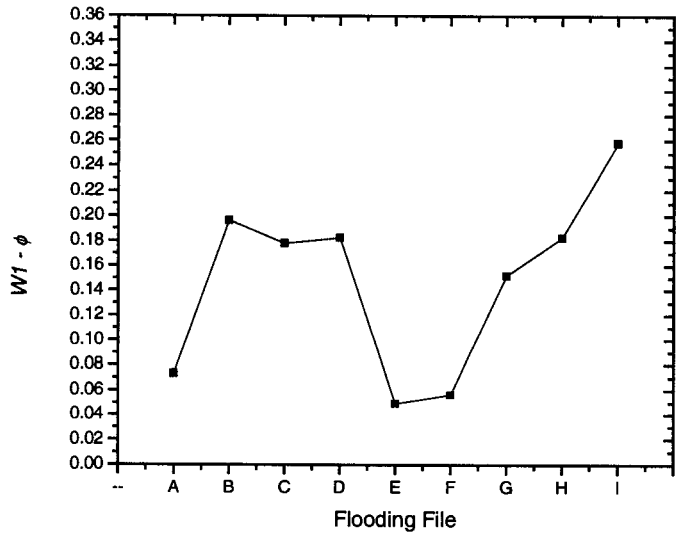

Figure 5.24: Warburg φ Parameter (*W1- φ*) Values (Figure 5.1) for Flooding Dataset.

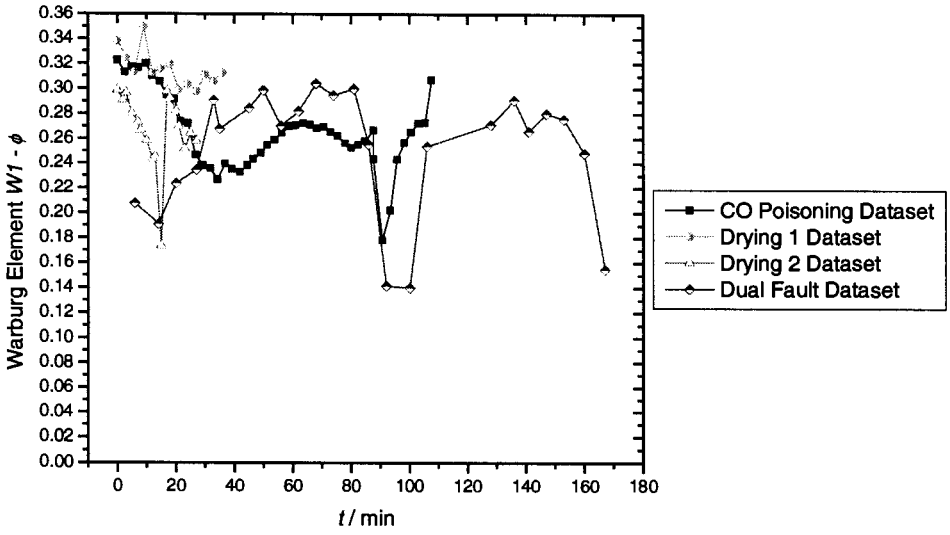

Figure 5.25: Warburg φ Parameter (*W1- φ*) Values (Figure 5.1) as a Function of Time for CO Poisoning, Drying 1, Drying 2, and Dual Fault Datasets.

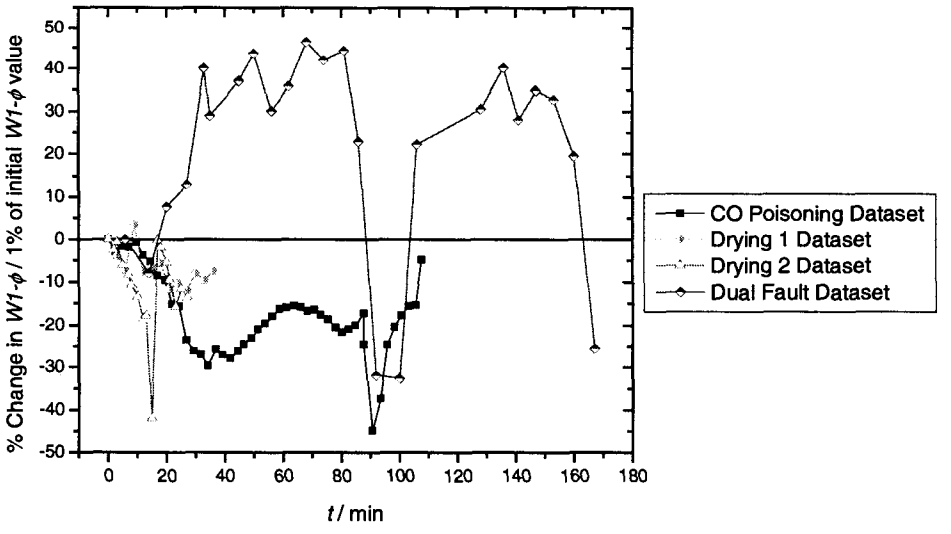

Figure 5.26: Percent Change in Warburg φ (*W1- φ*) Parameter Values (Figure 5.1) from Normal Conditions as a Function of Time for CO Poisoning, Drying 1, Drying 2, and Dual Fault Datasets.

The Warburg φ parameter does not track as strongly with the voltage as other parameters do (Figure 5.24-Figure 5.26). The Drying 2 dataset Warburg φ parameter decreases as the voltage decreases due to the fault. The Drying 1 dataset Warburg φ parameter does not track as clearly, nor does the CO poisoning dataset Warburg φ parameter. There is a large jump in the Warburg φ parameter in each of the datasets at the point where the fault stops and recovery begins. The average fitting errors, for the Warburg φ parameter, are 6.6 % for Drying 1, 16.8% for Drying 2, and 2.0 % for CO Poisoning datasets respectively. The Warburg φ parameter does correlate with flooding behaviour (Figure 5.24).

The Warburg φ parameter does not substantially change with time or with decreases in voltage for the dual fault dataset. There are spikes at the recovery points from drying and CO poisoning, indicating a sensitivity to transience, as with many other parameters. The average fitting error for the Warburg φ parameter is 8.4% for the dual fault dataset.

For a Warburg element to be descriptive of the impedance of diffusion, the φ parameter needs to be approximately 0.5. For this model the Warburg φ parameter is closer to 0.3, indicating that it is likely not directly associated with diffusion. One explanation for this is the limited frequency range used for fitting with this models, we suspect that the

Warburg impedance affects the 1 kHz – 5 Hz frequency range but we are only using the model to fit in the 50Hz-50kHz range because it cannot resolve the third impedance feature, it is likely that the Warburg impedance plays a role in the low frequency behavior and so, in limiting the frequency range of the fit, the ability to completely resolve the Warburg impedance is diminished.

5.3.2.3 Warburg T Parameter

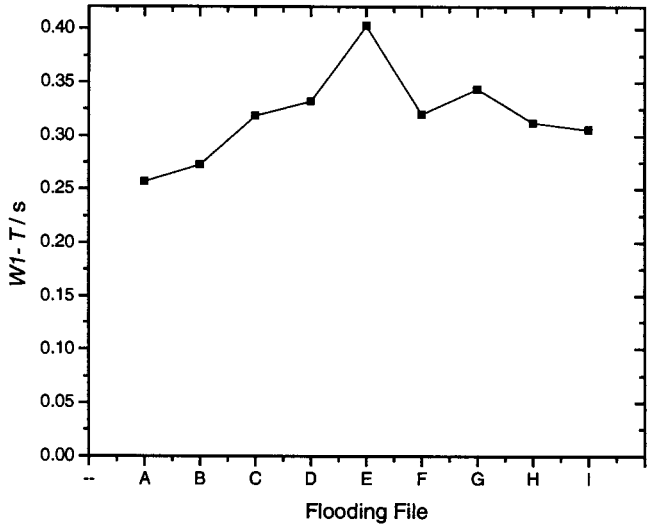

Figure 5.27: Warburg T Parameter (*W1-T*) Values (Figure 5.1) for Flooding Dataset.

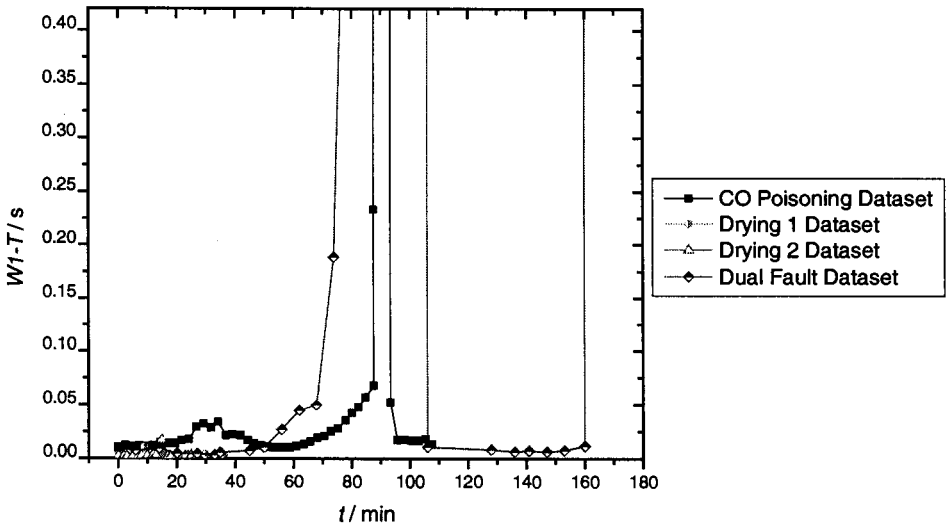

Figure 5.28: Warburg T Parameter (*W1-T*) Values (Figure 5.1) as a Function of Time for CO Poisoning, Drying 1, Drying 2, and Dual Fault Datasets, Partial Scale.

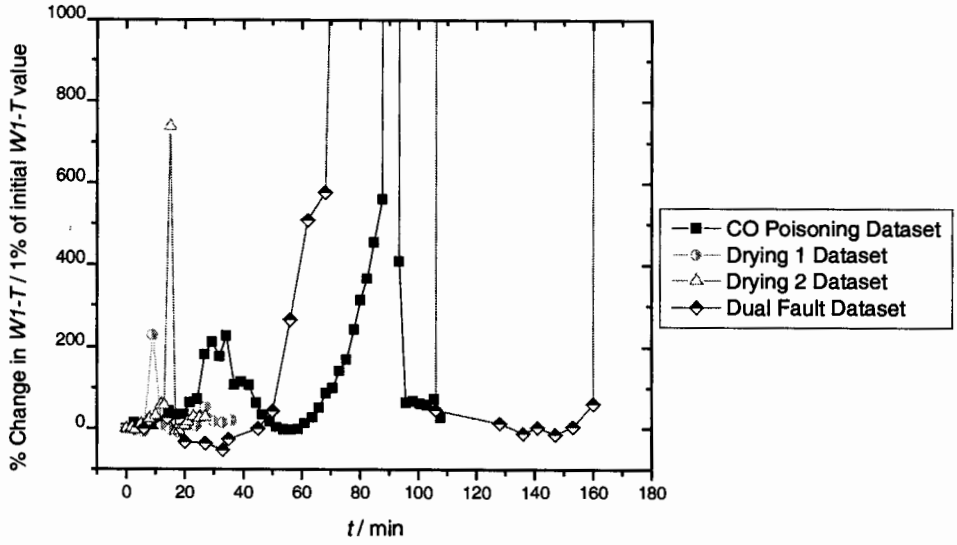

Figure 5.29: Percent Change in Warburg T (*W1-T*) Parameter Values (Figure 5.1) from Normal Conditions as a Function of Time for CO Poisoning, Drying 1, Drying 2, and Dual Fault Datasets, Partial Scale.

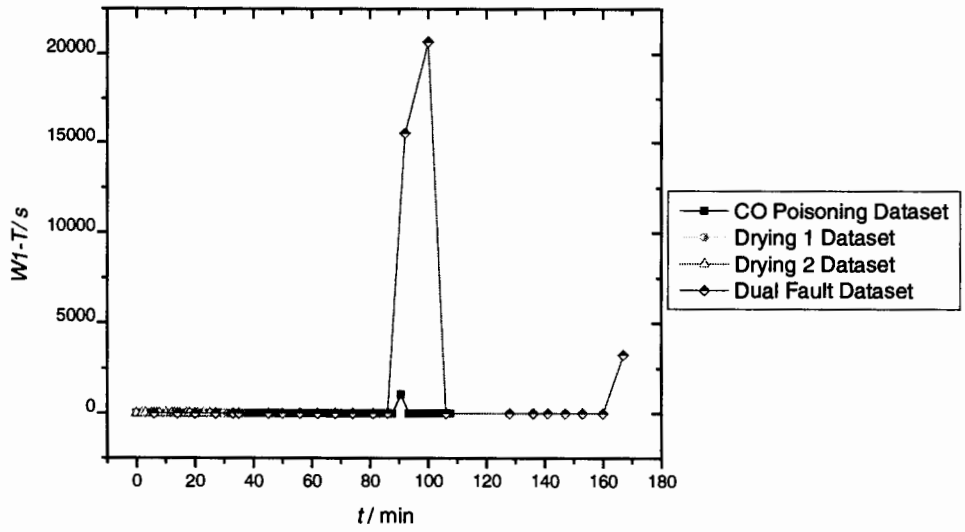

Figure 5.30: Warburg T Parameter (*W1-T*) Values (Figure 5.1) as a Function of Time for CO Poisoning, Drying 1, Drying 2, and Dual Fault Datasets, Full Scale.

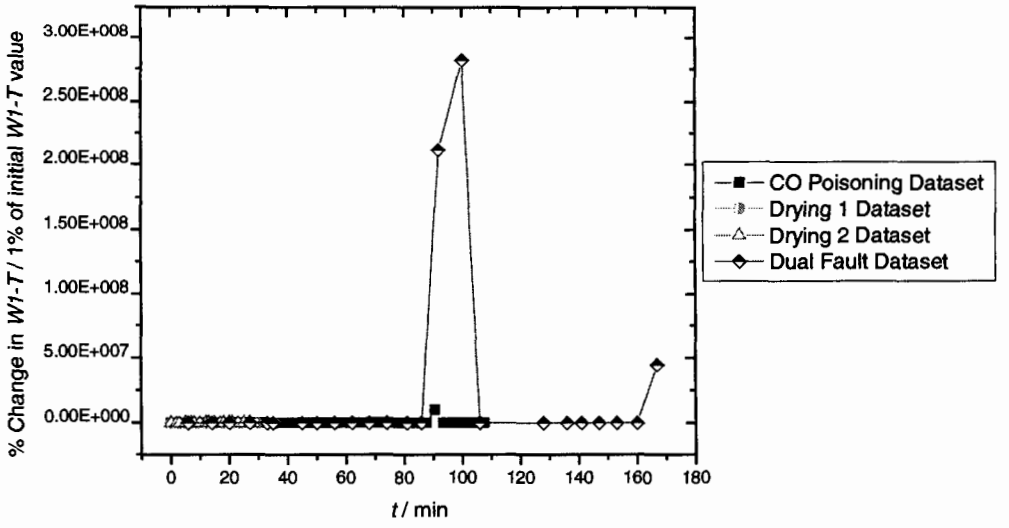

Figure 5.31: Percent Change in Warburg T (*W1-T*) Parameter Values (Figure 5.1) from Normal Conditions as a Function of Time for CO Poisoning, Drying 1, Drying 2, and Dual Fault Datasets, Full Scale.

For both drying and CO poisoning, the Warburg T parameter increases as the voltage decreases with faults. For the CO poisoning dataset and Drying 2 dataset there is a sharp increase in the value of the Warburg T parameter when the fuel cell recovers. This parameter appears to be highly sensitive to the transience of impedance diagrams taken during recovery from faults. The average fitting errors, for the Warburg T parameter, are 15.7% for Drying 1, 72.2% for Drying 2, and 15.1% for CO Poisoning (ignoring the CO Poisoning error of $>10^7$% at t =90 min) respectively.

The Warburg T parameter does not significantly change with the decrease in voltage due to drying for the dual fault dataset. This follows the behaviour of the drying datasets. The CO poisoning sequence in the dual fault dataset behaves similarly to the CO poisoning dataset with respect to the Warburg T parameter; it increases as the voltage decreases. Again, as with other parameters there is a spike for impedance files acquired during recovery from faults. The average fitting error for the Warburg T parameter for the dual fault dataset is 9.1×10^6 % overall, and 29.1% excluding the data points from fault recovery spectra.

5.3.3 Dataset Comparison Conclusions

Initial conclusions drawn from equivalent circuit fitting would indicate that a drying fault can be characterized by an increase in the Warburg *R*, and Warburg *T* parameters, a strong increase in the *R2* resistance, and a decrease in the *R1* and *C1* parameters. A CO poisoning fault can be characterized by an increase in the *R1, R2*, and Warburg *T* parameters, a strong increase in the Warburg R parameter, and a decrease in the *C1* parameter. CO poisoning and drying faults could be differentiated from one another by examining the *R2* and Warburg *R* parameter behaviour. This is illustrated in Figure 5.32 where there are *R2* and Warburg *R* intercepting area for both CO poisoning and drying. It should be noted that in this figure the points labeled CO poisoning in the drying region are in fact from the drying component of the dual fault dataset.

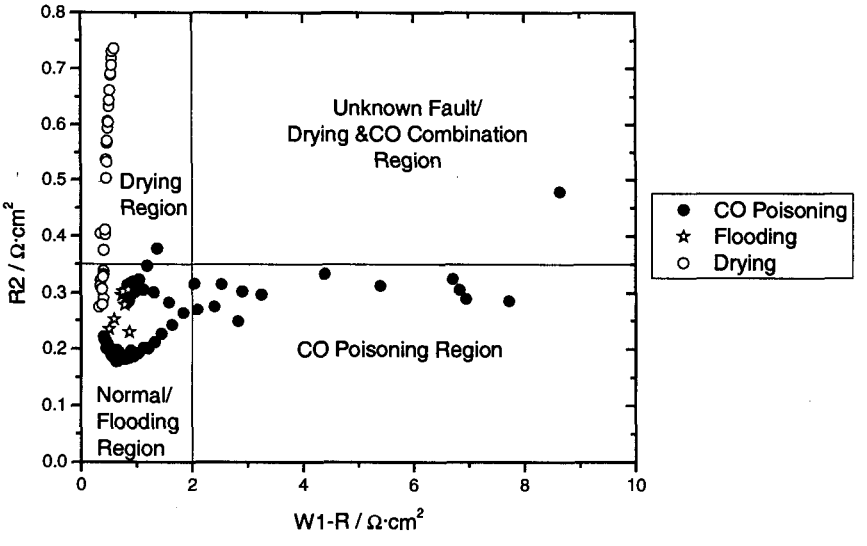

Figure 5.32: R2 parameter vs. Warburg R to show fault regions.

There is a high level of fitting error when using this equivalent circuit to fit impedance data acquired during recovery from faults (re-hydration after drying and air bleed after CO poisoning). This is likely because, for the acquisition of the impedance diagrams that the equivalent circuit model fits well, everything is changing very slowly and for the duration of acquisition is essentially at steady state. During recovery from fault conditions this is not true and there is a high level of transience during impedance acquisition,

causing fittings with the equivalent circuit model to be less accurate particularly at lower frequencies. In an integrated diagnostic device this fitting problem could cause false positive readings for faults due to high levels of error in parameters. Alternatively, high levels of error in fitting parameters could be used to diagnose highly transient conditions in fuel cells.

Many of the equivalent circuit parameters change in a statistically significant manner as the voltage decreases due to CO poisoning and drying faults. There are indications that the rate of increase of parameters such as *R2* and Warburg R could be used to differentiate between CO poisoning and drying fault conditions. A problem with this type of identification could be the possible effects of the rate and severity of performance deterioration due to individual CO poisoning or drying events. Further study of drying and CO poisoning events with differing rates and severity, with all other conditions maintained constant, could help to solve this problem.

There is also concern about the fitting error. Equivalent circuit fitting using a CNLS algorithm is very sensitive to starting parameters. When fitting the dual fault dataset it was fit both in a scaled and un-scaled form. The results of these fittings were different trends in parameters, essentially parameters which would not scale to be equivalent. This is likely due to different initial parameters. Equivalent circuit fitting is also very sensitive to transient conditions. It does not converge well for recovery datasets taken during air bleed events during CO poisoning or re-hydration events during drying.

Information about fault status in fuel cells could be achieved using equivalent circuit fitting with this model. This would likely be more appropriate for use in an off-board setting as many frequencies need to be measured and there are often several iterations required to converge to a "good fit". Problems with unreliable fitting in transient conditions could lead to false fault identification or identification of incorrect faults, leading to incorrect response in an onboard control type setting, whereas in an off-board setting they could be more easily used to identify transient conditions in the cell.

One of the advantages of equivalent circuit fitting is that information about fuel cell material properties such as membrane resistivity, membrane dielectric permittivity, and double-layer capacitance can be identified from model parameters. A better understanding of the effects of a variety of fuel cell operating conditions could be used not only as a diagnostic tool, but also as a basis for fuel cell and membrane design improvement.

6 Single Frequency Analysis – First Circle and Drying

Initially work was done, pursuant to equivalent circuit subtraction work (Section 4.3), to identify the properties of the first semicircle of the impedance (particularly the resistance) by following a single frequency. This work is also described in Ref. 3. The focus was on the identification of drying conditions by monitoring a single frequency. The intent was to develop fault condition cutoff points which could be used as either a part of a control system to initiate humidification or as a safety device to shut down fuel cells prior to membrane burn-through failure. The effect of noise and the possibility of false positive drying fault identification were also investigated. Because much of this work required a baseline for comparison, a variety of impedance spectra with similar conditions were examined and averaged into "baseline data". It should be noted that this baseline was developed for comparative purposes only and does not necessarily reflect the "normal operating conditions" of a fuel cell. To set actual cutoff points and for a better understanding of the issue of noise, real baseline data would be needed.

6.1.1 First Circle RC Algorithm

A geometric algorithm was developed to estimate the electrolyte membrane resistance from measured impedance data at frequencies above 1 kHz (the first semicircle impedance feature). This algorithm uses the idea that the diameter of a semicircle, centered on the horizontal axis and passing through the origin, can be determined geometrically if the coordinates of a point on the arc are known (Figure 6.1).

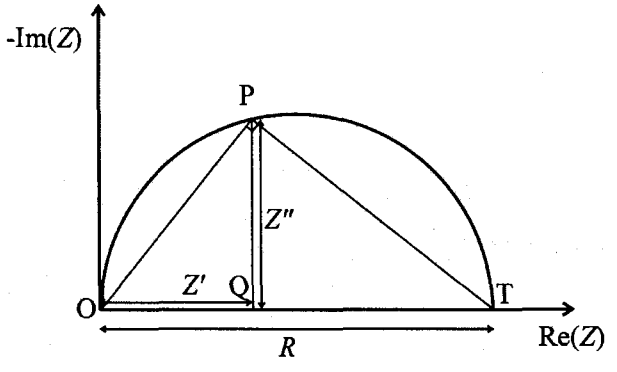

Figure 6.1: Semicircle geometry used for drying fault algorithm

For a semicircle impedance signature the parallel resistance value is the diameter of the semicircle. Using the experimental real and imaginary impedance values (Z' and Z'') at a given frequency (point P), the resistance (R) and capacitance (C) values for that signature can be estimated by noting that triangles OPT and OQP in figure 1 are similar, so that:

$$R = \frac{(Z')^2 + (Z'')^2}{Z'}$$

Eq 6-1

and

$$C = \frac{1}{2\pi \cdot f_{top} R}$$

Eq 6-2

where f_{top} is the frequency at the center of the circle.

Although the capacitance can also track drying it is not as useful as the resistance for several reasons: the additional parameter f_{top} required to calculate the capacitance is only known approximately, and the percent increases of capacitance with drying are not as high (a little less than 50 % of the resistance values).

6.2 Frequency Choice

To create a simple, effective on-board device, the optimal single frequency needs to be chosen to identify the drying fault. The drying effect can be seen in the first semicircle feature on the Nyquist impedance plot. This is in the 1 kHz and above frequency region (Figure 6.2).

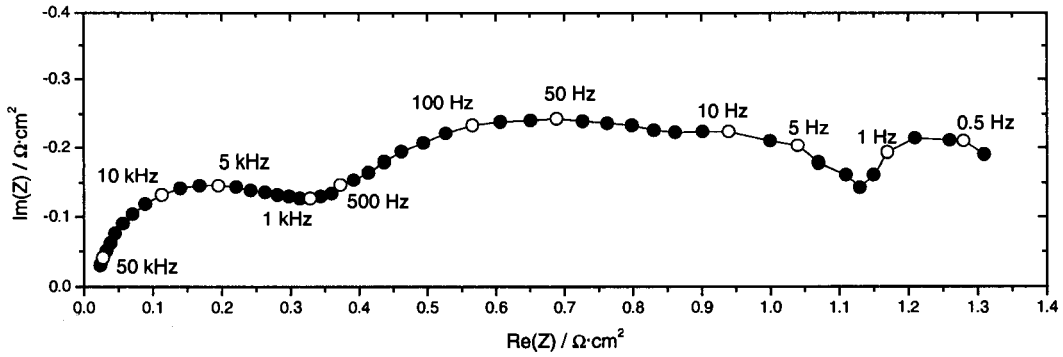

Figure 6.2: Typical impedance spectra (Section 3.3) with Frequencies Identified

In order to choose the optimal frequency to follow to identify drying faults, measured frequencies in the 1 kHz to 100 kHz region were examined. For spectra that were not acquired to 100 kHz the highest frequency measured was used as the upper limit. Frequencies below 1 kHz were not examined because they are heavily affected by second feature; this is beyond the limits of the algorithm used and can lead to mistakes in identification.

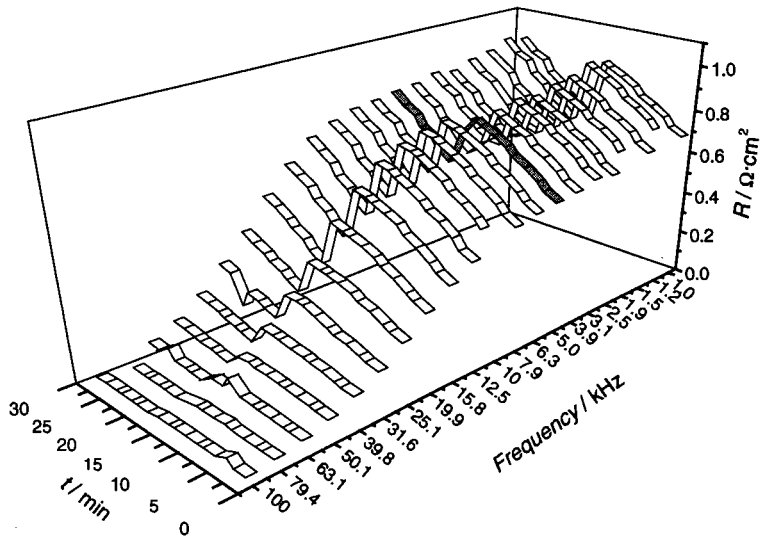

Figure 6.3: Change in membrane resistance, as estimated with the drying algorithm at individual frequencies, over time, gray bar at 5.0 kHz (Figure 3.10).

Figure 6.3 illustrates the change in resistance over time over a frequency range. It shows that frequencies in the 1.2 kHz to 12 kHz range follow drying behavior well, while at higher frequencies there is a steep drop in the magnitude of the estimated resistance. The 1.2 kHz to 12 kHz frequency range is also a logical choice because it is close to the top of the semicircle, an advantage with the drying algorithm. A frequency of 5 kHz, the gray bar on Figure 6.3, was chosen because of the magnitude of the increase of estimated membrane resistance over time was significant compared to higher frequencies, and because of concerns regarding feature overlap for lower frequencies.

6.3 Statistical Significance

In order to positively identify a drying fault, the change in estimated resistance needs to be statistically significant compared to normal operating conditions. This means that the normal variation in resistance during operation needs to be much lower than the variation with drying.

The noise level in measured data is also important in determining the statistical significance of the identification of the drying fault. The effect of noise, and the maximum level of noise acceptable for the drying fault to be identified, has been examined and is discussed below.

The statistical significance of the cutoff limit for drying in a variety of fuel cells needs to be examined. It is not yet known if the membrane resistance that signifies "dry" conditions is consistent between fuel cells.

6.3.1 Hypothetical Baseline

In order to create a hypothetical baseline, several spectra acquired at the conditions listed below in the range of current densities of j = 0.05 to 0.5 A.cm^2 were examined. The typical normal operating conditions for the 4-cell stack or the single cell test assembly are defined as follows:

- $p_{fuel} = p_{oxidant} = 30$ psig,
- $T_{cell} = 65$ °C, $T_{fuel} = 85$ °C, $T_{oxidant} = 70$ °C.

Using the first-circle algorithm to determine the resistance on "normal operation" data gives average estimated resistivity of 0.25 $\Omega.cm^2$ per cell. The average variation in normal conditions is about 15%.

6.3.2 Variation Due to Drying

Five sets of drying data were analyzed, with a focus on the Drying1 and Drying 2 datasets, to determine the degree of increase in the estimated membrane resistance with drying. From this analysis it was determined that, estimating the resistance at a frequency of 5 kHz, an increase of 50 % or more from a standard resistivity of 0.25 $\Omega \cdot cm^2$ can consistently indicate reversible drying, but drying can proceed to an increase of 150% or more without incurring failure or irreversibility (Figure 6.4-Figure 6.5).

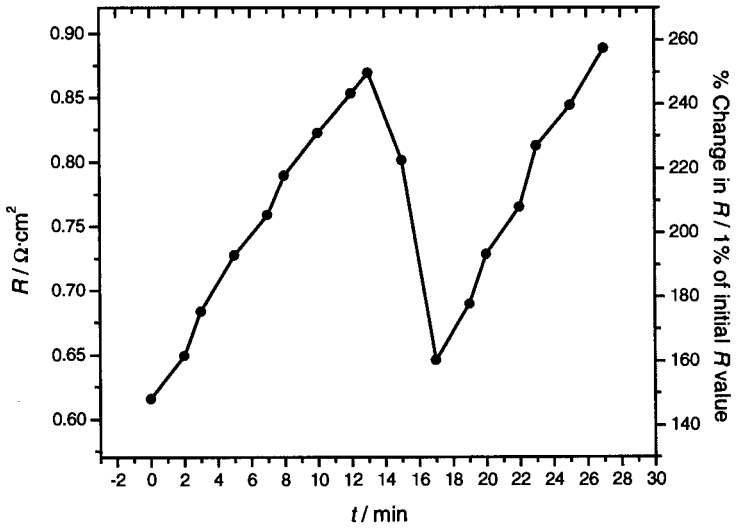

Figure 6.4: Estimated membrane resistance (left) and percent increase in resistance above 0.25 $\Omega.cm^2$ (right) with time (Drying 2 Dataset – Section 3.4.2).

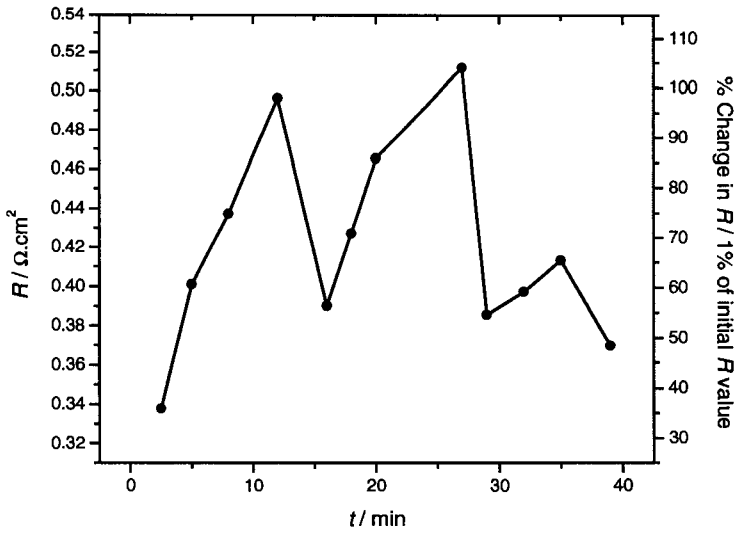

Figure 6.5: Estimated membrane resistance (left) and percent increase in resistance above 0.25 $\Omega.cm^2$ (right) with time (Drying 2 Dataset – Section 3.4.1).

Following the estimated membrane resistance gives a consistent indication of drying. For this data 0.5 $\Omega \cdot cm^2$ per cell, 100% above normal, would be an appropriate arbitrary cutoff to indicate a drying fault in a fuel cell. For a control device 0.375 $\Omega \cdot cm^2$ per cell, 50% above normal, would be a good warning point to rectify temperature or humidification problems.

The choice of cutoff to determine a drying fault could either be an arbitrary resistivity per cell or (as above) a percentage above the normal operating resistivity. This choice would depend on whether all fuel cells have the same characteristic resistivity per cell or if it changes from stack to stack. If all fuel cells have the same characteristic resistivity and change of resistivity with drying, then an arbitrary cutoff value scaled to stack size would be an effective technique. If all fuel cell stacks have different resistivity and drying characteristics then a sampling needs to be taken of individual or batches of stacks at normal operating conditions and a percentage increase above normal for that stack would be a better choice. In order to determine which method is preferable, tests need to be performed on different stacks to determine manufacturing or type variations in the measured membrane resistance.

Assuming the limits of a 50% increase as a warning, a 100% increase as a failure, and a a single cell drying, the warning would show up as an increase in the overall stack resistance of 12.5% in a 4 cell stack, 2.5% in a 20 cell stack and 0.5% in a 100 cell stack. The failure would show up as in increase in the overall stack resistance of 25% for a 4 cell stack, 5% for a 20 cell stack, and 1% for a 100 cell stack.

6.3.3 Noise

This technique was designed with a final device, likely be a part of an onboard diagnostics system, in mind. In that type of location noise levels are likely to be much higher than those experienced in laboratory experiments. Because of this it is necessary to determine the level of noise for experimental data after which this technique will no longer maintain statistical significance. Noise tolerance is also of interest because a smaller AC perturbation for impedance measurement would be preferable in a final device because it would have less of an overall effect on the rest of the system. With smaller amplitude perturbations the measured impedance data is generally noisier.

6.3.3.1 Noise Algorithm

A noise algorithm was developed to transform measured impedance data into "noisy" impedance data. Noise was added at varying levels to the same files to make comparison easier. The noise algorithm added noise randomly at each point to create the effect of random noise in an application.

In order to generate the noise for a given frequency point, the magnitude of the impedance ($|Z|$) at that frequency is multiplied by the "percentage" of noise applied (*%noise*). This is then multiplied by a random number (*nf*); generated in Maple from a normal distribution function with a standard deviation of 1.

$$noise = |Z| \cdot \%noise \cdot nf$$

Eq 6-3

Two noise values are generated for each frequency point and one is added to each the measured real and imaginary impedance values at that frequency.

$$Z'_n = Z' + noise$$

Eq 6-4

and

$$Z''_n = Z'' + noise$$

Eq 6-5

With this algorithm the noise is proportional to the magnitude of the impedance. For our data this means that the noise will be larger at lower frequencies (Figure 6.6) because the magnitude is larger. This makes sense for a variety or reasons including sample time. This method has also been used by Orazem *et al.* for work with noise and impedance data[80].

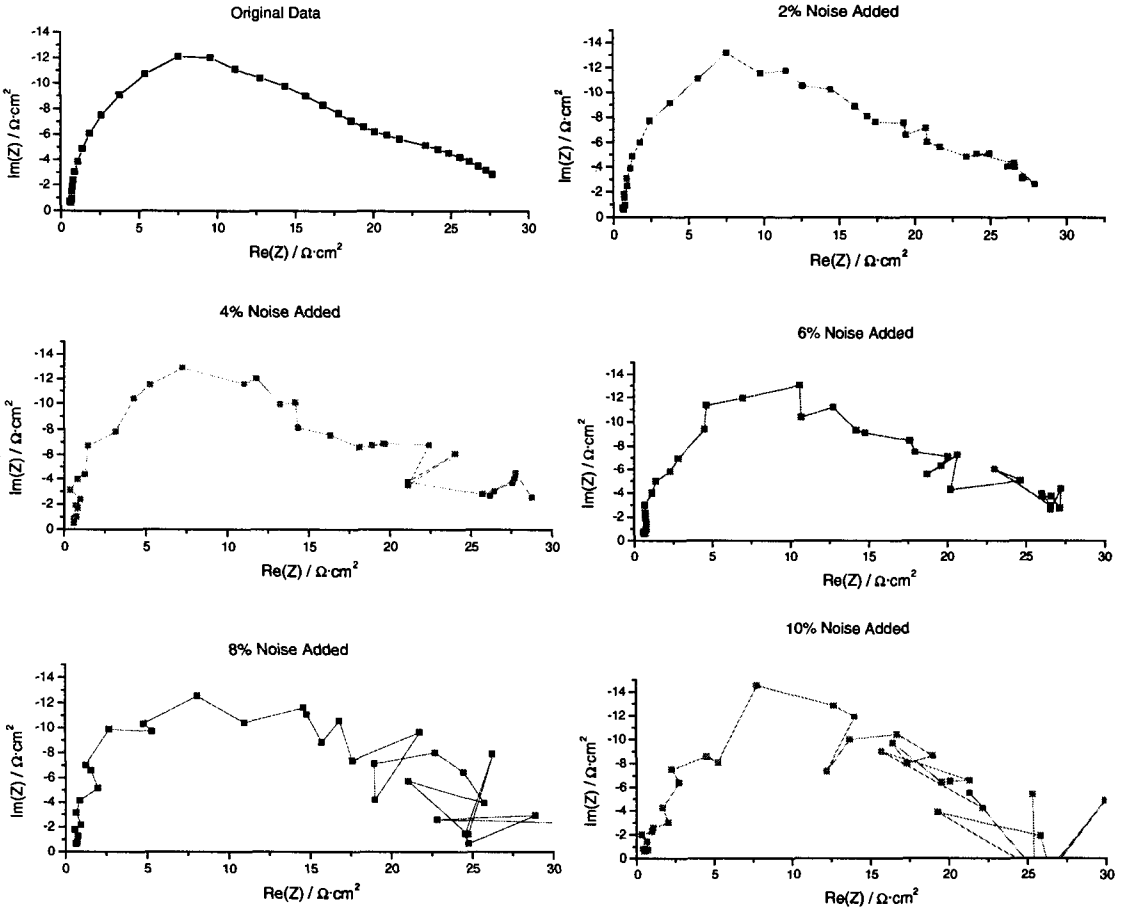

Figure 6.6: Nyquist Plots of data with no noise, 2%, 4%, 6%, 8%, and 10% noise added (Conditions as in Figure 3.10, t = 15 min).

6.3.3.2 Noise Level Threshold

The noise level threshold is the level after which the error due to noise reduces the statistical significance of the technique. To determine the probability of a false positive, the difference (ΔR) between the estimated resistance with noise (R_{noise}) and without ($R_{noinoise}$) was taken for each impedance file in the Drying 2 dataset:

$$\Delta R = R_{nonoise} - R_{noise}$$

Eq 6-6

These differences were then used to determine a mean and standard deviation for the distribution at each noise level.

To determine the probability that a false positive occurs, the distribution was considered to be a normal distribution, consistent with the earlier assumptions in the development of noisy data. The probability of a false positive was taken to be the probability of a resistance above the cutoff resistance.

A 50% to 150% increase in estimated resistance indicates a drying fault. A false positive will occur when the variation due to noise for normal operating conditions reaches this level. The worst-case scenario would be when the normal operating condition is at the top of the 15% variation and the cutoff for a drying fault is at 50% above normal conditions (Figure 6.7:). In this case the 4% noise level would be the cutoff where a false positive only occurs 1 out of 20 times instead of 1 out of 2 times as at 6% noise.

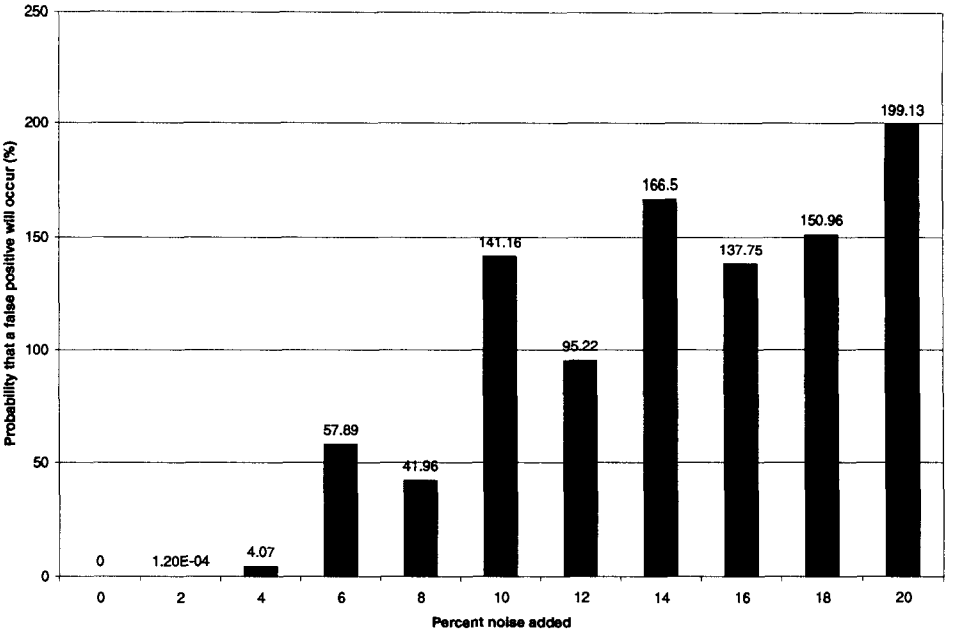

Figure 6.7: Probability that a false positive – (a reading of 0.375 $\Omega \cdot cm^2$) will be achieved with a normal operating resistance of 0.2875 $\Omega \cdot cm^2$ (15% above normal) – varying with noise level

Another scenario examined was when the considering the normal operating condition to be at the top of 15% variation and the cutoff for a drying fault is at 100% above normal conditions (Figure 6.8). In this case the 8% noise level would be the cutoff where a false positive only occurs 7 out of 1000 times instead of 17 out of 100 times as at 12 % noise.

Figure 6.9 and Figure 6.10 illustrate the absolute error in R and the percent deviation from normal conditions with the addition of differing levels of noise respectively.

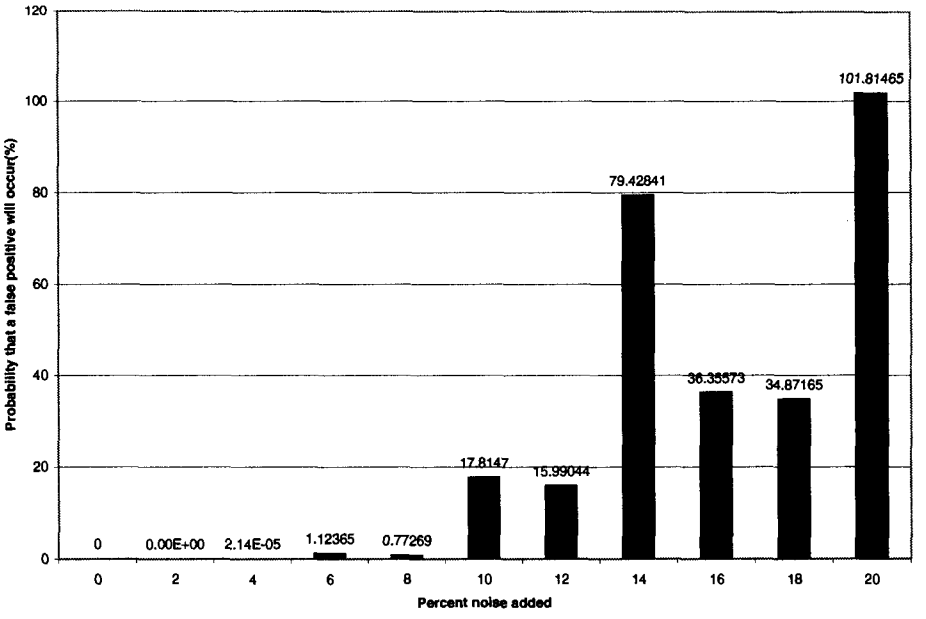

Figure 6.8: Probability that a false positive - a reading of 0.50 $\Omega \cdot cm^2$ will be achieve with a normal operating resistance of 0.2875 $\Omega \cdot cm^2$ (15% above normal) – varying with noise level

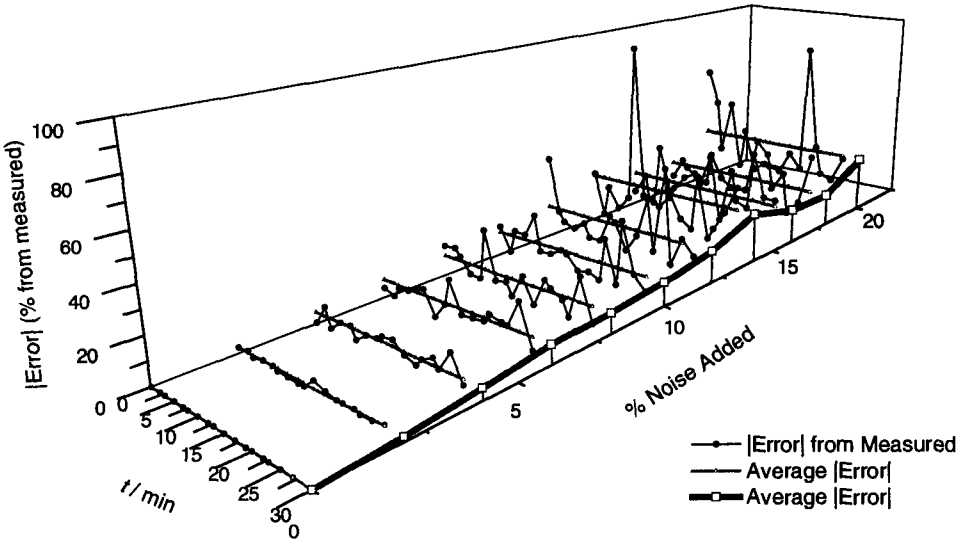

Figure 6.9: Absolute error as a percentage of the estimated resistance values at 5 kHz vs. time and average absolute error with increasing noise levels for Drying 2 Dataset.

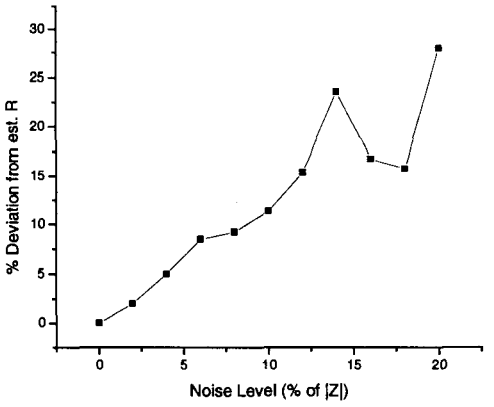

Figure 6.10: The average percent deviation from the estimated resistance vs. noise level for Drying 2 Data.

6.4 Summary

The drying fault can be reliably tracked, over time, by following the real and imaginary components of the fuel cell impedance at 5 kHz, and estimating the membrane resistance. Under the assumption of the hypothetical baseline conditions used, an increase of 50% above normal resistance conditions indicates drying is occurring but increases of 150% or more above normal can be attained without failure for our single cell fuel cell assembly. To make a final decision on the universality of the cutoff resistance and frequency choice, drying data from different fuel cell stacks and manufacturers should be studied. The work with noise suggests that there is a fairly good tolerance for noise with this technique.

This method was pursued with the interest of gaining not only a method to track drying but also a method to track membrane resistivity. It was later found that following individual, un-manipulated, impedance parameters also track with faults. This is discussed further in the following section.

7 Multi Frequency Analysis – All Faults

There is interest in developing techniques for onboard diagnostics and controls of running fuel cells; a device that can quickly identify multiple faults and provide the correct rectification or shut down in severe cases. For this purpose the acquisition and equivalent circuit analysis of full impedance spectra is time consuming and requires complex hardware and software to fit and monitor. The algorithm used for single frequency analysis, though somewhat effective to monitor membrane properties, proved not to be necessary to monitor fault conditions. There were also difficulties in differentiating between drying and CO poisoning faults using a single frequency. Because of this multi-frequency analysis (MFA) was investigated.

MFA, for the purpose of this work, is the monitoring and analysis of the impedance at several individual frequencies to identify individual fault behaviour. This involves measuring the impedance at several frequencies and monitoring to ensure that fault thresholds are not reached. Ideally in an onboard device there would be a fault threshold and a warning threshold, both integrated into the fuel cell control system. If the warning threshold for a known fault is passed then the fuel cell control system could adjust humidification or air bleed in order to rectify the problem. If the fault were to persist to the fault threshold then the fuel cell could be shut down before irreparable damage was done.

In an onboard situation the frequencies chosen would be continuously monitored. For the purposes of this analysis individual frequency data from measured impedance spectra were extracted and compared at each frequency as no hardware to continuously monitor several frequencies was available.

It should be noted that parameter thresholds are not intensively discussed in this section because there are discrepancies between "normal operating conditions" for the fault datasets. These discrepancies are likely due to the differing conditions required to

produce different fault conditions and the fact that impedance spectra were not continuously acquired from an initial hydrated state in the case of the drying faults.

7.1 Frequency choice

There are several factors influencing the choice of frequencies for MFA. Because time of acquisition is important in MFA, higher frequencies are more appealing. Also there are the physical limitations of the measurement device to consider, measurements at too high or too low a frequency can be susceptible to noise or measurement artifacts. The most important factor in choosing the frequencies is that they be able to represent sufficient impedance information to enable the fault conditions to be distinguished (particularly between CO poisoning and Drying).

5 kHz (at the apex of the first semi-circle feature), 500 Hz (between the first and second semicircle features), and 50 Hz (on the start of the second semi-circle feature), were chosen as the three frequencies for the analysis of impedance fault data in this work (Figure 7.1). Three frequencies were chosen because two frequencies were insufficient to represent the impedance data: the spacing of the semicircles, and size of the second semicircle in relation to the first can be identified with three frequencies but not with two.

The three frequencies chosen were shown to give the best distinction between CO poisoning and drying of the 11 frequencies attempted. The real and imaginary parts of the impedance as well as the phase and magnitude for drying and CO poisoning data were compared at 0.5 Hz, 1 Hz, 5 Hz, 10 Hz, 50 Hz, 100 Hz, 500 Hz, 1 kHz, 5 kHz, 10 kHz, and 50 kHz. From this comparison, and pursuant to the single frequency work in Section 6, 5000 Hz, 500 Hz, and 50 Hz were chosen.

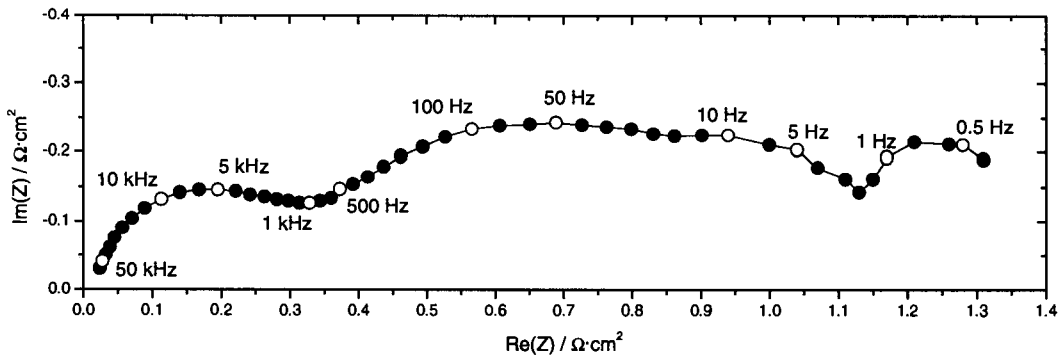

Figure 7.1: Typical impedance spectra (Section 3.3) with Frequencies Identified.

7.2 Parameters of Interest

In MFA there were four primary parameters investigated in this work. The change in the real part, the imaginary part, the phase and the magnitude of the impedance were examined at each of the three frequencies. The magnitude of impedance is relatively simple to measure on its own while the phase, real part, and imaginary part are more difficult to measure. Both the values of each of these parameters and their percent increase from normal operating conditions were considered for fault detection.

In order to set eventual threshold values for each of these parameters, the actual values of parameters would most likely be used. Of note, in this case there is a lack of "normal operating condition" or baseline data to compare all the faults to. This is due to the fact that there is a high level of variation in the spectra taken as "normal operating conditions" in our work. Because of this the percent change in parameters from the "normal operating conditions file", described in Section 3.2, is used to have a better method for comparing changes.

7.2.1 Real Part of the Impedance

Drying (Figure 7.2-Figure 7.7)

The real part of the impedance increases with drying at all three frequencies. For the H_2-air drying sequences (Drying 1 and Drying 2), although the change in value of the real

part of the impedance is different for the three frequencies, the percent increase in Re(Z) remains approximately 40% at each frequency. The drying data acquired with reformate show a similar result except that the percent increase is larger at 50 Hz than at 500 Hz and 5000 Hz. This may be due to incomplete recovery from CO poisoning or could be a characteristic of drying with reformate.

CO Poisoning (Figure 7.2-Figure 7.7)

The real part of the impedance increases with CO poisoning at all three frequencies, but increases more steeply at 500 Hz than at 5000 Hz and even more steeply at 50 Hz than at 500 Hz. The percent change also increases as frequency decreases.

Flooding (Figure 7.8)

The real part of the impedance does not change significantly with flooding in this frequency range.

Variation of Gas Composition (Figure 7.9-Figure 7.11)

The real part of the impedance does not vary significantly at 500 Hz or 5000 Hz with changing gas compositions or current density. At 50 Hz the real part of the impedance is slightly higher for datasets acquired with reformate instead of hydrogen but not in a manner that could be interpreted as statistically significant. The real part of the impedance decreases slightly as current density increases.

Summary

Drying and CO poisoning could be differentiated using the real part of the impedance because drying (both with hydrogen and reformate) shows a larger increase in the real part of the impedance at 5000 Hz than CO poisoning. Drying with hydrogen also maintains a fairly similar percentage increase at all three frequencies (40%). Drying with

the reformate shows a slightly larger percent increase at 50 Hz than at other frequencies, differentiating it somewhat from drying with hydrogen. This is consistent with the gas composition variation results that show Re(Z) with reformate to be higher than Re(Z) with hydrogen at 50 Hz. CO poisoning shows very little increase in Re(Z) at 5000 Hz but has greater increases at 500 Hz and 50 Hz.

If monitoring the real part of the impedance at 5000 Hz, 500 Hz, and 50 Hz, assuming only the 3 fault conditions studied, a voltage drop could be identified as:

1. **Drying**: if there is a consistent percent change in Re(Z) (~50%) with at all three frequencies as voltage decreases with time.

2. **CO Poisoning**: if there are progressively larger percent changes in Re(Z) at 5000 Hz, 500 Hz and 50 Hz as voltage decreases with time.

3. **Flooding**: if there is essentially no change in Re(Z) from normal conditions as voltage decreases with time.

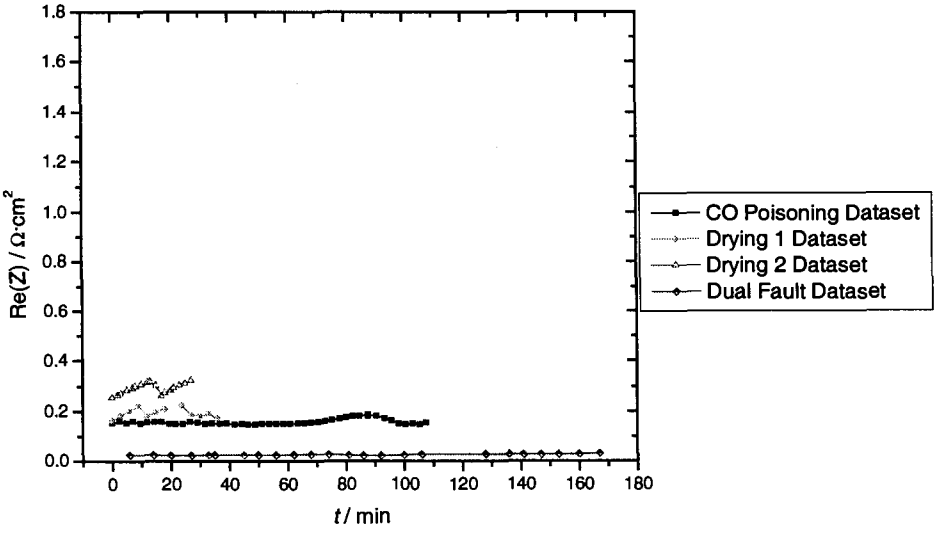

Figure 7.2: Real Part of the Impedance at 5000 Hz vs. Time for CO Poisoning, Drying 1, Drying 2, and Dual Fault Datasets.

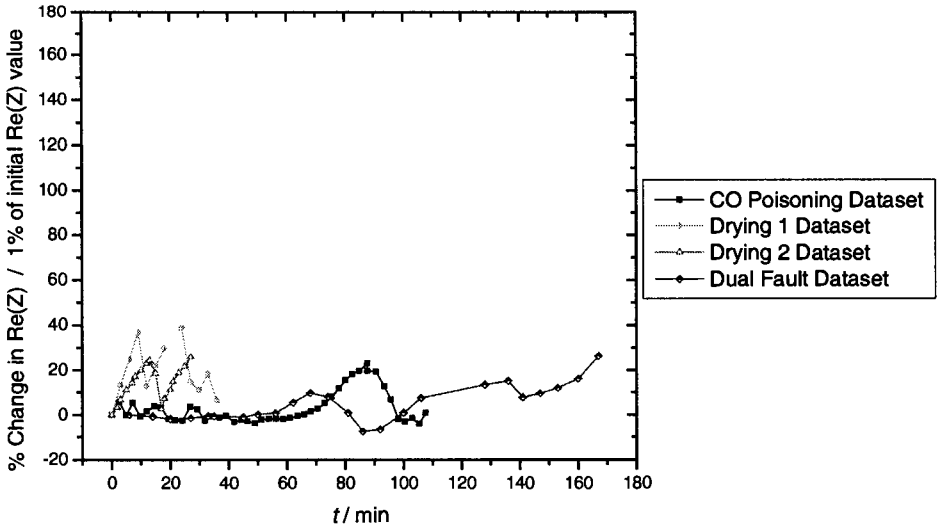

Figure 7.3: Percent Change in the Real Part of the Impedance at 5000 Hz vs. Time for CO Poisoning, Drying 1, Drying 2, and Dual Fault Datasets.

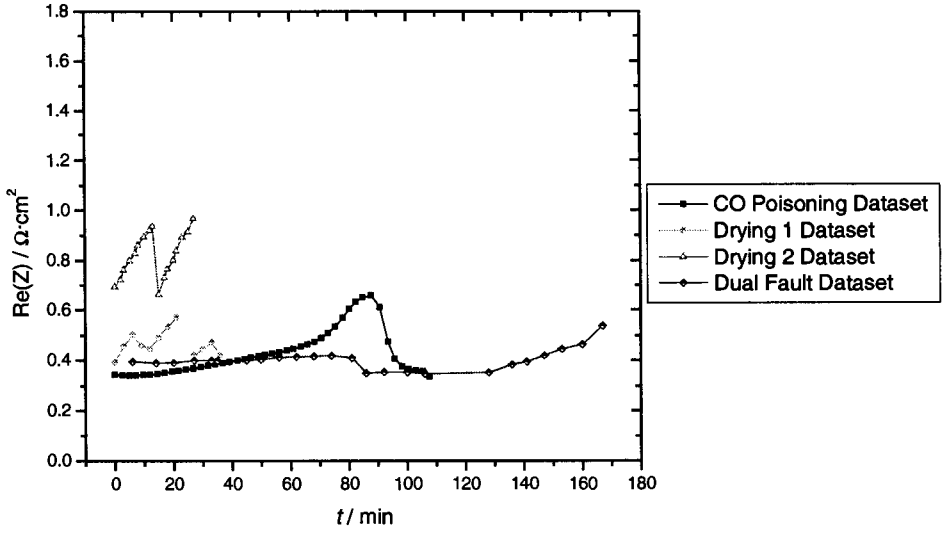

Figure 7.4: Real Part of the Impedance at 500 Hz vs. Time for CO Poisoning, Drying 1, Drying 2, and Dual Fault Datasets.

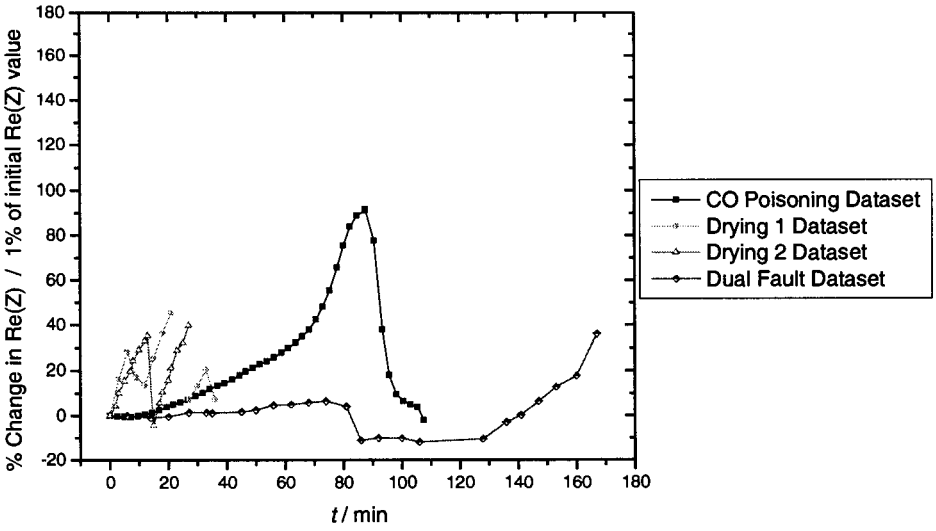

Figure 7.5: Percent Change in the Real Part of the Impedance at 500 Hz vs. Time for CO Poisoning, Drying 1, Drying 2, and Dual Fault Datasets.

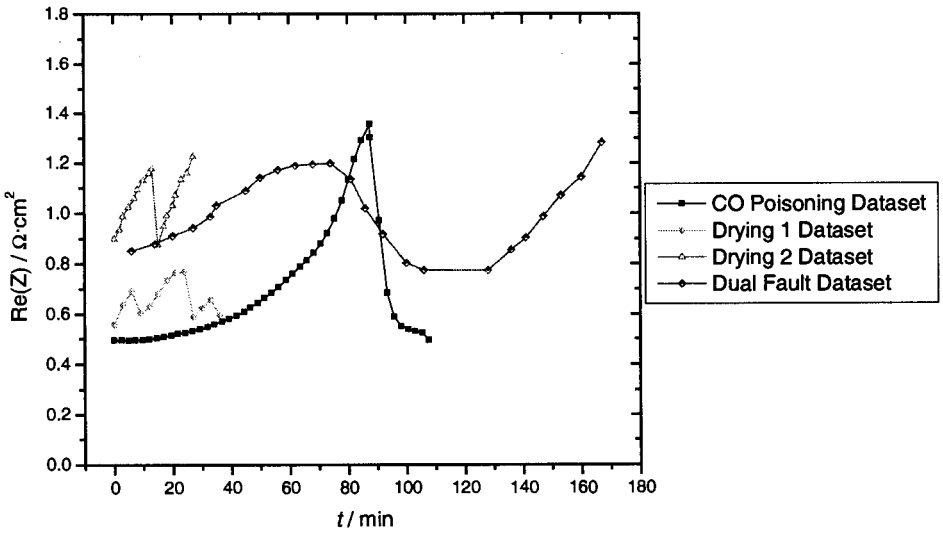

Figure 7.6: Real Part of the Impedance at 50 Hz vs. Time for CO Poisoning, Drying 1, Drying 2, and Dual Fault Datasets.

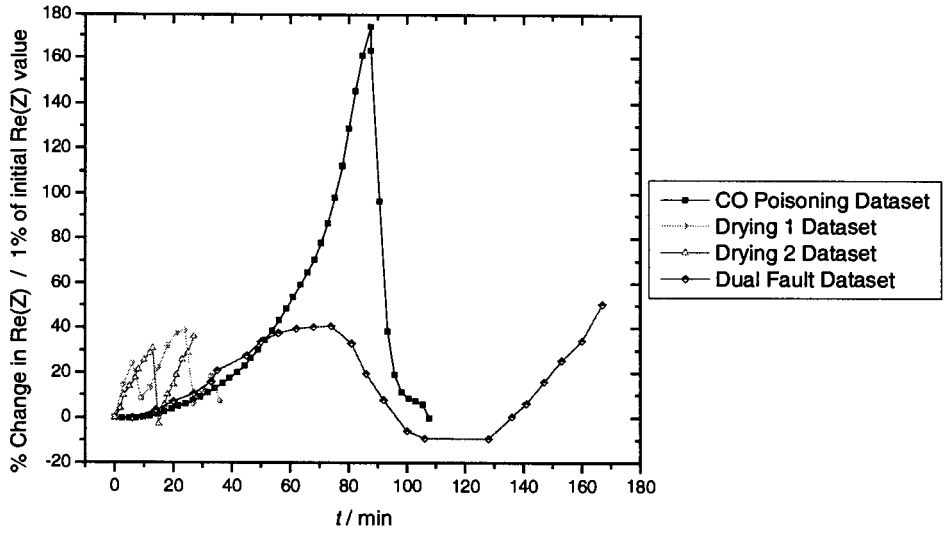

Figure 7.7: Percent Change in the Real Part of the Impedance at 50 Hz vs. Time for CO Poisoning, Drying 1, Drying 2, and Dual Fault Datasets.

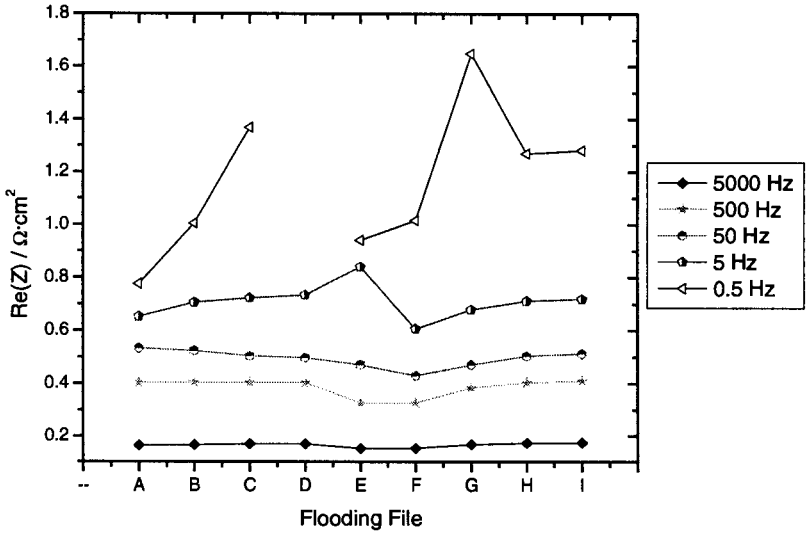

Figure 7.8: Real Part of the Impedance for Flooding Data Files at 5000 Hz, 500 Hz, 50 Hz, 5 Hz, and 0.5 Hz.

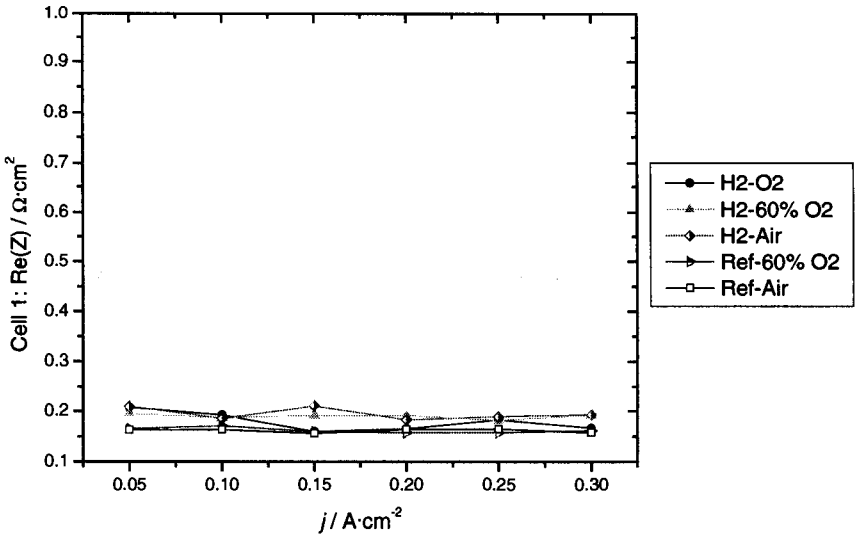

Figure 7.9: Real Part of the Impedance at 5000 Hz vs. Current Density for H_2-O_2, H_2-60% O_2 , H_2-Air, Ref – 60% O_2, and Ref-Air Datasets.

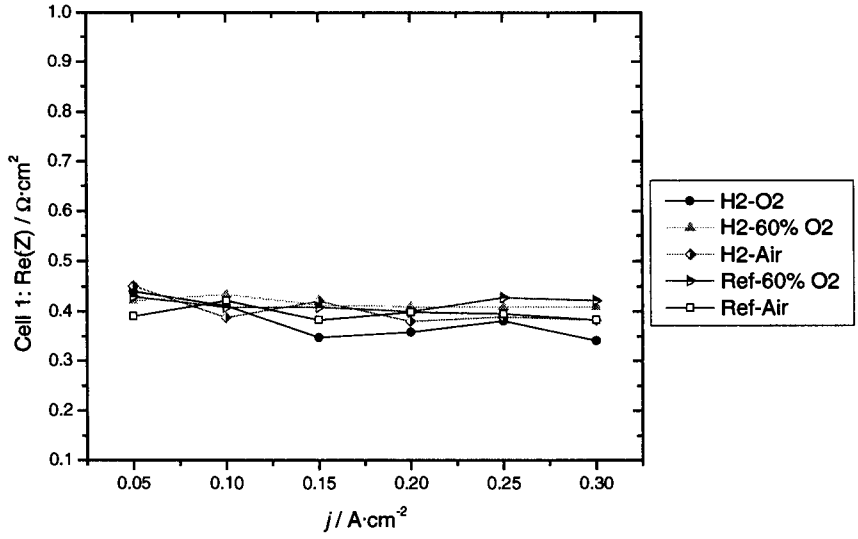

Figure 7.10: Real Part of the Impedance at 500 Hz vs. Current Density for H_2-O_2, H_2-60% O_2 , H_2-Air, Ref – 60% O_2, and Ref-Air Datasets.

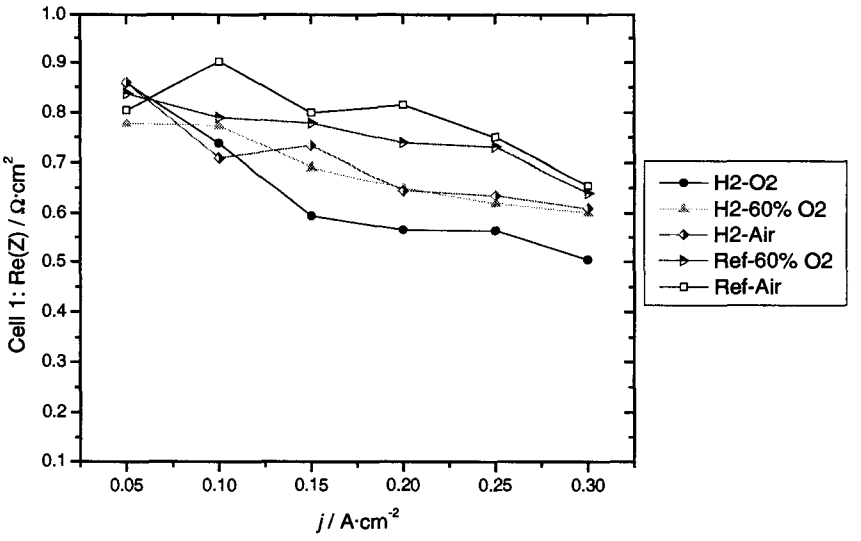

Figure 7.11: Real Part of the Impedance at 50 Hz vs. Current Density for H_2-O_2, H_2-60% O_2, H_2-Air, Ref – 60% O_2, and Ref-Air Datasets.

7.2.2 Imaginary part of the Impedance

Drying (Figure 7.12-Figure 7.17)

For the H_2 –Air datasets, Drying 1 and Drying2, the absolute imaginary part of the impedance increases with drying behaviour at 5000 Hz and 500 Hz and there is little change at 50 Hz. The percent change in the absolute imaginary part of the impedance is approximately 50 % at 5000 Hz, 30% at 500 Hz, and 25% at 50 Hz.

For the dual fault dataset the magnitude of the imaginary part of the impedance increases with CO poisoning behaviour, with greater increases at 500 Hz and 50 Hz than at 5000 Hz. The percent change in the absolute imaginary part of the impedance increases as frequency decreases.

The discrepancy between the behaviour of the imaginary part for the Drying 1 and Drying 2 datasets and the dual fault dataset is probably due to the affect of the reformate. The absolute imaginary part of the impedance at 50 Hz is greater for the reformate air combination (Figure 7.21) than for all the other gas combinations; this could be affecting the drying data behaviour in the dual fault dataset.

CO Poisoning (Figure 7.12-Figure 7.17)

The absolute imaginary part of the impedance increases with CO poisoning. The percent change in the absolute imaginary part of the impedance increases as frequency decreases.

Flooding (Figure 7.18)

The imaginary part of the impedance does not change significantly with flooding at 5000, 500, or 50 Hz. It does however change significantly with flooding behaviour at 0.5 Hz (Figure 7.18).

Variation of Gas Composition (Figure 7.19-Figure 7.21)

At 5000 Hz there is very little variation in the magnitude of the imaginary part of the impedance with gas composition or current density. At 500 Hz the magnitude of the imaginary part of the impedance for datasets acquired with reformate was larger than |Im(Z)| for datasets acquired with hydrogen. There was very little change with current density. At 50 Hz the |Im(Z)| values for the dataset acquired with reformate-air were slightly larger than the others, which were all fairly similar. There was a decrease in |Im(Z)| with increasing current density.

Summary

The imaginary part of the impedance is less useful than the real part of the impedance to differentiate between CO poisoning and drying conditions. It increases with decreasing frequency for drying with hydrogen but not for drying with reformate. Im(Z) decreases with decreasing frequency for CO poisoning and drying with reformate. This makes it difficult to differentiate between the two phenomena using the imaginary part of the impedance.

If monitoring the imaginary part of the impedance at 5000 Hz, 500 Hz, 50 Hz, and 0.5 Hz assuming only the 3 fault conditions studied, a voltage drop could be identified as:

1. **Drying**: if there is a fairly consistent (within 50%) percent change in |Im(Z)| at all three frequencies as voltage decreases with time.

2. **CO Poisoning**: if there are progressively larger percent changes in |Im(Z)| at 5000 Hz, 500 Hz and 50 Hz, with a relatively high percent in crease (>200%) at 50 Hz as voltage decreases with time.

3. **Flooding**: if there is essentially no change in |Im(Z)| from normal conditions at 5000, 500, and 50 Hz, but there are significant changes in |Im(Z)| at 0.5 Hz as voltage decreases with time.

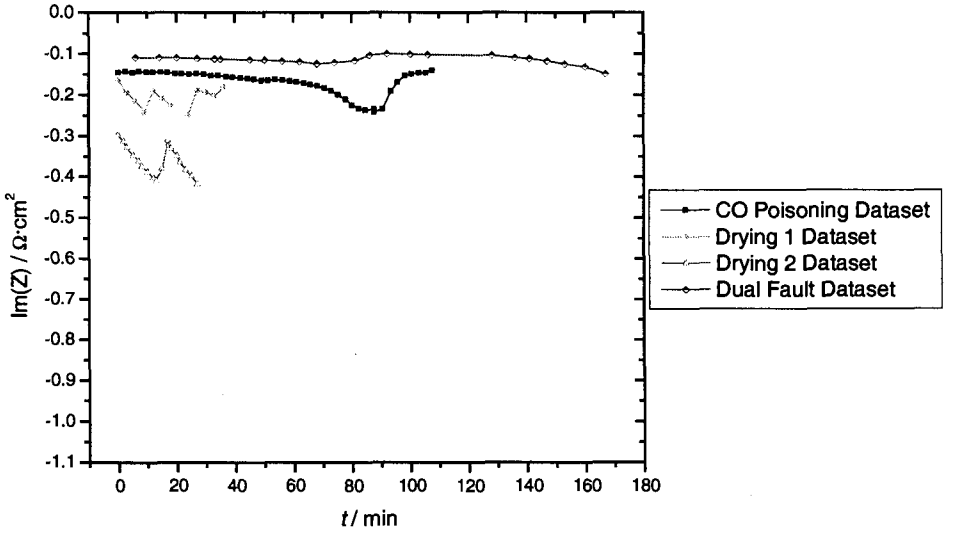

Figure 7.12: Imaginary Part of the Impedance at 5000 Hz vs. Time for CO Poisoning, Drying 1, Drying 2, and Dual Fault Datasets.

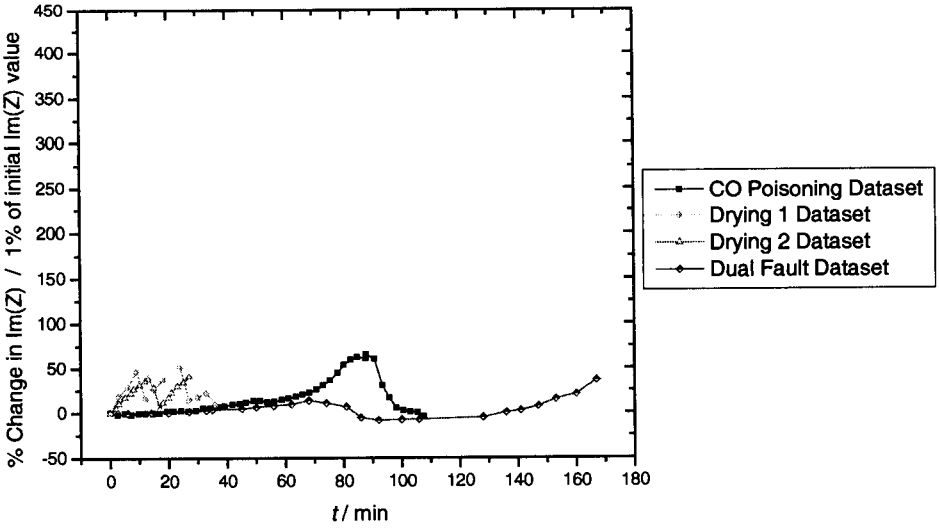

Figure 7.13: Percent Change in the Imaginary Part of the Impedance at 5000 Hz vs. Time for CO Poisoning, Drying 1, Drying 2, and Dual Fault Datasets.

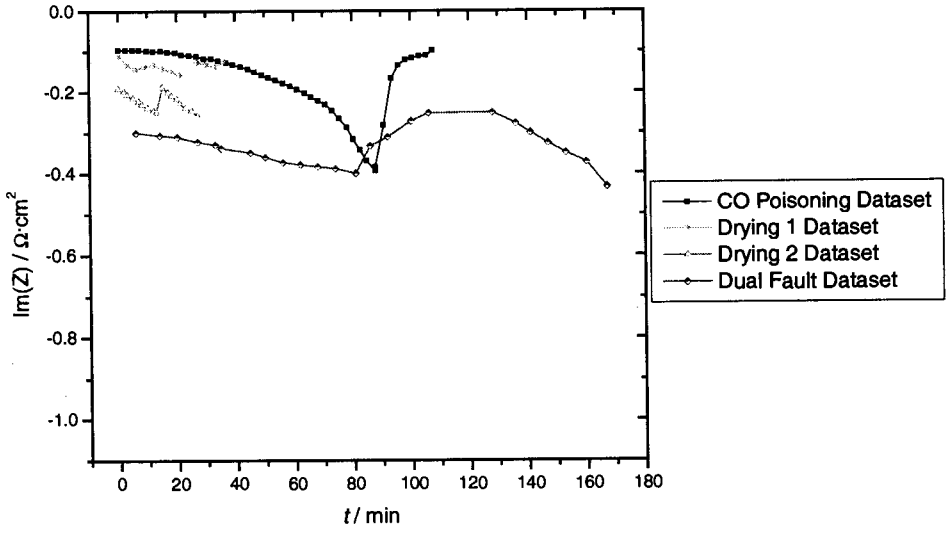

Figure 7.14: Imaginary Part of the Impedance at 500 Hz vs. Time for CO Poisoning, Drying 1, Drying 2, and Dual Fault Datasets.

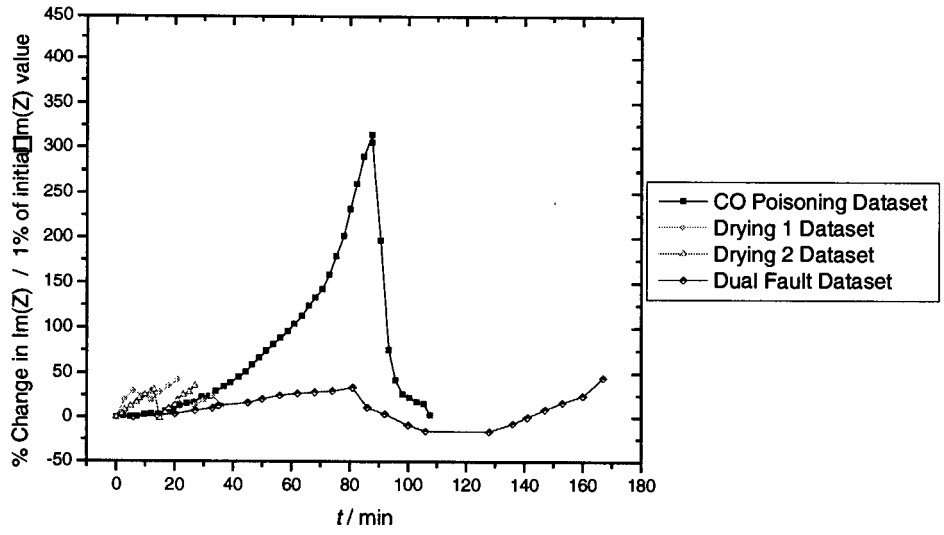

Figure 7.15: Percent Change in the Imaginary Part of the Impedance at 500 Hz vs. Time for CO Poisoning, Drying 1, Drying 2, and Dual Fault Datasets.

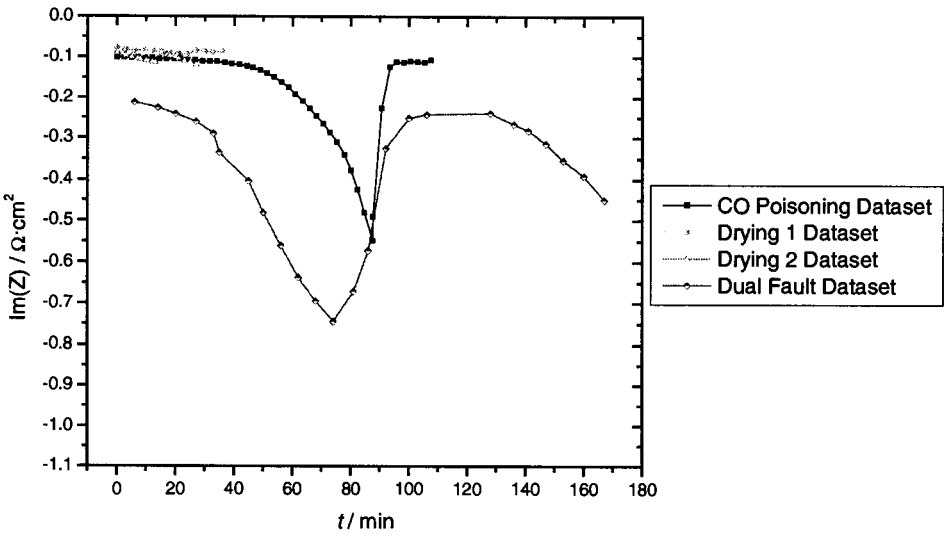

Figure 7.16: Imaginary Part of the Impedance at 50 Hz vs. Time for CO Poisoning, Drying 1, Drying 2, and Dual Fault Datasets.

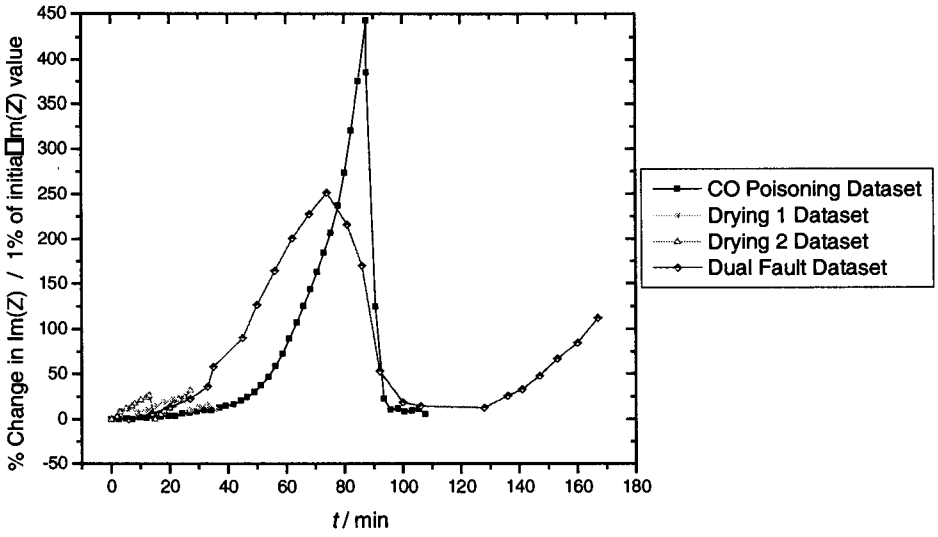

Figure 7.17: Percent Change in the Imaginary Part of the Impedance at 50 Hz vs. Time for CO Poisoning, Drying 1, Drying 2, and Dual Fault Datasets.

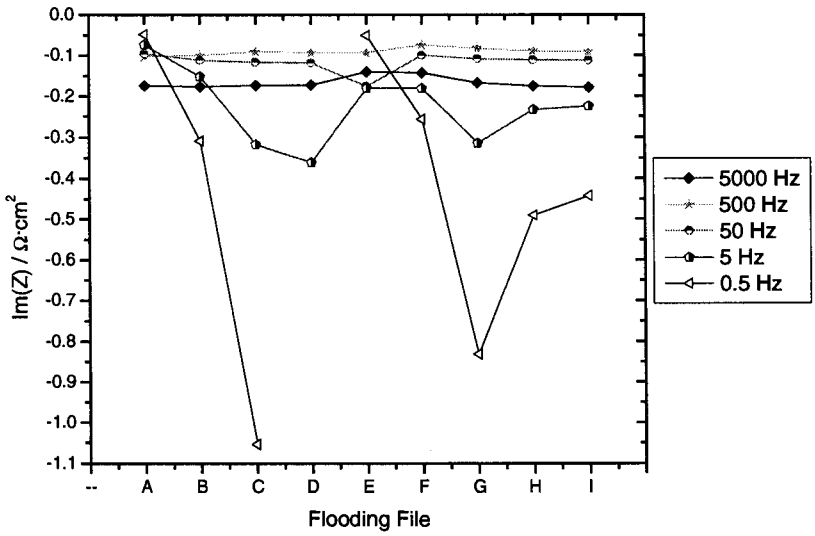

Figure 7.18: Imaginary Part of the Impedance for Flooding Data Files at 5000 Hz, 500 Hz, 50 Hz, 5 Hz, and 0.5 Hz.

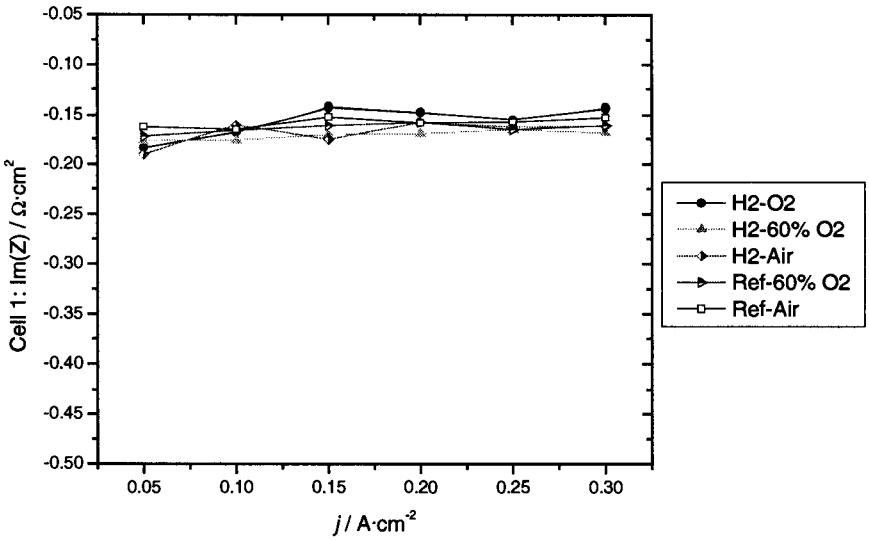

Figure 7.19: Imaginary Part of the Impedance at 5000 Hz vs. Current Density for H_2-O_2, H_2-60% O_2, H_2-Air, Ref – 60% O_2, and Ref-Air Datasets.

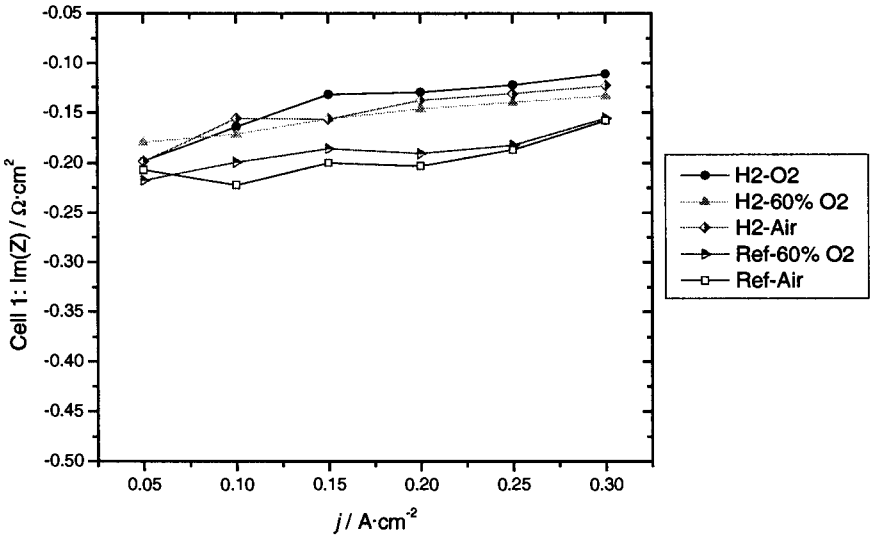

Figure 7.20: Imaginary Part of the Impedance at 500 Hz vs. Current Density for H_2-O_2, H_2-60% O_2, H_2-Air, Ref – 60% O_2, and Ref-Air Datasets.

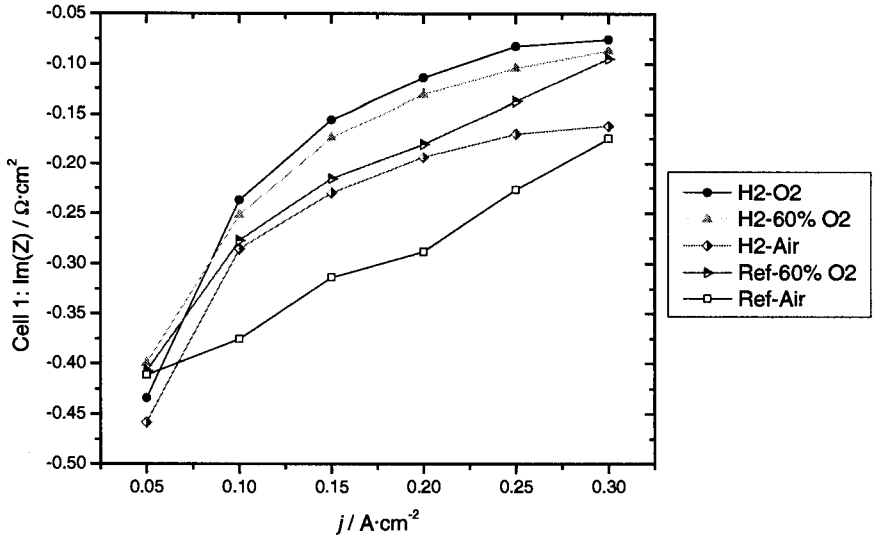

Figure 7.21: Imaginary Part of the Impedance at 50 Hz vs. Current Density for H_2-O_2, H_2-60% O_2, H_2-Air, Ref – 60% O_2, and Ref-Air Datasets.

7.2.3 Phase

Drying (Figure 7.22-Figure 7.27)

The phase of the impedance does not change substantially with drying using either hydrogen or reformate at all three frequencies. The percent change in the phase remains below 10 % for all three frequencies as well.

CO Poisoning (Figure 7.22-Figure 7.27)

The absolute phase of the impedance increases with CO poisoning. The percent change in the absolute phase of the impedance is greatest at 50 Hz (>50%).

Flooding (Figure 7.28)

Flooding can be characterized by very little change in phase at 5000 Hz and an increase in the absolute phase of the impedance at 500 and 50 Hz (>10 degrees).

Variation of Gas Composition (Figure 7.29-Figure 7.31)

At 5000 Hz and 500 Hz the absolute phase for datasets acquired with reformate is approximately 5 degrees larger than that of datasets acquired with hydrogen. At 5000 Hz, the magnitude of the phase does not change with current density, but at 500 Hz the magnitude of the phase increases as current density decreases. At 50 Hz the phase for the reformate-air and hydrogen-air datasets is about 5 degrees smaller than the phase for the other datasets. The phase at 50 Hz decreases with decreasing current density. Several other datasets would need to be acquired and analyzed to evaluate these trends with any kind of accuracy.

Summary

The phase does not change significantly with drying (both with hydrogen and reformate) at all three frequencies. The phase does change significantly with CO poisoning, particularly at 500 Hz and 50 Hz. It is of some concern that the phase changes significantly with current density at 50 Hz. It would likely be best to monitor the phase at 500 Hz, then if there is a change it is likely CO poisoning.

There is some difficulty differentiating between CO poisoning and flooding with the phase of the impedance. If monitoring the phase the impedance at 5000 Hz, 500 Hz, and 50 Hz assuming only the 3 fault conditions studied, a voltage drop could be identified as:

1. **Drying**: if there is very little (<10 %) change in the phase of the impedance at 5000, 500, and 50 Hz as voltage decreases with time.
2. **CO Poisoning or Flooding**: if there relatively low (< 20 %) percent change in the phase of the impedance at 5000 Hz and larger increases in the percent change in the phase of the impedance at 500 and 50 Hz.

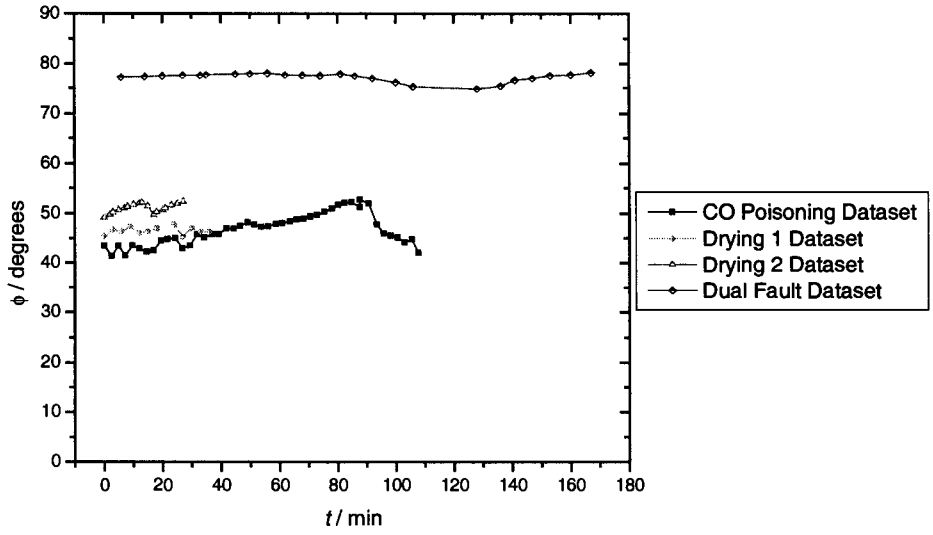

Figure 7.22: Phase of the Impedance at 5000 Hz vs. Time for CO Poisoning, Drying 1, Drying 2, and Dual Fault Datasets.

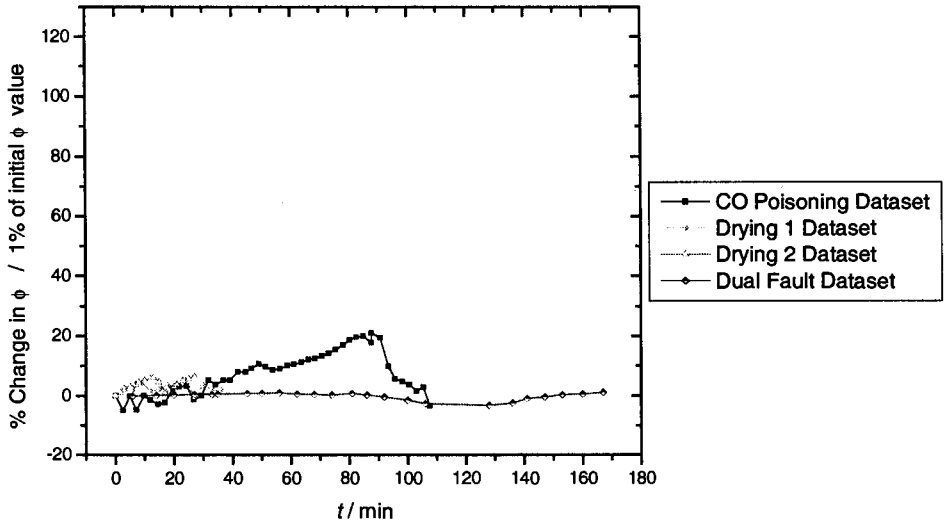

Figure 7.23: Percent Change in the Phase of the Impedance at 5000 Hz vs. Time for CO Poisoning, Drying 1, Drying 2, and Dual Fault Datasets.

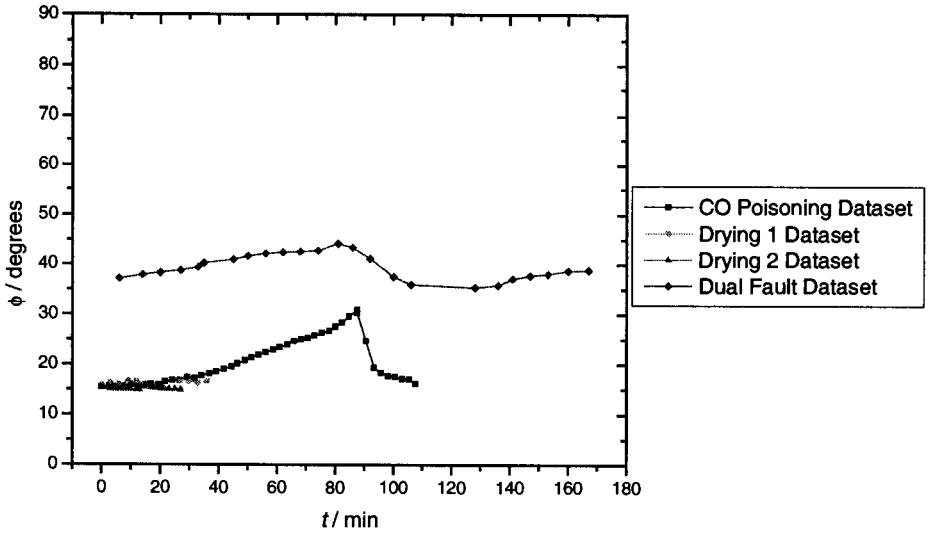

Figure 7.24: Phase of the Impedance at 500 Hz vs. Time for CO Poisoning, Drying 1, Drying 2, and Dual Fault Datasets.

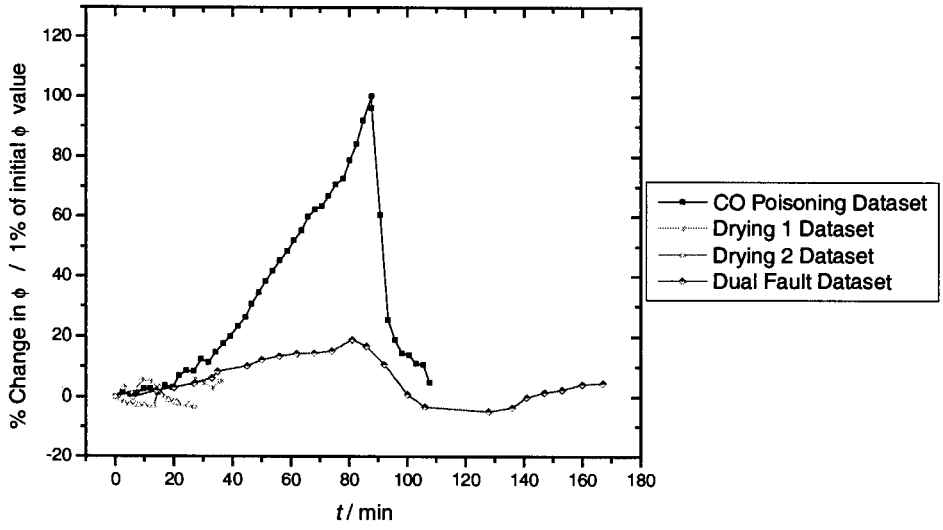

Figure 7.25: Percent Change in the Phase of the Impedance at 500 Hz vs. Time for CO Poisoning, Drying 1, Drying 2, and Dual Fault Datasets.

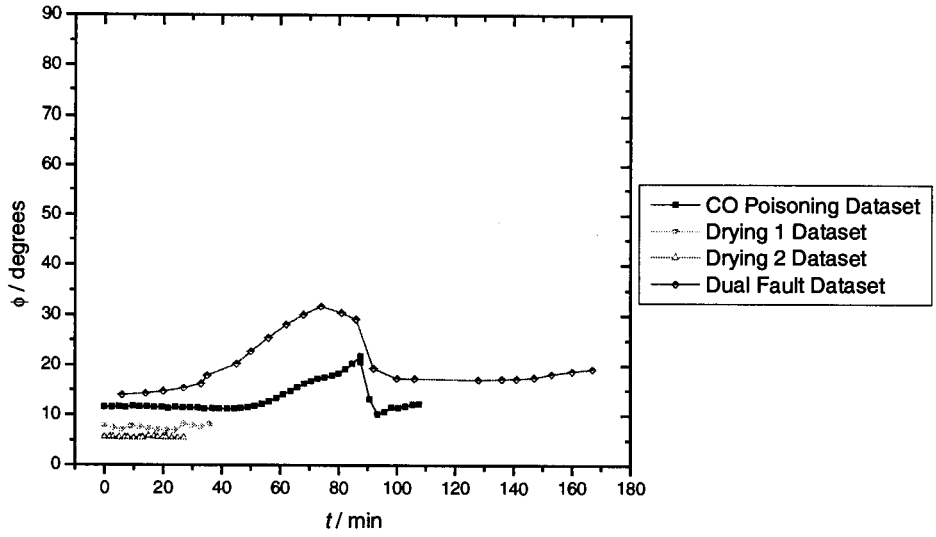

Figure 7.26: Phase of the Impedance at 50 Hz vs. Time for CO Poisoning, Drying 1, Drying 2, and Dual Fault Datasets.

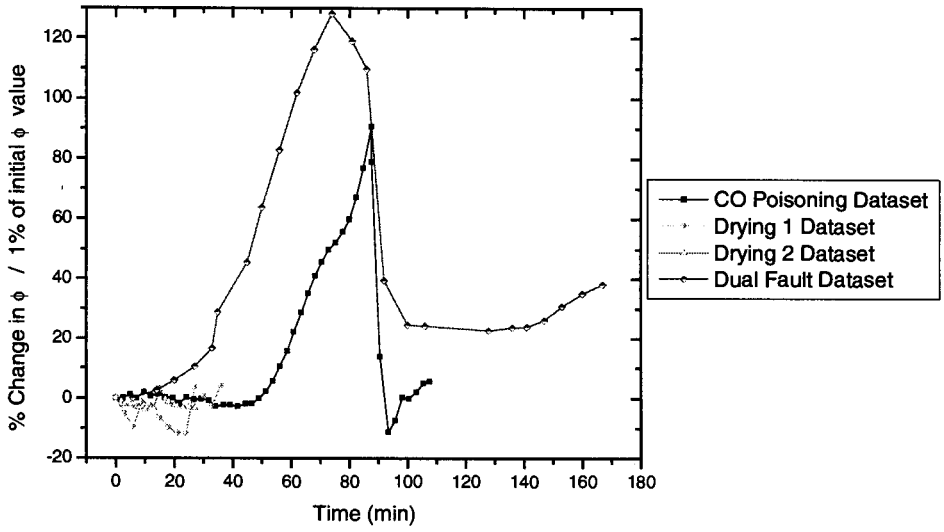

Figure 7.27: Percent Change in the Phase of the Impedance at 50 Hz vs. Time for CO Poisoning, Drying 1, Drying 2, and Dual Fault Datasets.

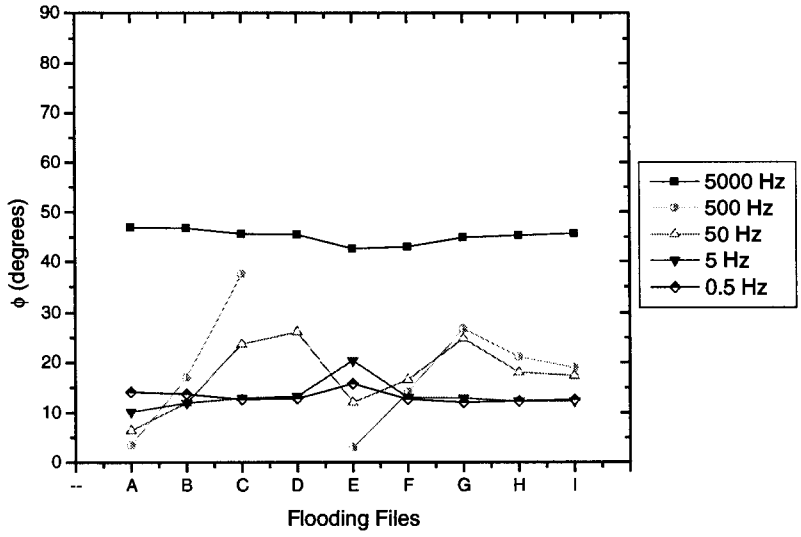

Figure 7.28: Phase of the Impedance for Flooding Data Files at 5000 Hz, 500 Hz, 50 Hz, 5 Hz, and 0.5 Hz.

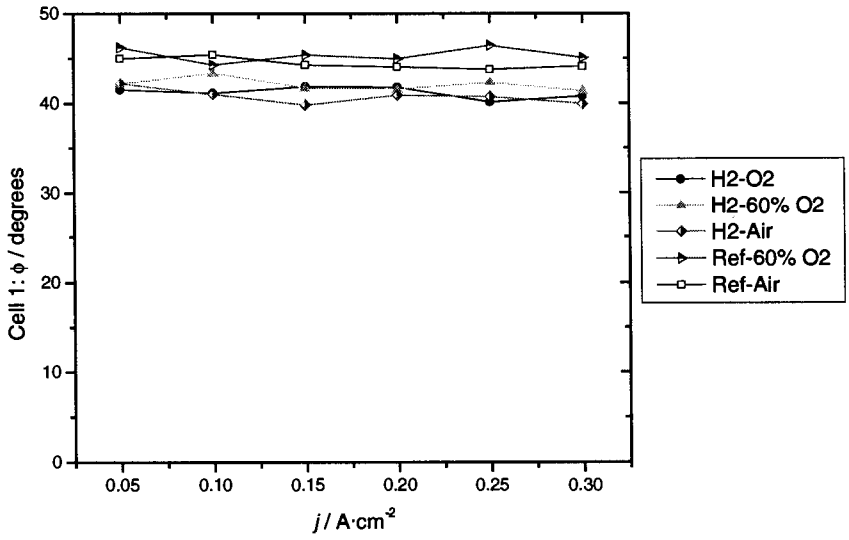

Figure 7.29: Phase of the Impedance at 5000 Hz vs. Current Density for H_2-O_2, H_2-60% O_2 , H_2-Air, Ref – 60% O_2, and Ref-Air Datasets.

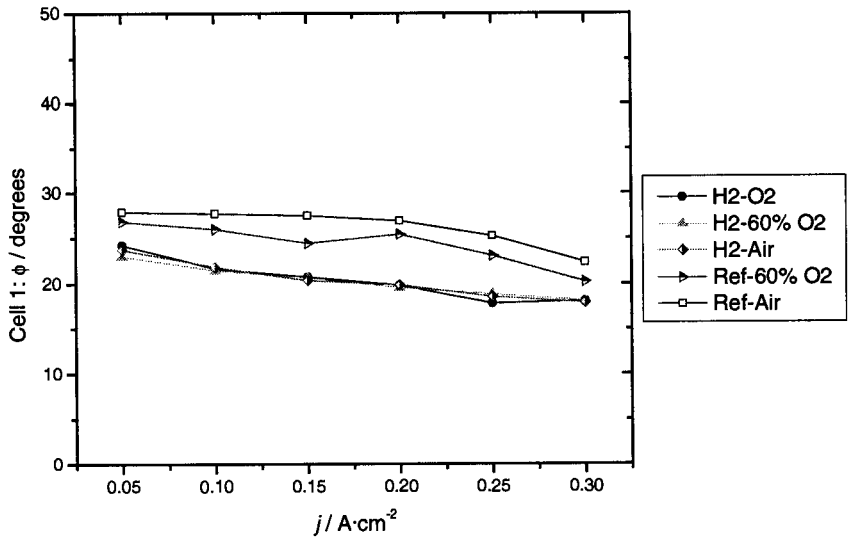

Figure 7.30: Phase of the Impedance at 500 Hz vs. Current Density for H_2-O_2, H_2-60% O_2 , H_2-Air, Ref – 60% O_2, and Ref-Air Datasets.

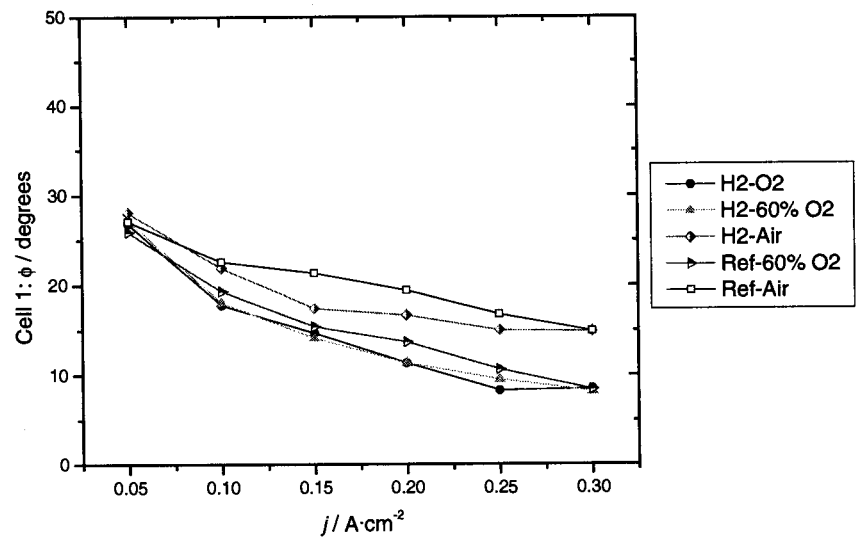

Figure 7.31: Phase of the Impedance at 50 Hz vs. Current Density for H_2-O_2, H_2-60% O_2 , H_2-Air, Ref – 60% O_2, and Ref-Air Datasets.

7.2.4 Magnitude

The magnitude of the impedance is relatively the easiest to measure of the parameters examined in this section.

Drying (Figure 7.32-Figure 7.37)

Although the actual change in magnitude is different at each frequency for drying (both with hydrogen and reformate) the percent change in magnitude remains relatively fixed for all three frequencies at approximately 50%.

CO Poisoning (Figure 7.32-Figure 7.37)

The magnitude of the impedance increases with CO Poisoning. The percent change in the magnitude of the impedance due to CO poisoning increases with decreasing frequency.

Flooding (Figure 7.38)

The magnitude of the impedance does not change significantly (<10 %) with flooding at 5000, 500, or 50 Hz.

Variation in Gas Composition (Figure 7.39-Figure 7.41)

There is very little change in the magnitude of the impedance at 5000 Hz and 500 Hz due to gas composition or current density. At 50 Hz the magnitude of the impedance is slightly larger for the dataset acquired with reformate, and the magnitude decreases with increasing current density.

Summary

For drying conditions, both with reformate and hydrogen, the percent change in the magnitude from normal conditions remains fairly constant (~50%) at all three frequencies

while, for CO poisoning conditions, the percent change in the magnitude increases as frequency decreases. There is very little change in the magnitude of the impedance (>10%) with flooding.

If monitoring the magnitude of the impedance at 5000 Hz, 500 Hz, and 50 Hz, assuming only the 3 fault conditions studied, a voltage drop could be identified as:

1. **Drying**: if there is a consistent percent increase of ~50% in $|Z|$ with at all three frequencies as voltage decreases with time.
2. **CO Poisoning**: if there are progressively larger percent increases in $|Z|$ at 5000 Hz, 500 Hz and 50 Hz as voltage decreases with time.
3. **Flooding**: if there is essentially no change in $|Z|$ from normal conditions as voltage decreases with time.

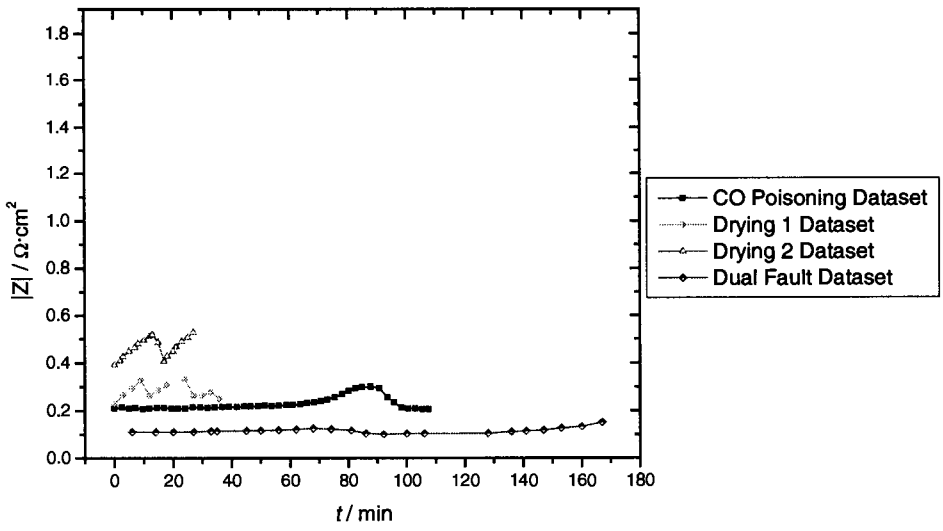

Figure 7.32: Magnitude of the Impedance at 5000 Hz vs. Time for CO Poisoning, Drying 1, Drying 2, and Dual Fault Datasets.

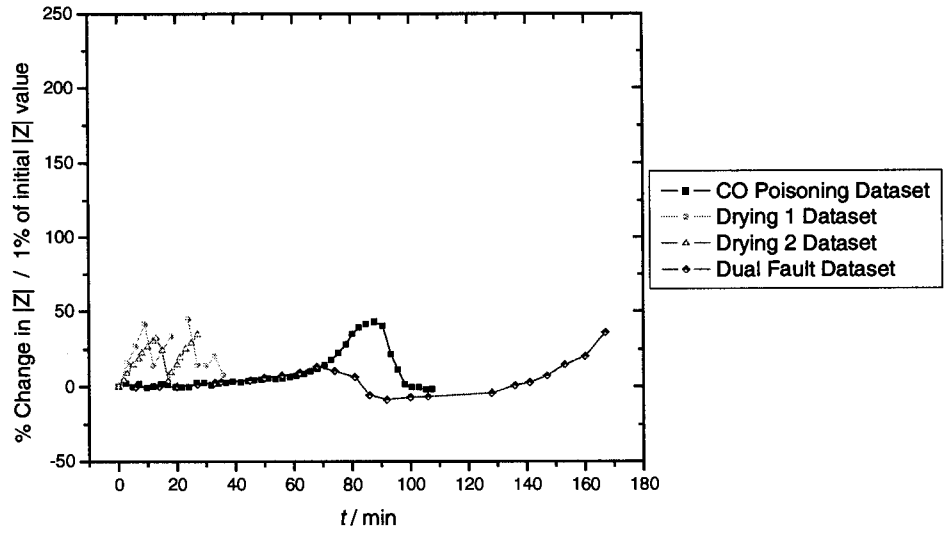

Figure 7.33: Percent Change in the Magnitude of the Impedance at 5000 Hz vs. Time for CO Poisoning, Drying 1, Drying 2, and Dual Fault Datasets.

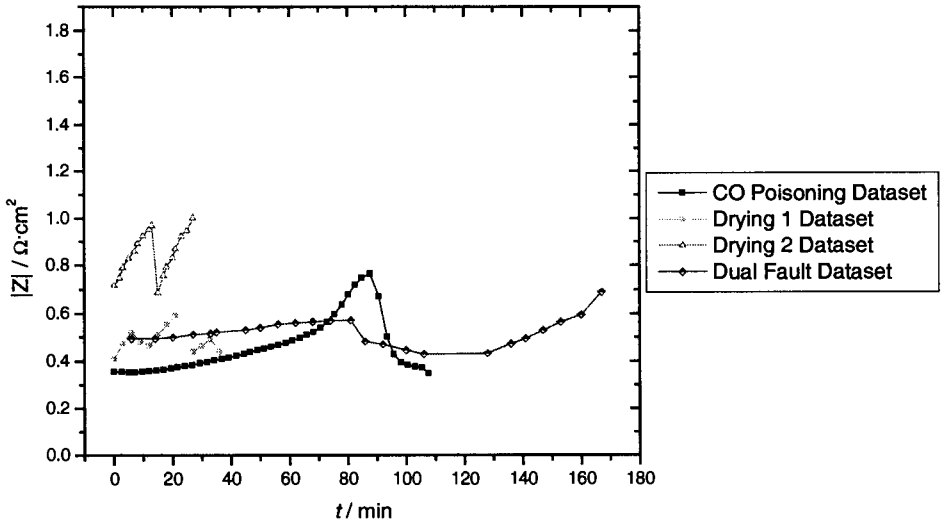

Figure 7.34: Magnitude of the Impedance at 500 Hz vs. Time for CO Poisoning, Drying 1, Drying 2, and Dual Fault Datasets.

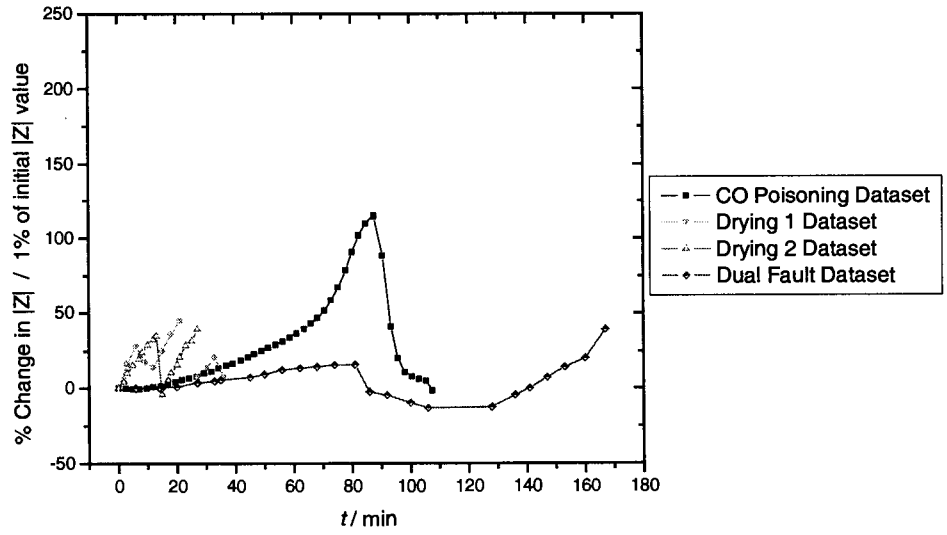

Figure 7.35: Percent Change in the Magnitude of the Impedance at 500 Hz vs. Time for CO Poisoning, Drying 1, Drying 2, and Dual Fault Datasets.

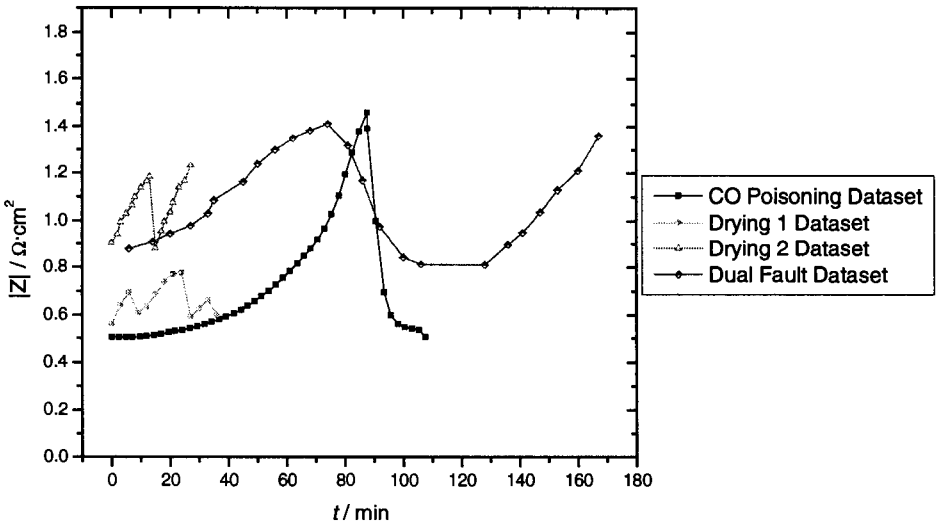

Figure 7.36: Magnitude of the Impedance at 50 Hz vs. Time for CO Poisoning, Drying 1, Drying 2, and Dual Fault Datasets.

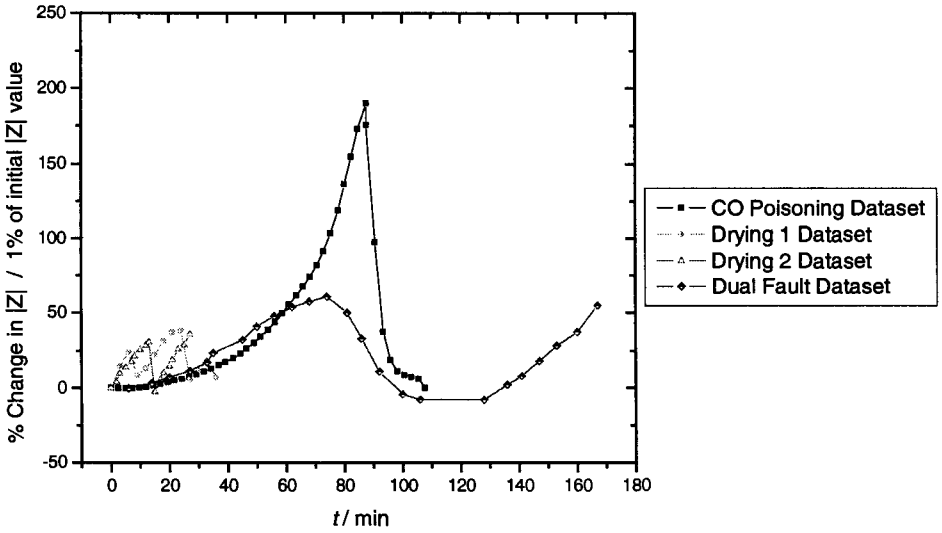

Figure 7.37: Percent Change in the Magnitude of the Impedance at 50 Hz vs. Time for CO Poisoning, Drying 1, Drying 2, and Dual Fault Datasets.

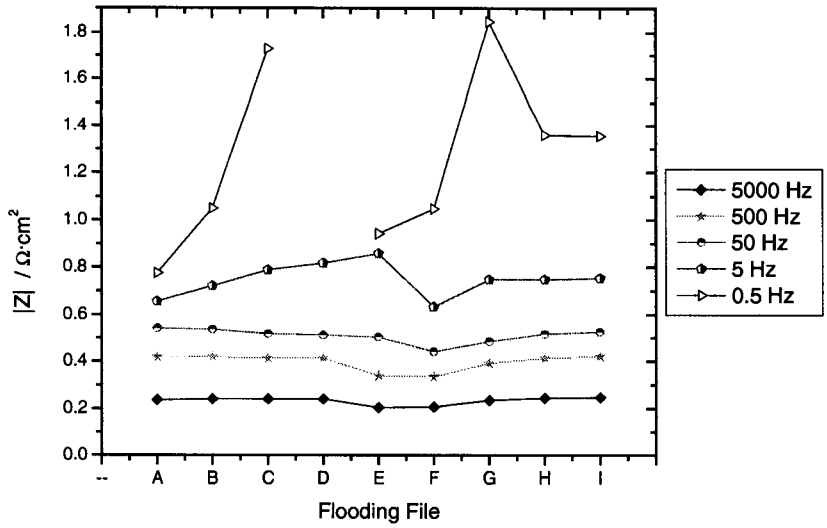

Figure 7.38: Magnitude of the Impedance for Flooding Data Files at 5000 Hz, 500 Hz, 50 Hz, 5 Hz, and 0.5 Hz.

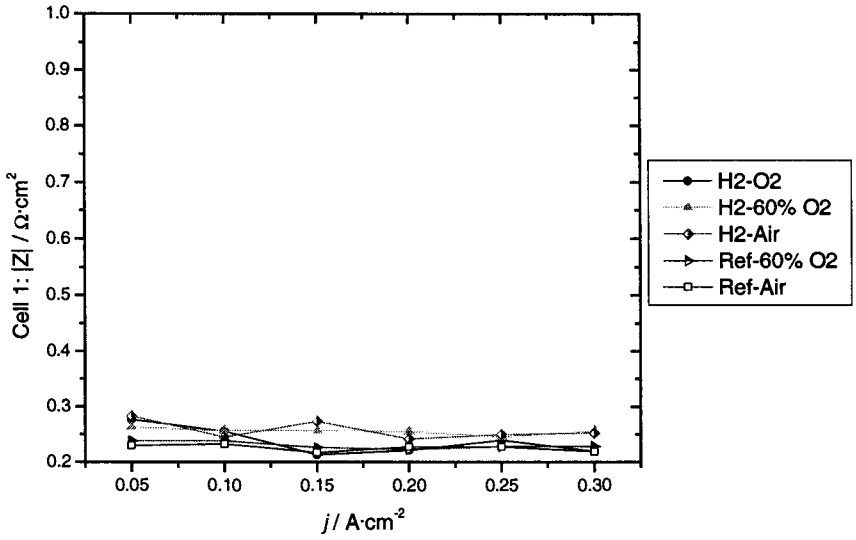

Figure 7.39: Magnitude of the Impedance at 5000 Hz vs. Current Density for H_2-O_2, H_2-60% O_2, H_2-Air, Ref – 60% O_2, and Ref-Air Datasets.

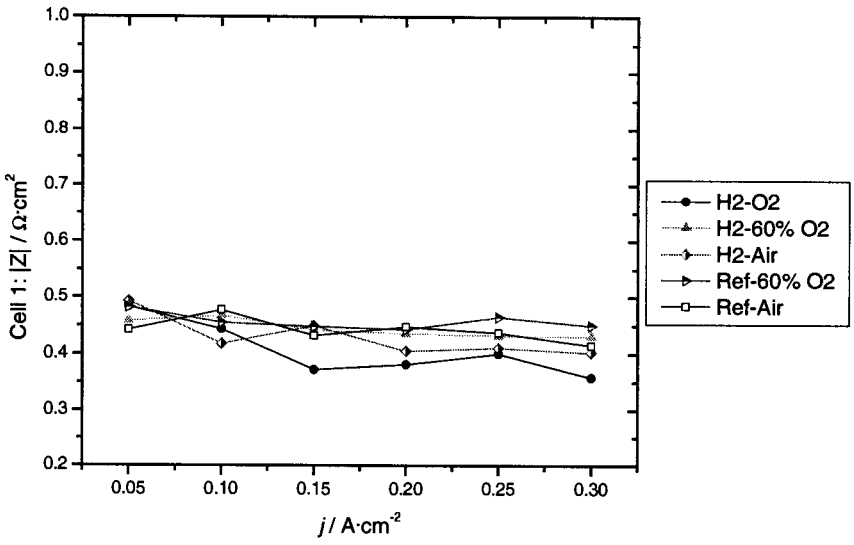

Figure 7.40: Magnitude of the Impedance at 500 Hz vs. Current Density for H_2-O_2, H_2-60% O_2 , H_2-Air, Ref – 60% O_2, and Ref-Air Datasets.

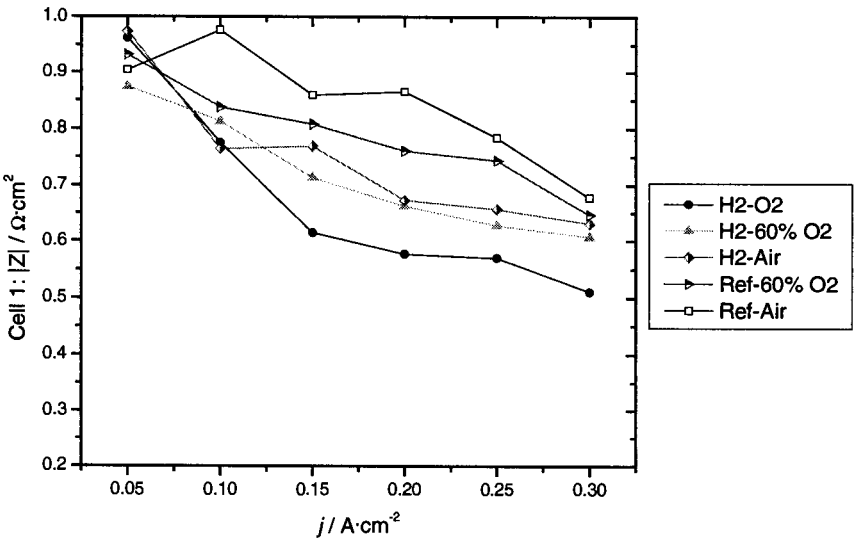

Figure 7.41: Magnitude of the Impedance at 50 Hz vs. Current Density for H_2-O_2, H_2-60% O_2 , H_2-Air, Ref – 60% O_2, and Ref-Air Datasets.

7.2.5 Slopes

To examine the interrelation between the three frequencies and how this is affected by fault conditions, threes slopes were analyzed. Each slope was calculated as follows, as illustrated in Eq 7-1, Eq 7-2, and Eq 7-3:

$$Slope1 = \frac{\mathrm{Im}(Z_{\omega=5000}) - 0}{\mathrm{Re}(Z_{\omega=5000}) - 0}$$

Eq 7-1

$$Slope2 = \frac{\mathrm{Im}(Z_{\omega=500}) - \mathrm{Im}(Z_{\omega=5000})}{\mathrm{Re}(Z_{\omega=500}) - \mathrm{Re}(Z_{\omega=5000})}$$

Eq 7-2

$$Slope3 = \frac{\mathrm{Im}(Z_{\omega=50}) - \mathrm{Im}(Z_{\omega=500})}{\mathrm{Re}(Z_{\omega=50}) - \mathrm{Re}(Z_{\omega=500})}$$

Eq 7-3

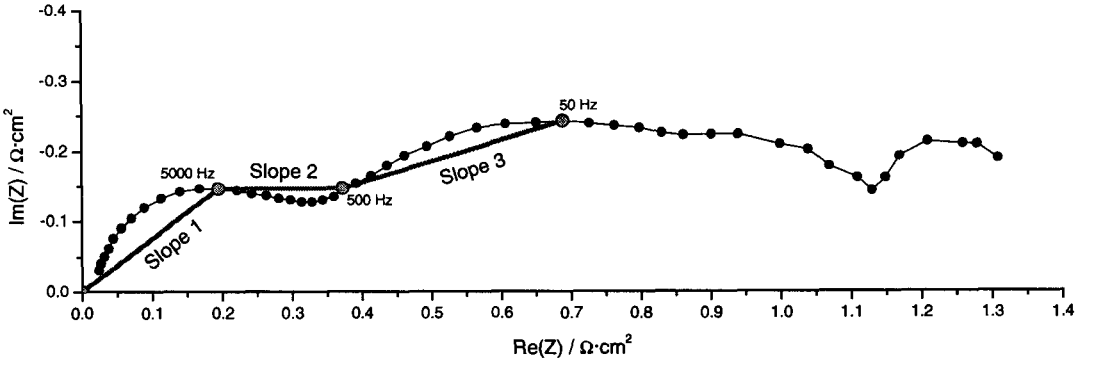

Figure 7.42:Typical Impedance Spectra with slopes 1,2, and 3 illustrated

Drying (Figure 7.43-Figure 7.54)

Slopes 1 and 3 do not change appreciably with drying conditions with either hydrogen or reformate. Slope 2 does change with drying (approximately 50 % increase in magnitude)

but not as significantly as CO poisoning does. Slopes 2 and 3 are positive for drying conditions, indicative of the characteristic shape of drying impedance data with a larger first semicircle feature.

CO Poisoning (Figure 7.43-Figure 7.54)

All three slopes change significantly with CO poisoning. Slopes 1 and 3 decrease as CO poisoning increases and Slope 2 increases then decreases before recovery. Those slopes that did not begin negative (Slopes 2 and 3) became negative as CO poisoning increased indicating an increase in the height of the second semicircle feature.

Flooding (Figure 7.43-Figure 7.54)

Slope 1 and Slope 2 do not change significantly with flooding conditions. Slope 3 varied with flooding, but not consistently. It should be noted that Slope 3 was consistently negative for flooding behaviour, indicating an increase in the height of the second semicircle feature.

Variation in Gas Composition (Figure 7.43-Figure 7.54)

There is some variation in the slopes with gas composition but not a significant amount. There is a decrease in all three slopes as current density decreases.

Summary

If monitoring the real part and imaginary part of the impedance at 5000 Hz, 500 Hz, and 50 Hz, assuming only the 3 fault conditions studied, a voltage drop could be identified by the slope 1, slope 2, and slope 3 behaviour as:

1. **Drying**: if Slope 1 is negative and its magnitude changes ~10 %, Slope 2 is positive and its magnitude does not change significantly, and Slope 3 is positive and its magnitude changes ~25 %.

2. **CO Poisoning**: if Slope 1 is negative and its magnitude changes with, Slope 2 is becomes negative and the percent change of its magnitude is significant ~50%, and Slope 3 becomes negative and the percent change of its magnitude is large ~300%,.

3. **Flooding**: if Slope 1 is negative and does not change significantly, Slope 2 is positive and its magnitude does not change significantly, and Slope 3 is negative.

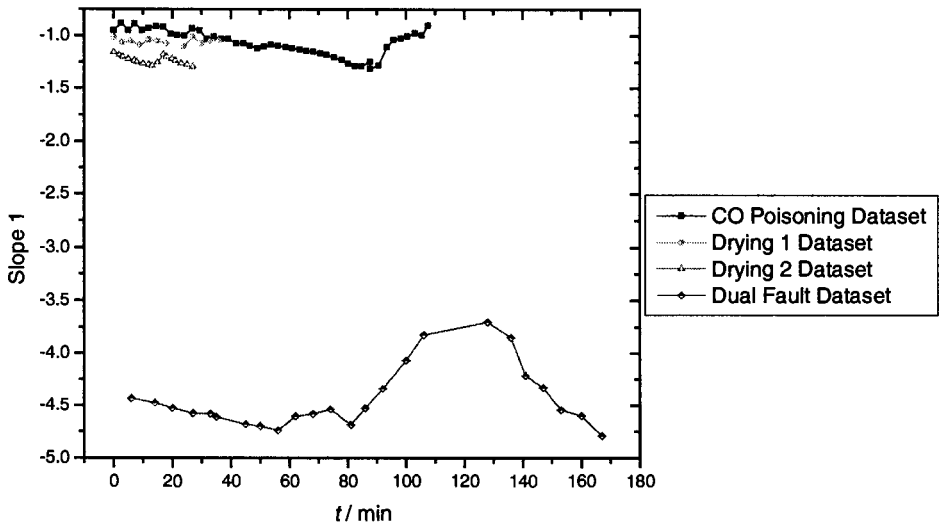

Figure 7.43: Slope 1 Values vs. Time for CO Poisoning, Drying 1, Drying 2, and Dual Fault Datasets.

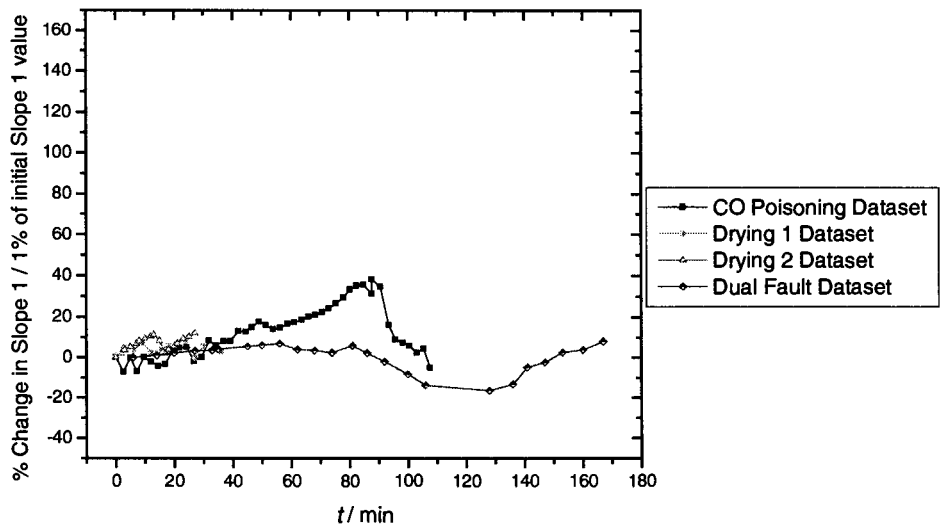

Figure 7.44: Percent Change in Slope 1 Values vs. Time for CO Poisoning, Drying 1, Drying 2, and Dual Fault Datasets.

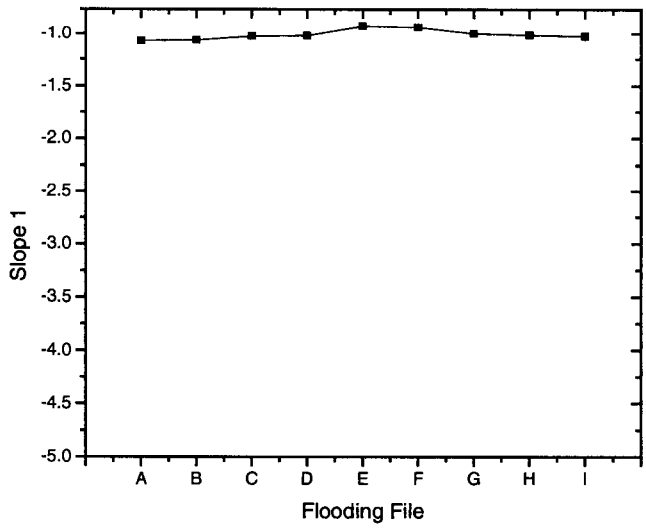

Figure 7.45: Flooding Dataset Slope 1 Values.

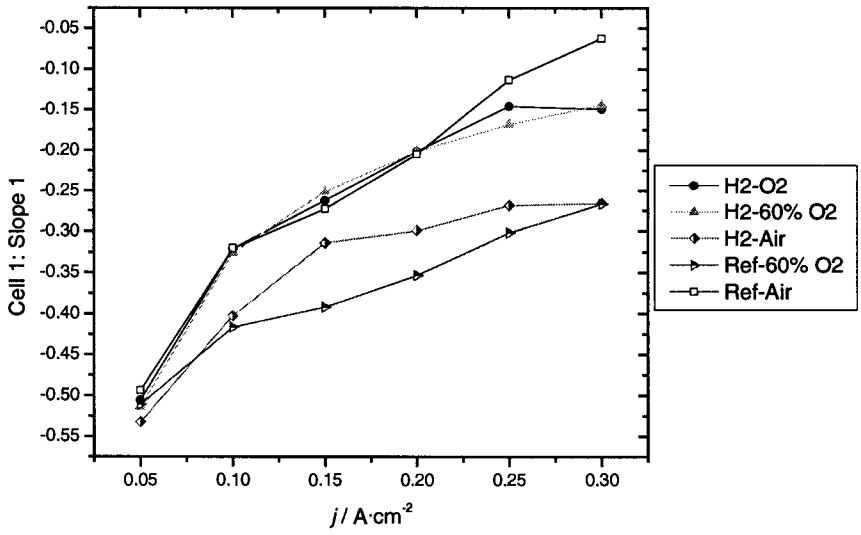

Figure 7.46: Slope 1 Values vs. Current Density for H_2-O_2, H_2-60% O_2 , H_2-Air, Ref – 60% O_2 , and Ref-Air Datasets.

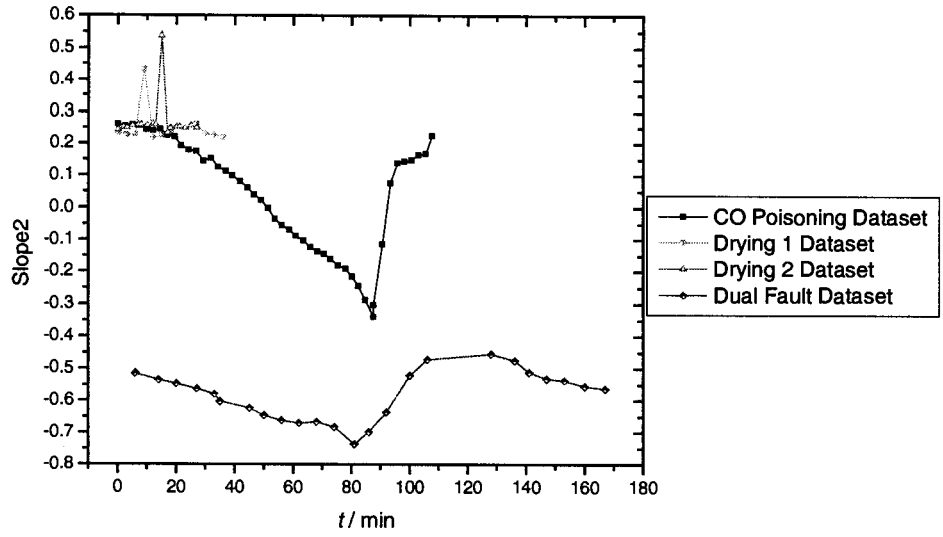

Figure 7.47: Slope 2 Values vs. Time for CO Poisoning, Drying 1, Drying 2, and Dual Fault Datasets.

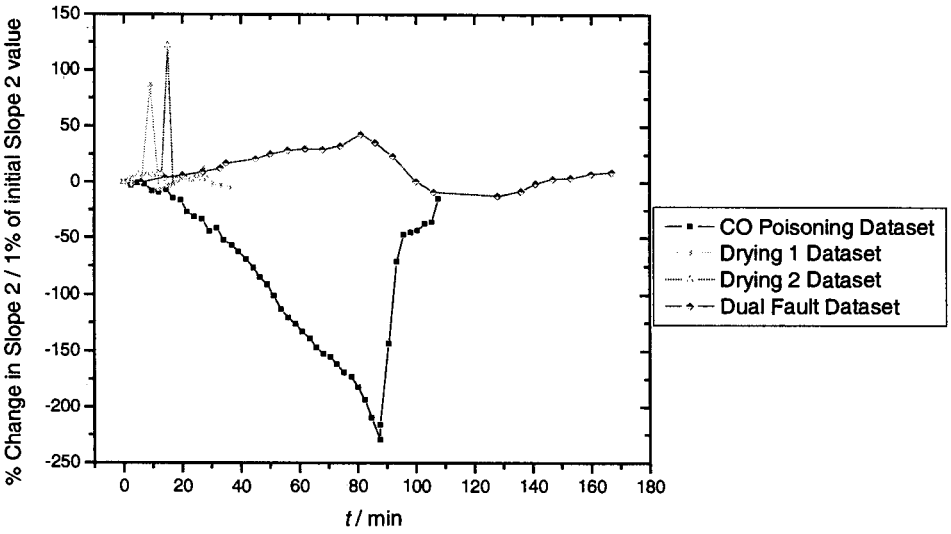

Figure 7.48: Percent Change in Slope 2 Values vs. Time for CO Poisoning, Drying 1, Drying 2, and Dual Fault Datasets.

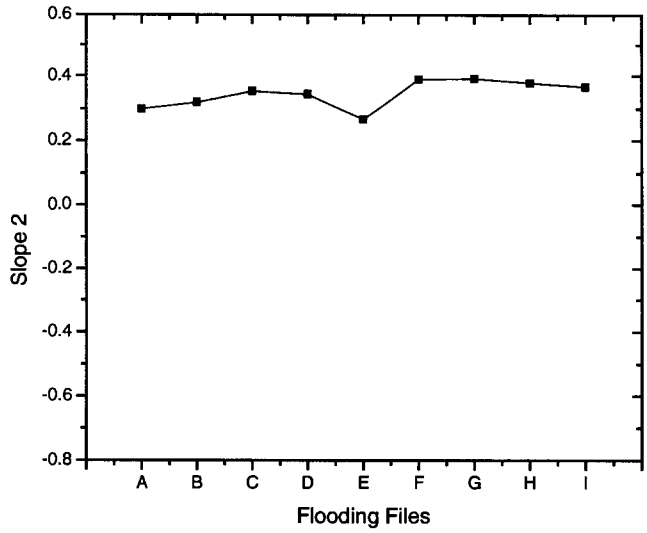

Figure 7.49: Flooding Dataset Slope 2 Values.

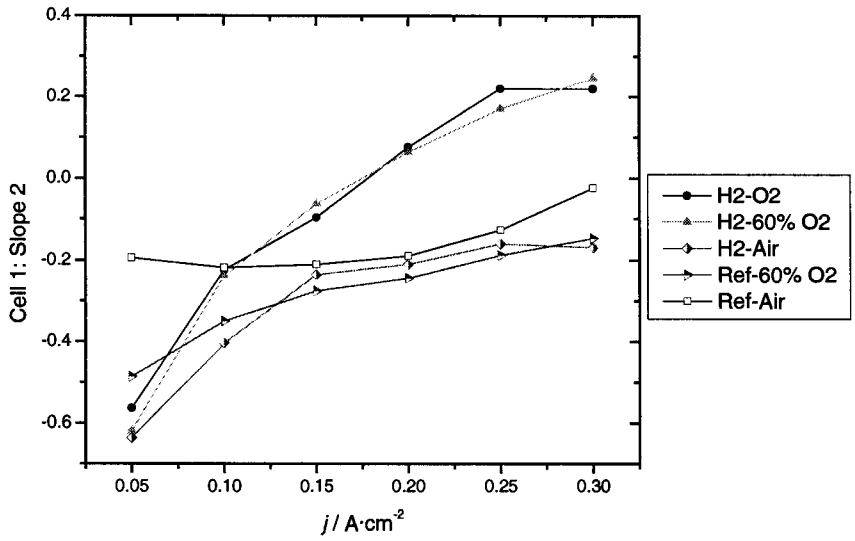

Figure 7.50: Slope 2 Values vs. Current Density for H_2-O_2, H_2-60% O_2 , H_2-Air, Ref – 60% O_2 , and Ref-Air Datasets.

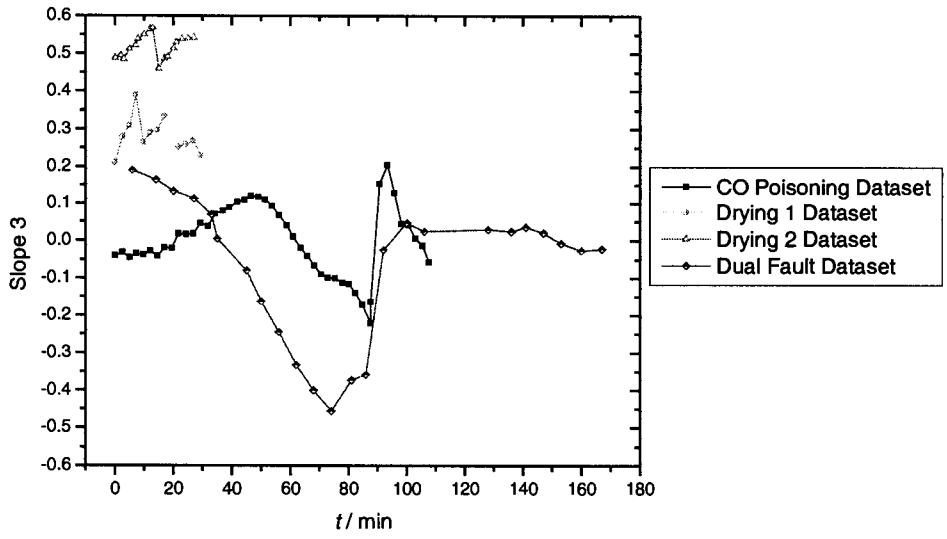

Figure 7.51: Slope 3 Values vs. Time for CO Poisoning, Drying 1, Drying 2, and Dual Fault Datasets.

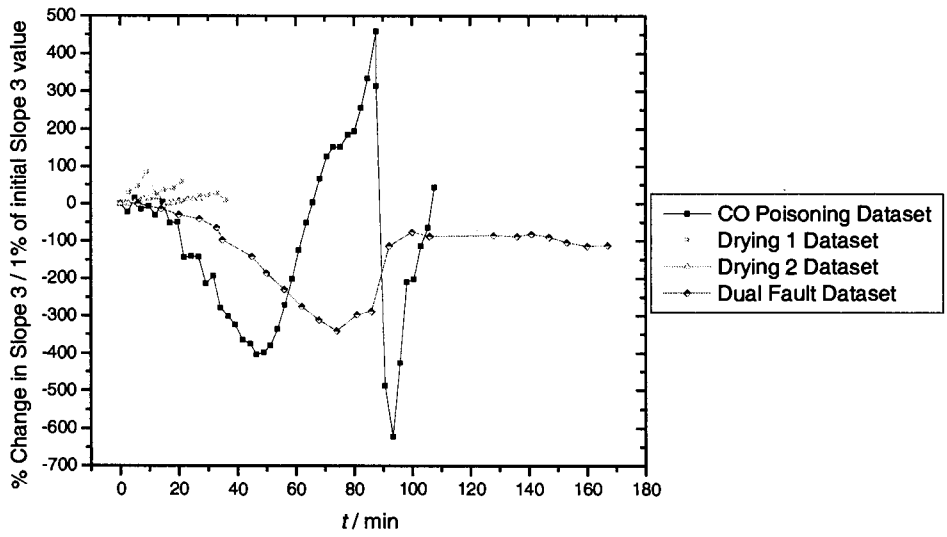

Figure 7.52: Percent Change in Slope 3 Values vs. Time for CO Poisoning, Drying 1, Drying 2, and Dual Fault Datasets.

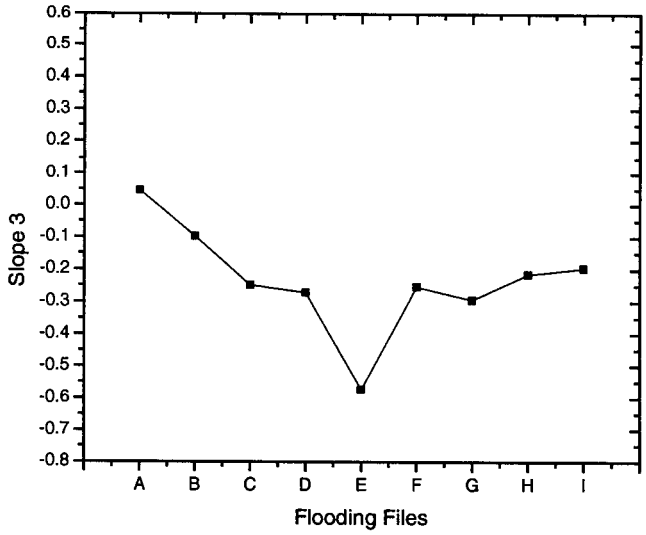

Figure 7.53: Flooding Dataset Slope 3 Values.

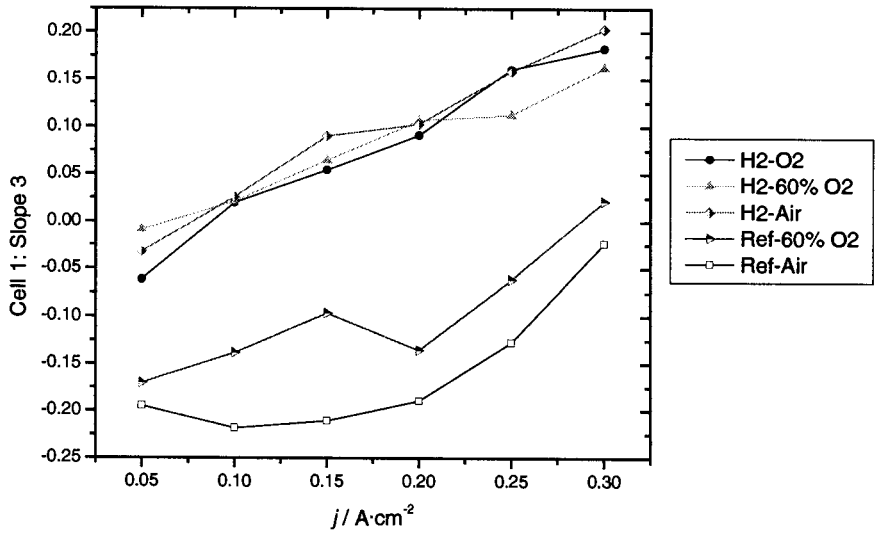

Figure 7.54: Slope 3 Values vs. Current Density for H_2-O_2, H_2-60% O_2, H_2-Air, Ref – 60% O_2, and Ref-Air Datasets.

7.3 Summary of multi frequency analysis

Any of the impedance parameters examined (Re(Z), Im(Z), φ, $|Z|$ or the slopes) are able to differentiate between drying and CO poisoning fault behaviour by examining only 50 Hz, 500 Hz, and 5000 Hz over time.

Given all the parameters examined and the datasets used, the Re(Z) parameter is the best, most conservative choice. It is the most consistently able to differentiate between all three faults and has the most consistent behaviour for each fault type. The Im(Z) and $|Z|$ parameters can be used to differentiate between faults, but with more risk involved. The phase is not very useful in differentiating between flooding and CO poisoning, but could be useful in differentiating between fuel gas compositions.

The magnitude of the impedance is the only parameter that is simple to measure on its own. The magnitude of an AC signal is electronically simple to measure. Any measurements requiring phase, or real and imaginary impedance components, need a phase sensitive detection scheme which is more electronically complex. Practically, to measure Re(Z), Im(Z), or φ, the values for all of the parameters will be acquired with little additional complexity. With this in mind, assuming only the 3 fault conditions studied, a voltage drop could be identified as:

Drying if :

- The percent change from "normal conditions" in Re(Z), Im(Z) and |Z| is similar for all three frequencies and is approximately 50% for our conditions.
- There is very little change in φ at all three frequencies.
- Slope 1 is negative and Slopes 2 and 3 are positive.

CO Poisoning if :

- The absolute percent change from "normal conditions" in Re(Z), Im(Z) and |Z| increases as the frequency decreases.
- Slope 1 is negative and Slopes 2 and 3 becomes more negative.

Flooding if:

- There is essentially no change in Re(Z), Im(Z) and in |Z| at all three frequencies.
- Slope 1 is negative, Slope 2 is positive, and Slope 3 is negative or becomes more negative.

To set more universal threshold values for these parameters, a more extensive baseline study would be necessary. This is primarily because there is a high level of variation in the first spectrum of each dataset and thus in the "normal operating conditions" impedance used for this work. The first spectrum in each drying dataset, in particular,

already appears to be quite "dry" when compared to well humidified spectra acquired under similar conditions. This means that, compared to well humidified baseline conditions, drying conditions likely have a higher than 50% increase in the Re(Z), Im(Z) and |Z| parameters with drying.

There are some differences in the response of the drying sequence from the dual fault dataset and the Drying 1 and Drying 2 datasets as well as the response of the CO poisoning sequence from the dual fault dataset and the CO poisoning dataset. This difference could be due to a variety of factors; different measurement techniques, different levels of fault severity, or different gas composition. More failure datasets will need to be acquired to decide.

8 Conclusions

In order to develop hardware solutions for both onboard and off-board EIS fuel cell fault diagnostics, algorithms were investigated to differentiate between flooding, drying, and CO poisoning fault conditions.

Equivalent circuit fitting was pursued primarily as an off-board diagnostic tool not only because of its potential to identify material properties, but also because of its sensitivity to fitting parameters.

An equivalent circuit was developed which consistently fitted impedance data during normal, flooding, drying, and CO poisoning conditions. The circuit, a resistor (*R1*) in series with a resistor (*R2*) and capacitor (*C1*) in parallel and a capacitor (C2) and short Warburg Element (*W1*) in parallel (Figure 4.21), can be used to accurately fit impedance data in the 50 Hz to 50 kHz frequency range. Further work still needs to be done to develop a model that fits consistently over a larger frequency range. This will provide a better understanding of the impedance in the f<500 Hz frequency region, particularly with regards to the third impedance feature and diffusion effects.

Using the circuit developed, CO poisoning and drying faults can be differentiated from one another by examining the *R1, R2* and Warburg *R* parameter behaviour. CO poisoning can be identified by an increase in the *R1* and *R2* parameters and a strong increase in the Warburg *R* parameter while drying can be characterized by a decrease in the *R1* parameter, a strong increase in the *R2* parameter, and an increase in the Warburg *R* parameters. Membrane resistivity and dielectric behaviour evaluated from the equivalent circuit parameter fit results are consistent with values found in the literature.

The multi frequency analysis technique was developed as a method for fault identification in an onboard setting. Because of this, a small number of frequencies were chosen to be monitored over time to differentiate between fault conditions.

Four impedance parameters were examined at 50, 500, and 5000 Hz; Re(Z), Im(Z), φ, $|Z|$ as well as impedance slopes. The real part of the impedance, of all the parameters examined, was able to most consistently differentiate between CO poisoning, drying and flooding conditions. For technical reasons, |Z| is the only parameter, of those investigated, that it is logical to measure independently. Given this, information from all the parameters could be used in the method outlined in Section 7.3 to differentiate between fault conditions.

8.1 Future Work/Recommendations

To develop more universal fault threshold values for both the equivalent circuit and MFA diagnostic techniques a better understanding of normal impedance conditions is required. There is a high level of variation in the first spectrum between datasets and thus in the "normal operating condition" for each dataset used in the work. This is evident particularly in the drying datasets where specific operating conditions were required to produce the faults, leading to already "dry" conditions in the normal operating conditions spectra.

Further testing needs to focus on the development of baseline "normal operating conditions" data, preferably for several fuel cell configurations, to determine if the baseline properties are individual to each fuel cell or universal. Pursuant to this, there needs to be further testing involving the rate and severity of fault conditions to ensure that faults are not confused, particularly CO poisoning and drying. Finally other fuel cell faults such as membrane ageing and other forms of catalyst poisoning should also be investigated. More time spent on each experiment, i.e., acquiring spectra continuously while creating a fault, to better understand absolute changes in impedance due to fault conditions would be helpful.

It is logical that more extensive and longer-term investigation take place on an actual commercial stack under some type of "normal operating conditions". Information about

actual noise levels, values of thresholds and the normal operating variation is required to optimize a final diagnostic scheme.

9 References

1. Mérida Donis, Walter Roberto, Diagnosis of PEMFC Stack Failures via Electrochemical Impedance Spectroscopy, PhD. Thesis, Mechanical Engineering, University of Victoria, (2002).
2. Le Canut, Jean-Marc, Walter Mérida, and David Harrington, Research and Development of a Fuel Cell Diagnostic Product, 6 Month Progress Report to Greenlight/IRAP, Greenlight Power Technologies/IESVic, (June 28 – 2002).
3. Le Canut, Jean-Marc, Ruth Latham, and David Harrington, Research and Development of a Fuel Cell Diagnostic Product, 12 Month Progress Report to Greenlight/IRAP, Greenlight Power Technologies/IESVic, (December 24 – 2002).
4. Le Canut, Jean-Marc, Ruth Latham, Wade Simpson, and David Harrington, Research and Development of a Fuel Cell Diagnostic Product, 18 Month Progress Report to Greenlight/IRAP, Greenlight Power Technologies/IESVic, (July 4 – 2003).
5. Le Canut, Jean-Marc, Ruth Latham, and David Harrington, Research and Development of a Fuel Cell Diagnostic Product, 24 Month Progress Report to Greenlight/IRAP, Greenlight Power Technologies/IESVic, (December 31 – 2003).
6. Hoogers, G., Fuel Cell Technology Handbook, CRC Press, Boca Raton, (2003).
7. Larminie, J., Dicks, A., Fuel Cell Systems Explained, John Wiley and Sons, Chichester, (2000).
8. http://www.fuelcells.org/fctypes.htm#zafc, Fuel Cell 2000, Types of Fuel Cells,
9. http://www.iesvic.uvic.ca/research/fuelcellsystems/fuelcelltypes.htm, IESVic Website, Types of Fuel Cells.
10. Tüber, Klaus, David Pócza, and Christopher Hebling, Visualization of water buildup in the cathode of a transparent PEM fuel cell, *Journal of Power Sources*, **124**, (2003), 403-414.
11. IMPACT AC Impedance Module, Hydrogenics Corporation, Mississauga, Ontario .
12. Knights, Shanna D., Lauritzen, Michael V., Vohra, Rajeev , Wilkinson, David P., Methods for operating fuel cells on impure fuels, US Patent # 6,500,572, December 31, 2002.
13. Lasia, Andrzej, Electrochemical Impedance Spectroscopy and its Application, *Modern Aspects of Electrochemistry*, **32**, edited by B.E. Conway *et al.*, Kuwer Academic/Plenum Publishers, New York, (1999).
14. Sluyters-Rehbach, M. , Impedances of Electrochemical Systems : Terminology , Nomenclature and Representation Part I: Cells with Metal Electrodes and Liquid Solution, *Pure & Applied Chemistry.* , **66** (9), (1994), 1831-1891.
15. J. R. Macdonald, Impedance Spectroscopy, John Wiley and Sons, New York, (1987).
16. Franceshetti, Donald R., and J. Ross Macdonald, Electrode Kinetics, Equivalent Circuits, and System Characterization: Small –Signal Conditions, *Journal of Electroanalytical. Chemistry.*, **82**, (1977), 271-301.
17. Harrington, D. A., CHEM 645: Advanced Electrochemistry – Class Notes, Class Notes, University of Victoria, (2003).
18. Fletcher, Stephen, The two terminal equivalent network of a three-terminal electrochemical cell, *Electrochemistry Communications*, **3**, (2001), 692-696.
19. Sadkowski, A., Time Domain Responses of Constant Phase Electrodes, *Electrochimica Acta*, **38** (14), (1993), 2051-2054.
20. Halsey, T.C., and M. Leibig, The Double Layer Impedance at a Rough Electrode: Random Walk Method, *Electrochimica Acta*, **36** (11/12), (1991), 1699-1702.
21. Buck, Richard P., and Carsten Mundt, Origins of finite transmission lines for exact representations of transport by the Nernst-Planck equations for each charge carrier, *Electrochimica Acta*,**44** ,(1999), 1999-2018.
22. Wang, J.C., Impedance of a Fractal Electrolyte-Electrode Interface, *Electrochimica Acta*, **33** (5), (1988), 707-711.
23. Mulder, W.H., and, J. H. Sluyters, Tafel currents at fractal electrode Connection with admittance spectra, *Journal of Electroanalytical Chemistry*, **285**, (1990), 103-115.
24. Mulder, W.H., and J. H. Sluyters, The admittance of smooth electrodes with a fractal carpet structure, *Journal of Electroanalytical Chemistry.*, **282**, (1990), 27-32.
25. Brug, G.L., A.L.G Van Den Eeden, M. Sluyters-Rehbach, and J.H. Sluyters, The Analysis of Electrode

Impedances Complicated by the Presence of a Constant Phase Element, *Journal of Electroanaytical.Chemistry.*, **176**, (1984), 275-295.
26. Lang, G., and K.E. Heusler, Remarks on the energetics of interfaces exhibiting constant phase element behaviour, *Journal of Electroanalytical. Chem*istry, **457**, (1998), 257-260.
27. Zoltowski, Piotr, On the electrical capacitance of interfaces exhibiting constant phase element behaviour, *Journal of Electroanalytical Chemistry*, **443**, (1998), 149-154.
28. Van Heuveln, Fred H., Analysis of Nonexponential Transient Response Due to a Constant Phase Element, *Journal of the Electrochemical Society.*, **141**(12), (1994), 3423-3428.
29. Bisquert, J., Germà Garcia-Belmonte, Francisco Fabergat-Santiago, and Paulo Roberto Bueno, Theoretical models of ac impedance of finite diffusion layers exhibiting low frequency dispersion, *Journal of Electroanalytical Chemistry*, **475**, (1999), 152-163.
30. Scheider, Walter, Theory of the Frequency dispersion of Electrode Polarization. Topology of Networks with Fractional Power Frequency Dependence, *Journal of Physical Chem*istry, **79**(2), (1975), 127-136.
31. Pajkossy, Tamàs, Wandlowski, Thomas, Kolb, Dieter, Impedance aspects of anion adsorption on gold single crystal electrodes, *Journal of Electroanalytical Chemistry*, **414**, (1996), 209-220.
32. Mulder, W.H., and J. H. Sluyters, J.H., An Explanation of Depressed Semi-Circular Arcs in Impedance Plots for Irreversible Electrode Reactions, *Electrochimica Acta*, **33**(3), (1988), 303-310.
33. Johnson, Derek, Z View v. 2.3d Software Help Files, Scribner and Associates, (1990-2000).
34. J. R. Macdonald, CNLS (Complex Non-Linear Least Squares) Immitance Fitting Program LEMV Manual V7.11, Solartron Group Ltd., (1999)
35. Macdonald, James Ross, Impedance Spectroscopy; Old Problems and New Developments, *Electrochimica Acta*, **35** (10), (1990),pp.1483-1492.
36. Boukamp, Bernard A. A package for impedance/admittance data analysis *Solid State Ionics* **18&19,** (1986) 136-140.
37. Bhatnagar, S., S. Gupta, K. Shahi, Automated measurement of ac impedance data: Acquisition and analysis, *Solid State Ionics* **31,**(1988), 107-115
38. Macdonald, J. Ross, and Larry D. Potter Jr., A flexible procedure for analyzing impedance spectroscopy results: Description and illustrations, *Solid State Ionics,* **23**, (1987), 61-79.
39. Marquardt, Donald W., An Algorithm foe Least-Squares Estimation of Non-Linear Parameters, *Journal of the Society for Industrial and Applied Mathematics*, **11**, (1963), 431-441.
40. Carson, S.L., Orazem, M.E., Crisalle, O.D., and Garcia-Rubio, L, On the Error of Impedance measurements – Simulation of FRA Instrumentation, *Journal of the Electrochemical Society*, **150**(10), (2003), E477-E490.
41. Carson, S.L., Orazem, M.E., Crisalle, O.D., and Garcia-Rubio, L, On the Error of Impedance measurements – Simulation of PSD Instrumentation, *Journal of the Electrochemical Society*, **150**(10), (2003), E491-E500.
42. P.R. Bevington, Data Reduction and Error Analysis for Physical Sciences, McGraw-Hill Book Company, New York, (1969).
43. Ballard 3 kW Fuel Cell Test Station Operating Manual, Document Number 710.743.001. Ballard Power Systems, 9000 Glenlyon Parkway, Burnaby, BC V5J 5J9 Canada (1996).
44. Le Canut, Jean-Marc, Personal Communication, March 2004.
45. Schiller, C.A., F. Richter, E. Gülzow, and N. Wagner, Relaxation impedance as a model for the deactivation mechanism of fuel cells due to carbon monoxide poisoning, *Physical Chemistry Chemical Physics*, **3**, (2001), 2113-2116.
46. Schiller, C.A., F. Richter, E Gülzow, and N. Wagner, Validation and evaluation of electrochemical impedance spectra of systems with states that change with time, *Physical Chemistry Chemical Physics*, **3**, (2001), 374-378.
47. Wagner, N., and M. Schulze, Change of electrochemical impedance spectra during CO poisoning of the Pt and Pt-Ru anodes in a membrane fuel cell (PEFC), *Electrochimica Acta*, **48**, (2003), 3899-3907.
48. Wagner, N., and E. Gülzow, Change of electrochemical impedance spectra (EIS) with time during CO-poisoning of the Pt-anode in membrane fuel cells, *Journal of Power Sources*, **127**, (2004), 341-347.
49. Andreaus, B., A.J. McEvoy, and G.G. Scherer, Analysis of performance losses in polymer electrolyte

fuel cells at high current densities by impedance spectroscopy, *Electrochimica Acta*, **47**, (2002), 2223-2229.

50. Andreaus, B., Scherer, G.G., Proton-conducting polymer membranes in fuel cells – humidification aspects, *Solid State Ionics*, **IN PRESS**, (2003).
51. Ciureanu, Mariana, Hong Wang, and Zhigang Qi, Electrochemical Impedance Study of Membranes – Electrode Assemblies in PEM Fuel Cells. II. Electrooxidation of H_2 and H_2/CO Mixtures on Pt/Ru Based Gas Diffusion Electrodes, *Journal of Physical Chemistry* B, **103**, 9645-9657.
52. Ciureanu, M., and H. Wang, Electrochemical impedance study of anode CO –poisoning in PEM fuel cells, *Journal of New Materials for Electrochemical Systems*, **3**, (2000), 107-119.
53. Ciureanu, M., S.D. Mikhailenko, and S. Kaliaguine, S., PEM fuel cells as membrane reactors: kinetic analysis by impedance spectroscopy, *Catalysis Today*, **82**, (2003), 195-206.
54. Beattie, Paul D., Francesco P. Orfino, Vesna I. Basura, Kristi Zyckowska, Jianfu Ding, Carmen Chuy, Jennifer Schmeisser, and Steven Holdcroft, Ionic conductivity of proton exchange membranes, *Journal of Electroanalytical Chemistry*, **503**, (2001), 45-56.
55. Eikerling, M., and A.A. Kornyshev, Electrochemical impedance of the cathode catalyst layer in polymer electrolyte fuel cells, *Journal of Electroanalytical Chemistry*, **475**, 107-123.
56. Baschuk, J.J., and Xianguo Li, Modeling of polymer electrolyte membrane fuel cells with variable degrees of water flooding, *Journal of Power Sources*, **86**, (2000), 181-196.
57. Jiang, S.P., J. G. Love, and Y. Ramprakash, Electrode behavior at (La, Sr)MnO_3/Y_2O_3-ZrO_2 interface by electrochemical impedance spectroscopy, *Journal of Power Sources*, **110**, (2002), 201-208.
58. Diethelm, Stefan, Alexandre Closset, Jan Van herle, A.J. McEvoy, and Kemal Nisancioglu, Study of oxygen exchange and transport in mixed conducting cobaltates by electrochemical impedance spectroscopy, *Solid State Ionics*, **135**, (2000), 613-618.
59. Bieberle, A., and L.J. Gauckler, Reaction mechanism of Ni pattern anodes for solid oxide fuel cells, *Solid State Ionics*, **135**, (2000), 337-345.
60. Matsuzaki, Yoshio, and Isamu Yasuda, Electrochemical properties of a SOFC cathode in contact with a chromium containing alloy separator, *Sold State Ionics*, **132**, (2000), 271-278.
61. Wagner, N., W. Schnurnberger, B. Müller, and M. Lang, Electrochemical impedance of solid-oxide fuel cells and polymer membrane fuel cells, *Electrochimica Acta*, **43** (24), (1998), 3785-3793.
62. Müller, Jens T., and Peter M. Urban, Characterization of direct methanol fuel cells by ac impedance spectroscopy, *Journal of Power Sources*, **75**, (1998), 139-143.
63. Müller, Jens T., Peter M. Urban, and Wolfgang F. Hölderich, Impedance studies on direct methanol fuel cell anodes, *Journal of Power Sources*, **84**, (1999), 157-160.
64. Friere, T.J.P, and Ernesto R. Gonzalez, Effects of membrane characteristics and humidification conditions on the impedance response of polymer electrolyte fuel cells, *Journal of Electroanalytical Chemistry*, **503**, (2001), 57-68.
65. Büchi, Felix N., and Günther G. Scherer, Investigation of the Transversal Water Profile in Nafion Membranes in Polymer Electrolyte Fuel Cells , *Journal of the Electrochemical Society*, **148** (3), (2001), A183-A188.
66. Paddision, Stephen J., David W. Reagor, and Thomas A. Zawodzinski Jr., High frequency dielectric studies of hydrated Nafion®, *Journal of Electroanalytical Chemistry*, **459**, (1998), 91-97.
67. Perusich, Stephen A., Peter Avankian, and Mimi Y. Keating, Dielectric Relaxation Studies of Peflurocarboxylate Polymers, *Macromolecules*, **26**, (1993), 4756-4764.
68. Mauritz Kenneth A., and Ruey-Mei Fu, Dielectric Relaxation Studies of Ion Motions in Electrolyte-Containing Perfluorosulfonaed Ionomers. 1. NaOH and NaCl Systems, *Macromolecules*, **21**, 1324-1333.
69. Mauritz, K. A., and H. Yun, Dielectric Relaxation Study of Ion Motions in Electrolyte-Containing Perfluorosulfonate Ionomers. 2. CH_3COONa, KCl, and KI Systems, *Macromolecules*, **21**, (1988), 2738-2743.
70. Mauritz, K.A., and H. Yun, Dielectric Relaxation Study of Ion Motions in Electrolyte-Containing Perfluorosulfonate Ionomers 3. $ZnSO_4$ and $CaCl_2$ Systems, *Macromolecules*, **22**, (1989), 220-225.
71. Mauritz, K.A., Dielectric Relaxation Study of Ion Motions in Electrolyte-Containing Perfluorosulfonate Ionomers. 4. Long Range Ion Transport, *Macromolecules*, **22**, (1989), 4483-4488.
72. Deng, Z.D., and K.A. Mauritz, Dielectric Relaxation Studies of Acid-Containing Short-Side-Chain

Perfluorosulfonic Acid Membranes., *Macromolecules*, **25**, (1992), 2369-2380.
73. Deng, Z.D., amd K.A. Mauritz, Dielectric Relaxation Studies of Water-Containing Short Side Chain Perfluorosulfonic Acid Membranes., *Macromolecules*, **25**, (1992), 2739-2745.
74. Schwarz, G., A Theory of the Low-Frequency Dielectric Dispersion of Colloidal Particles in Electrolyte Solutions, *Journal of Physical Chemistry*, **66**, (1962), 2626-2642.
75. Michaels, A. S., G.L. Falkenstein, and N.S. Schneider, Dielectric Properties of Polyanion-Polycation Complexes, *Journal of Physical Chemistry*, **69** (5), (1965), 1456-1465.
76. Romero-Castañón, T., L.G. Arriaga, and U. Cano-Castillo, Impedance spectroscopy as a tool in the evaluation of MEAs, *Journal of Power Sources*, **118**, (2003), 179-182.
77. Springer, T.E., T. A. Zawodzinski, M.S. Wilson, and S. Gottesfeld, Characterization of Polymer Electrolyte Fuel Cells Using AC Impedance Spectroscopy, *Journal of the Electrochemical Society*, **143** (2), (1996), 587-599.
78. Siroma, Z., T. Sasakura, K. Yasuda, M. Azuma, and Y. Miyazaki, Effects of ionomer content on mass transport in gas diffusion electrodes for proton exchange membrane fuel cells, *Journal of Electroanalytical Chemistry*, **546**, (2003), 73-78.
79. Parthasarathy, A., B. Davé, S. Srinivasan, A.J. Appleby, and C.R. Martin, The platinum microelectrode/Nafion interface: an electrochemical impedance spectroscopic analysis of oxygen reduction kinetics and Nafion characteristics, *Journal of the Electrochemical Society*, **139** (6), (1992), 1634-41.
80. Orazem, M, Pavan Shukla, and Michael A. Membrino, Extension of the measurement model approach for deconvolution of underlying distributions for impedance measurements, *Electrochimica Acta*, **47**, (2002), 2007-2034.